JOINT TRANSPORTATION
RESEARCH PROGRAM

INDIANA DEPARTMENT OF TRANSPORTATION
AND PURDUE UNIVERSITY

Backcalculated Dynamic Modulus Master Curve from the Time Histories of Falling Weight Deflectometer Surface Deflections

Mohammad Ali Notani, Seonghwan Cho, and John E. Haddock

SPR-4619 • Report Number: FHWA/IN/JTRP-2025/18 • DOI: 10.5703/1288284317898

RECOMMENDED CITATION

Notani, M. A., Cho, S., & Haddock, J. E. (2025). *Backcalculated dynamic modulus master curve from the time histories of falling weight deflectometer surface deflections* (Joint Transportation Research Program Publication No. FHWA/IN/JTRP-2025/18). West Lafayette, IN: Purdue University. https://doi.org/10.5703/1288284317898

AUTHORS

Mohammad Ali Notani, PhD
Research Associate
Purdue University
Lyles School of Civil and Construction Engineering

Seonghwan Cho, PhD
Pavement Research Engineer
Indiana Department of Transportation
Research and Development Division

John E. Haddock, Ph.D., PE.
Professor of Civil and Construction Engineering
Director of Indiana Local Technical Assistance Program
Purdue University
Lyles School of Civil and Construction Engineering

JOINT TRANSPORTATION RESEARCH PROGRAM

The Joint Transportation Research Program serves as a vehicle for INDOT collaboration with higher education institutions and industry in Indiana to facilitate innovation that results in continuous improvement in the planning, design, construction, operation, management and economic efficiency of the Indiana transportation infrastructure. https://engineering.purdue.edu/JTRP.

Published reports of the Joint Transportation Research Program are available at https://docs.lib.purdue.edu/jtrp/.

NOTICE

The contents of this report reflect the views of the authors, who are responsible for the facts and the accuracy of the data presented herein. The contents do not necessarily reflect the official views and policies of the Indiana Department of Transportation or the Federal Highway Administration. The report does not constitute a standard, specification, or regulation.

TECHNICAL REPORT DOCUMENTATION PAGE

1. Report No. FHWA/IN/JTRP-2025/18	**2. Government Accession No.**	**3. Recipient's Catalog No.**

4. Title and Subtitle Backcalculated dynamic modulus master curve from the time histories of falling weight deflectometer surface deflections	**5. Report Date** July 14, 2025 **6. Performing Organization Code**
7. Author(s) Mohammad Ali Notani, PhD Seonghwan Cho, PhD John E. Haddock, PhD, PE	**8. Performing Organization Report No.** FHWA/IN/JTRP-2025/18
9. Performing Organization Name and Address Joint Transportation Research Program Hall for Discovery and Learning Research (DLR), Suite 204 207 S. Martin Jischke Drive West Lafayette, IN 47907	**10. Work Unit No.** **11. Contract or Grant No.** SPR-4619
12. Sponsoring Agency Name and Address Indiana Department of Transportation (SPR) State Office Building 100 North Senate Avenue Indianapolis, IN 46204	**13. Type of Report and Period Covered** Final Report **14. Sponsoring Agency Code**

15. Supplementary Notes

Conducted in cooperation with the U.S. Department of Transportation, Federal Highway Administration.

16. Abstract

Accurate structural evaluation of flexible pavements is important for cost-efficient maintenance and rehabilitation (M&R) strategies. Traditional back-calculation methods based on Falling Weight Deflectometer (FWD) data assume elastic behavior, overlooking the viscoelastic nature of asphalt materials and subsequently leading to inaccuracies. This study introduces a mechanistic-based back-calculation technique to estimate the dynamic modulus (E*) master curve directly from FWD time-history data. By integrating layered elastic theory with viscoelastic principles, the proposed method first determines the relaxation modulus, E(t), using Differential-Time Fourier Transform (DTFT) analysis. This time-domain response is then converted into the frequency domain to construct the E* master curve. Validation against laboratory-measured dynamic modulus values from field-cored specimens demonstrates that the proposed technique generates highly accurate E* master curves for all asphalt layers. Moreover, the findings highlighted the importance of accurate pavement structural information, such as layer thickness and Poisson's ratio, for achieving reliable E* master curve.

17. Key Words mechanistic technique, back-calculation, FWD, dynamic modulus, mastercurve, non-destructive testing, asphalt pavement	**18. Distribution Statement** No restrictions. This document is available through the National Technical Information Service, Springfield, VA 22161.

19. Security Classif. (of this report) Unclassified	**20. Security Classif. (of this page)** Unclassified	**21. No. of Pages** 55	**22. Price**

Form DOT F 1700.7 (8-72) Reproduction of completed page authorized

EXECUTIVE SUMMARY

Introduction

Accurate structural evaluation that reflects the actual mechanical performance of flexible pavements is critical for effective pavement management. It allows related agencies to identify deficiencies and develop cost-efficient maintenance and rehabilitation (M&R) strategies. Most pavement structural evaluation techniques rely on non-destructive testing (NDT) results, such as using the Falling Weight Deflectometer (FWD), to interpret the pavement load-bearing capacity by estimating elastic modulus through backcalculation processes. However, purely elastic assumptions can lead to inaccurate assessments due to the viscoelastic nature of asphalt materials. A more accurate evaluation technique requires determining the dynamic modulus (E^*) master curve, which characterizes the asphalt material's time- and temperature-dependent response. Currently, E^* master curves are obtained through direct laboratory testing on field-cored specimens or empirical prediction models (i.e., the Witczak Models). Although the E^* master curve is important for assessing damaged flexible pavements and optimizing M&R strategies, laboratory testing is both time consuming and labor intensive. Meanwhile, the empirical models often lack the accuracy to avoid suboptimal budgeting and M&R decisions.

Recent advances in FWD technology allow for recording time-history deflection data that facilitates a dynamic analysis of flexible pavement performance. The present study introduces a mechanistic-based backcalculation technique to estimate the E^* master curve directly from FWD time-history data. By integrating elasticity and viscoelasticity principles within a layered pavement model, the method eliminates the need for extensive field-cored laboratory testing. The resulting framework improves the accuracy of in-situ pavement structural evaluations and supports better-informed decisions regarding M&R strategies.

Findings

The findings suggest that viscoelastic principles and layered elasticity theory allow for precise backcalculation of the relaxation modulus, $E(t)$. By applying Laplace transform functions along with a viscoelastic fractional-order differential model, the E^* master curve is backcalculated from FWD time history data. These backcalculated results are validated against laboratory dynamic modulus tests performed on field-cored specimens. Notably, the highest accuracy in the backcalculated E^* master curve is achieved for the surface layer, followed by the intermediate and base layers. Parametric analyses further show the E^* master curve's strong sensitivity to layer thickness; even a minor variation (i.e., 0.5 in.) results in significant changes in the E* values. Additionally, the Poisson ratio (ν) of the surface layer is found to significantly impact the accuracy of the backcalculated E^* master curve for that specific layer. In contrast, changes in ν for the intermediate and base layers have a relatively small effect on the backcalculated E^* master curves for all layers. These results suggest that errors in thickness measurements and assumptions about ν can result in considerable inaccuracies from actual values that can eventually compromise the precision of pavement structural performance assessments.

Implementation

The proposed mechanistic backcalculation technique provides transportation agencies and pavement engineers with an improved method for evaluating in-service flexible pavement performance. The mechanistic method only requires FWD time history data and pavement structural information to evaluate the load-bearing capacity of flexible pavements, substantially reducing reliance on time-consuming laboratory tests. In practice, this method allows precise determination of overlay thicknesses, more accurate scheduling of rehabilitation activities, and improved long-term performance predictions. Agencies can develop better rehabilitation strategies and overlay designs by accurately determining in-situ pavement mechanical performance that closely reflects actual field conditions.

CONTENTS

1. INTRODUCTION . . . 9
   1.1 Pavement Evaluation Techniques. . . . 9
   1.2 Falling Weight Deflectometer . . . 9
   1.3 Dynamic Modulus Backcalculation . . . 11
   1.4 Backcalculation Methods. . . . 12
   1.5 Problem Statement . . . 12
   1.6 Objectives. . . . 13
2. BACKGROUND . . . 13
   2.1 Introduction to Viscoelasticity . . . 13
   2.2 Creep Behavior . . . 13
      2.2.1 Characteristics of the Creep Function . . . 13
   2.3 Relaxation . . . 14
   2.4 Constitutive Relationships . . . 15
      2.4.1 Recovery Determination from Relaxation . . . 15
      2.4.2 Boltzmann Superposition Principle . . . 15
   2.5 Relation Between Creep and Relaxation . . . 17
      2.5.1 Laplace Transform. . . . 17
      2.5.2 Direct Construction $J(t) \leftrightarrow E(t)$ . . . 17
   2.6 Viscoelastic Mechanical Models . . . 18
      2.6.1 Integer-Order Differential Models. . . . 18
      2.6.2 Fractional-Order Differential Model . . . 20
   2.7 Time-Temperature Superposition . . . 20
   2.8 Master Curve . . . 21
   2.9 Layered Elastic Anisotropic Model . . . 21
   2.10 Mechanistic Model Development . . . 23
3. DATA COLLECTION . . . 24
   3.1 FWD Testing . . . 25
   3.2 Dynamic Modulus Testing . . . 26
   3.3 Methodology . . . 27
      3.3.1 Mechanistic Analysis . . . 27
      3.3.2 ViscoWave Analysis . . . 27
4. VISCOWAVE . . . 27
   4.1 C_1 Analysis . . . 30
   4.2 C_2 Analysis . . . 30
   4.3 C_3 Analysis . . . 31
   4.4 C_4 Analysis . . . 31
5. PAVEMENT ME SOFTWARE . . . 33
   5.1 MEPDG Hierarchical Input Levels. . . . 33
      5.1.1 Witczak Viscosity-Based E* Model . . . 34
6. RESULTS AND DISCUSSIONS . . . 36
   6.1 US 27 . . . 36
   6.2 SR 67 . . . 36
   6.3 SR 545 . . . 38
   6.4 SR 32 . . . 41
   6.5 US 20 . . . 41
   6.6 US 31 . . . 43
   6.7 I-69 . . . 44
   6.8 Evaluate FWD Time History Intervals Effects in Mechanistic Approach . . . 46
   6.9 Parametric Study of Mechanistic Approach . . . 47
      6.3.1 Surface Layer Thickness Sensitivity . . . 47
      6.3.2 Base Layer Thickness Sensitivity . . . 48
      6.3.3 Surface Layer’s Poisson Ratio Sensitivity. . . . 49
7. SUMMARY AND RECOMMENDATIONS . . . 52

REFERENCES . . . 52

LIST OF TABLES

Table 1.1 Current FWD Backcalculation Software 12

Table 3.1 Selected Pavement Section Information for FWD and Lab Testing 25

Table 4.1 Selected Road Section for ViscoWave Analysis 28

Table 4.2 ViscoWave Analysis Results for US 27 29

Table 4.3 ViscoWave Analysis Results for SR 67 29

Table 6.1 US 27 Pavement Structure Information 38

Table 6.2 SR 67 Pavement Structure Configuration Information 38

Table 6.3 SR 545 Pavement Structure Configuration Information 40

Table 6.4 SR 32 Pavement Structure Information 41

Table 6.5 US 20 Pavement Structure Information 43

Table 6.6 US 31 Pavement Structure Configuration Information 44

Table 6.7 I-69 Pavement Structure Configuration Information 46

Table 6.8 Baseline Values Used in the Parametric Study and Corresponding Variation Amounts 47

LIST OF FIGURES

Figure 1.1 INDOT FWD Device (a) View from Behind Device and (b) View of Underneath Device (October 2022) 9

Figure 1.2 Deflection Basin and Geophone Labels (Park et al., 2022) 10

Figure 2.1 Creep Behavior at Different Regions 14

Figure 2.2 (a) An Arbitrary Uniaxial Stress History, and (b) Corresponding Strain for Each Time Interval 15

Figure 2.3 Boltzmann's Superposition Principle for (a) an Arbitrary Uniaxial Strain History and (b) Responded Stress at Each Time Step *n* 16

Figure 2.4 (a) The Summation of Strain Steps Over Time. (b) Recovery Curve of Stress (σ) Created by the Superposition of Individual Relaxation Curves 17

Figure 2.5 Creep Function Decomposition: (a) Summation of Delayed and Immediate Heaviside Step Functions, and (b) Corresponding Summation of Relaxing Components 18

Figure 2.6 Primary Components of Integer-Order Viscoelastic Models: (a) Linear Spring, and (b) Dashpot 18

Figure 2.7 Maxwell Model 19

Figure 2.8 The Kelvin Model 19

Figure 2.9 The Burger Model 19

Figure 2.10 Element Configuration of 2S2P1D 20

Figure 2.11 A Cylindrical Coordinate System 22

Figure 2.12 FWD Configuration and Point of Interests for a Pavement Structure 24

Figure 2.13 Differential-Time Fourier Transform Analysis for Determining Relaxation Modulus 24

Figure 3.1 (a) FWD Time History Data for SR 67 and (b) SR 67 Appearance Before FWD Testing 25

Figure 3.2 (a) FWD Testing and (b) Field-Core Sampling (I-69 Test Section) 26

Figure 3.3 *E** Master Curve Constructed by FlexMAT From Dynamic Modulus Test Results Performed at Three Test Temperatures 26

Figure 4.1 ViscoWave Results Based on FWD Time History Data 28

Figure 4.2 ViscoWave Time History Data for Two FWD Geophones (a) Geophone D0 and (b) Geophone D18 28

Figure 4.3 ViscoWave and Field Core Dynamic Modulus Tests Results for US 27 (a) Surface Layer; (b) Intermediate Layer; (c) Base Layer 29

Figure 4.4 ViscoWave and Lab Testing Results for SR 67 Road Section (a) Surface Layer; (b) Intermediate Layer; (c) Base Layer 30

Figure 4.5 C_1 Effect on Sigmoidal Function 31

Figure 4.6 C_2 Variation Effect on the Sigmoidal Function Shape 32

Figure 4.7 C_3 Variation Effect on the Sigmoidal Function Shape 32

Figure 4.8 C_4 Analysis Under +0.5 Increment 33

Figure 5.1 MEPDG Required Data Input: (a) Level 1, (b) Level 2, and (c) Level 3 34

Figure 5.2 Relaxation Modulus for an Asphalt Mixture Determined at the Three MEPDG Levels 35

Figure 5.3 Air Voids Content Effects On E* At Different Loading Frequencies 36

Figure 6.1 US 27 Test Section 37

Figure 6.2 *E** Master Curves for the US 27 Pavement Layers: (a) Surface, (b) Intermediate, and (c) Base 37

Figure 6.3 SR 67 Test Section 38

Figure 6.4 *E** Master Curves for the SR 67 Flexible Pavement: (a) Surface Layer, (b) Intermediate Layer, and (c) Base Layer 39

Figure 6.5 SR 545 Test Section 39

Figure 6.6 *E** Master Curves for the SR 545 Pavement: (a) Surface Layer, (b) Intermediate Layer, and (c) Base Layer 40

Figure 6.7 SR 32 Test Section 41

Figure 6.8 *E** Master Curves for the SR 32 Pavement: (a) Surface Layer, (b) Intermediate Layer, and (c) Base Layer 42

Figure 6.9 US 20 Pavement Section 42

Figure 6.10 *E** Master Curves for the US 20 Pavement Section: (a) Surface Layer, (b) Intermediate Layer, and (c) Base Layer 43

Figure 6.11 US 31 Test Section 44

Figure 6.12 *E** Master Curves for the US 31 Pavement: (a) Surface Layer, (b) Intermediate Layer, and (c) Base Layer 45

Figure 6.13 I-69 Test Section 45

Figure 6.14 *E** Master Curves for the I-69 Pavement: (a) Surface Layer, (b) Intermediate Layer, and (c) Base Layer 46

Figure 6.15 *E** Master Curves Obtained at Several Time-Interval Steps 47

Figure 6.16 Backcalculated *E** Master Curves Under a 0.5-in. Increase in the Surface Layer Thickness: (a) Surface Layer, (b) Intermediate Layer, and (c) Base Layer 48

Figure 6.17 Backcalculated *E** Master Curves Under a 1-in. Increase in the Intermediate Layer Thickness: (a) Surface Layer, (b) Intermediate Layer, and (c) Base layer 49

Figure 6.18 Backcalculated *E** Master Curves Under a 2-in. Increase in the Base Layer Thickness: (a) Surface Layer, (b) Intermediate Layer, and (c) Base Layer 50

Figure 6.19 Backcalculated ***E**** Master Curves Under a 10% Change in the Surface Layer's ν: (a) Surface Layer, (b) Intermediate Layer, and (c) Base Layer 50

Figure 6.20 Backcalculated ***E**** Master Curves Under a 10% Change in the Intermediate Layer's ν: (a) Surface Layer, (b) Intermediate Layer, and (c) Base Layer 51

Figure 6.21 Backcalculated ***E**** Master Curves Under a 10% Change in the Base Layer's ν: (a) Surface Layer, (b) Intermediate Layer, and (c) Base Layer 51

1. INTRODUCTION

1.1 Pavement Evaluation Techniques

Pavement evaluation is a key step in the pavement management system that allows pavement-related agencies to assess in-service pavement functional and structural performance (Haas & Hudson, 1978). An appropriate pavement evaluation not only identifies existing deficiencies but also helps agencies predict future performance and subsequently develop cost-effective maintenance and rehabilitation (M&R) strategies (Shahin, 1994). Therefore, the need for more accurate and reliable evaluation approaches has led pavement researchers to develop and advance pavement evaluation techniques (Manjusha & Sunitha, 2023; Schnebele et al., 2015; Shahin, 1994).

Functional pavement performance is generally evaluated by inspecting surface conditions to detect visible defects, such as roughness, cracking, and rutting (Cai et al., 2020). Such assessments can be performed using visual inspections; nondestructive testing (NDT); and automated methods such as laser profilers, remote sensing, and strain accelerometers (Nair et al., 1985; Roberts & Hudson, 1971; Sabahfar et al., 2021). Conversely, structural pavement evaluation techniques primarily assess the load-bearing capacity of the pavement layers, including surface, intermediate, and base courses. Assessing both pavement functional and structural aspects is crucial because pavements can be functional sound but have inherent structural defects that can contribute to early pavement failure.

Traditional structural evaluation techniques are based on field-core sampling and subsequent laboratory testing. While these methods can provide accurate performance information, they are time consuming and labor intensive, cause traffic disruptions, and become expensive when applied at the network level. To overcome this limitation, NDT methods, such as the Falling Weight Deflectometer (FWD), have become widely used to assess in-service pavement mechanical performance (Chen et al., 1999; Lytton, 1989).

1.2 Falling Weight Deflectometer

The FWD test is a useful pavement field test that provides information about pavement structural capacity (Gopalakrishnan et al., 2014; Varma et al., 2013). It operates by dropping weight from a certain height onto a load plate positioned on the pavement surface, generating a load pulse that simulates the impact of a passing wheel load (Figure 1.1). This loading is characterized by a short duration, typically 25–35 ms (Lee, 2014). The impulse loading causes stress distribution within the pavement structure in the form of a mechanical wave. The pavement response to the impulse loading is time-dependent deflections which are measured by the FWD geophones. The geophones are strategically placed at various radial distances from the load center to record the deflection (Sharma & Das, 2008). The recorded deflection data is important for analyzing the structural integrity and performance of the pavement layers. This impulse FWD loading causes inertia effects in the pavement, which are important for determining each pavement layer's stiffness (Sebaaly et al., 1985).

Figure 1.1 shows the Indiana Department of Transportation (INDOT) FWD device with geophones placed longitudinally to measure and record pavement deflections. The deflection basin is the main output from the FWD test (Figure 1.2). It provides valuable insights into pavement layer conditions, allowing engineers to identify potential structural deficiencies and determine appropriate maintenance or rehabilitation strategies.

Deflection basin data is commonly used to determine pavement layer properties, such as stiffness or modulus of elasticity, through an inverse technique known as "backcalculation." This

Figure 1.1 INDOT FWD Device (a) View from Behind Device and (b) View of Underneath Device (October 2022).

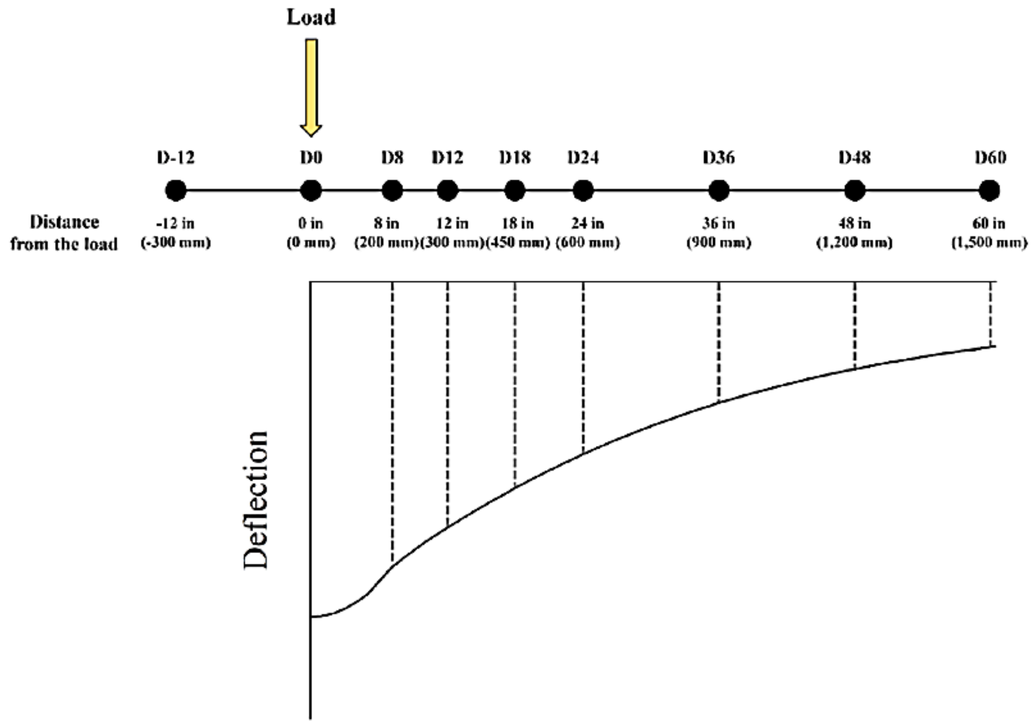

Figure 1.2 Deflection Basin and Geophone Labels (Park et al., 2022).

technique estimates the fundamental engineering properties of each pavement layer (i.e., elastic modulus) and the underlying subgrade soil (i.e., the modulus of subgrade reaction [*k*]), and is performed by processing the measured surface deflection data in a mathematical algorithm with the pavement structural information such as load magnitudes, material Poisson ratio (ν), and layer thicknesses. Technically, backcalculation involves adjusting layer stiffness values obtained from a mathematical model until the model's predicted deflection basin closely matches the measured pavement deflections through an iterative process.

Park et al. (2022) used FWD deflection basin data to predict critical strain responses in pavements and assess structural integrity through finite element modeling (FEM). This study used deflection-basin-predictive models to determine the critical tensile strain at the bottom of the asphalt layer and the vertical strain at the top of the subgrade soil. The authors demonstrated how FEM, combined with FWD deflection-basin data, can produce more representative stress-strain distributions for various pavement layers (Park et al., 2022).

Fu et al. (2024) developed a dynamic deflection prediction model for flexible pavements based on FWD impulse loading. This model addresses the limitations of static deflection-based analysis methods, which overestimate surface deflections by neglecting inertia and damping effects. The authors proposed a static-to-dynamic deflection conversion model based on the layered elastic theory (LET) and the spectral element method (SEM) to predict deflection basins with higher accuracy and lower computational time than traditional methods (Fu et al., 2024).

Cheng et al. (2021) studied the relationship between asphalt layer elastic modulus and loading conditions, both FWD and vehicular loadings. They found the modulus obtained from FWD loading tends to overestimate in-service asphalt stiffness due to the significantly shorter pulse duration loads (~ 0.03 s) compared to vehicular loading. Additionally, the elastic modulus ratio under vehicular loading to those obtained from FWD varied with loading speed and pavement temperature. Thus, the authors indicated that the conventional FWD-based backcalculation procedure may not accurately reflect in-service pavement performance.

Vyas et al. (2021) trained artificial neural networks (ANN) on a dataset, including FWD deflection basin parameters, to predict flexible pavement mechanical performance. The study aimed to minimize the frequency of FWD testing while ensuring reliable structural assessments at the network level. The authors trained multiple ANN models using data from a 77-mile pavement network, including structural, functional, environmental, and subgrade properties, to predict pavement Surface Curvature Index (SCI) and Base Curvature Index (BCI). The results demonstrated that ANN models outperformed traditional multiple linear regression methods, achieving R^2 values of up to 0.88 for SCI and 0.87 for BCI. However, these machine learning models can only estimate the deflection basin parameters for pavements whose condition falls within the range of dataset data.

In another study, Park et al. (2024) investigated using FWD deflection basin data to determine the effective structural number (SN_{eff}) of full-depth asphalt pavements. The authors developed an improved SN_{eff} prediction model by integrating FWD data with a calibrated Rohde model and eliminating negative deflection values to overcome the inaccuracies of the AASHTO

1993 method. It was found that the model indicates close agreement with the calibrated Rohde model, while offering a more practical and reliable approach for network-level pavement management system.

1.3 Dynamic Modulus Backcalculation

The dynamic modulus (E*) is a fundamental asphalt material property used in Pavement ME Design (formerly known as the Mechanistic-Empirical Pavement Design Guide [MEPDG]) to design and analyze flexible pavements. It describes the material's behavior under cyclic loading and is a key indicator of asphalt material stiffness under varying temperatures and loading frequencies. To determine *E** values without performing dynamic modulus (DM) laboratory testing, Witczak developed empirical E* predictive models based on asphalt mixture volumetric properties. However, recent pavement materials and construction advancements require more accurate models to estimate *E** values for better M&R planning.

Bari (2005) conducted a study to improve the Witczak predictive model by extending the dataset and incorporating additional variables that may affect *E** values. The model also improved the ability to predict the *E** values over a broader range of loading frequencies, temperatures, and asphalt mixture types. For this purpose, the authors analyzed data from 2,750 tests conducted on 205 asphalt mixtures to ensure the model covered various material properties, environmental conditions, and loading conditions, while advanced statistical methods were used to evaluate the significance of each variable and its interactions. The updated model better represents the viscoelastic behavior of asphalt mixtures and generates *E** values that closely match laboratory-measured results. One of the notable contributions of this research is the model's improved capability to predict *E** for different types of hot mix asphalt (HMA) mixtures, including those containing polymer-modified asphalt binders and reclaimed asphalt pavement (RAP).

Solatifar et al. (2017) formulated a methodology for improving the mechanistic-empirical rehabilitation strategies for flexible pavements. Their study highlights the significance of the *E** value in determining pavement mechanical performance. The method uses the Witczak model to generate the initial *E** master curve using volumetric properties and asphalt binder viscosity data. A critical review of their work shows that the authors incorporated a sigmoidal function in combination with a calibration factor to make the model's predictions closer to the experimental results.

Backcalculating pavement layer properties includes matching the load and deflection data from a theoretical/statistical model to the FWD deflection measurements. This process consists of two main components: (1) a theoretical model (or forward analysis) capable of simulating the FWD loading and the corresponding deflections and (2) an iterative or statistical method that determines the optimal layer parameters by minimizing the summation of errors between the measured and simulated results (Lee, 2014). The theoretical model should provide the pavement's mechanical performance under FWD loading conditions. At the same time, the statistical optimization process systematically adjusts the parameters to achieve the best fit. Many methods have been developed to backcalculate layer elastic moduli using FWD deflection-basin data using a combination of forward analysis and iterative approaches, such as EVERCALC, ELMOD, BAKFAA, and BISAR (Chen et al., 1996; Rao & Von Quintus, 2016; Tarefder & Ahmed, 2013; White, 2019).

Considering the main assumptions and estimation algorithms, there are three categories of backcalculation techniques: static, viscoelastic, and dynamic. Each category has unique merits, limitations, and areas that could benefit from further enhancement. For example, Varma et al. (2013) developed a technique using a genetic algorithm (machine learning tools) and a layered viscoelastic forward solution to determine the *E** master curve. The genetic algorithm optimizes the backcalculation process by adjusting sigmoidal function and shift factor polynomial coefficients to reflect the laboratory-measured data closely. The initial goal was to identify optimal temperatures for FWD testing so a larger part of the *E** master curve could be accurately backcalculated. The research indicated that an accurate backcalculation requires FWD tests at various temperatures. to more accurately determine the pavement's *E** master curve. The techniques would be further enhanced if it used the time-temperature superposition principle to generate a more accurate *E** master curve.

Zhao et al. (2022) performed a study to evaluate the reliability of backcalculating the elastic modulus using a set of parameters from FWD deflection basins and Ground Penetrating Radar (GPR) to improve the accuracy of modulus estimation for flexible pavements. The study proved that traditional numerical models, which assume idealized pavement structures, may result in significant inaccuracies, with differences as high as 64% between backcalculated modulus values and laboratory-measured values. To overcome this limitation, the authors proposed an improved numerical model including actual pavement layer thickness, Poisson's ratio, and the initial modulus range (seed values). This improvement reduced the relative error of backcalculated modulus estimates to within ±4%, demonstrating the advantages of integrating GPR data with the FWD backcalculation process. Additionally, the study evaluated several regression models, including exponential, parabolic, and sigmoidal, to fit theoretical deflection basins and optimize the relationship between deflection basin parameters and pavement structural properties. The findings showed the sigmoidal regression model provided the most accurate fit, resulting in modulus values closely aligned with laboratory-measured E* results. Moreover, the authors noted that the type of regression model significantly impacts the backcalculated deflection basin, with improper selection potentially resulting in a deviation exceeding 30%.

Static forward solution backcalculation techniques work on the assumption that a pavement structure is in static equilibrium. Such methods neglect the time-dependent nature of asphalt materials, which causes inaccuracies in backcalculated elastic modulus values. Viscoelastic backcalculation methods, on the other hand, consider the time-dependent properties of asphalt materials, providing a more accurate simulation of FWD testing conditions (Kutay et al., 2011). However, they often fail to consider the full effects of wave propagation essential for dynamic loading conditions, i.e., a time delay between measured deflection and applied load (Lee, 2014). Dynamic backcalculation methods address these limitations by introducing wave propagation phenomena and using viscoelastic principles. However, traditional dynamic methods rely on discrete Fourier transforms (DFT), which are prone to errors due to signal truncation and noise sensitivity when dealing with transient, nonperiodic signals like FWD impulse loading. Despite recent advancements, it is necessary to improve methodologies for accurately estimating the dynamic response of flexible pavement. More sophisticated tools like ViscoWave (30) integrate continuous integral transforms to better handle transient signals. The ViscoWave software is capable of generating E^* values based on FWD time history data.

1.4 Backcalculation Methods

To date, most backcalculation efforts using field FWD data have focused on determining the elastic modulus of pavement layers by matching the measured deflection basin to one generated analytically (Öcal, 2014; Sangghaleh et al., 2014; Satyanandam et al., 2023). The core algorithm of these methods minimizes the absolute or squared errors between the calculated and measured deflection basins, typically by applying weighting factors to each geophone. However, these approaches assume that the pavement behaves purely elastically under impulse loading, neglecting the viscoelastic behavior of asphalt mixtures as well as the inertial and damping effects.

Many static backcalculation techniques rely on Boussinesq's solution to determine the stress at any point within the pavement structure, assuming a pavement behaves as a homogeneous, isotropic half-space medium (Lei, 2011). For example, KENLAYER is a software tool developed for analyzing the interface conditions between pavement layers, using static techniques (Gupta & Kumar, 2014; Omer & Eghan, 2018). As mentioned earlier, static backcalculating methods estimate pavement layer stiffness by iteratively adjusting forward-calculated deflections to match field-measured FWD data. There are three common methods for making these adjustments: (1) iterative optimization, (2) database-driven methods, and (3) regression-based modeling. Although static methods are widely used in pavement engineering, they are based on elastic assumptions that fail to account for the viscoelastic and dynamic characteristics of flexible pavements.

In contrast, dynamic backcalculation methods use damped-elastic finite layer or finite element forward models. Finite layer solutions follow Kausel's formulation (Kausel & Peek, 1982), divide the total pavement layer into small-thickness layers, allowing algebraic approximations of transcendental functions (Endiran 1999). Al-Khoury et al. (2001) developed LAMDA, which uses spectral element-based solution models. Unlike traditional methods, LAMDA treats each pavement layer as a single element, avoiding the need to subdivide the pavement into sub-layers, thereby reducing processing in the iterative algorithm. Additionally, Endiran (1999) introduced DYNARK, a nonlinear dynamic model that defines granular materials and subgrade nonlinearity behavior.

Dynamic backcalculation solutions can be formulated in either the frequency or time domain. Frequency-domain methods use Fast Fourier Transforms (FFT) to convert load and deflection times into specific frequency ranges, matching steady-state (complex) deflection basins to geophone responses. This approach is computationally efficient and theoretically robust, but it is highly sensitive to truncation errors, sampling intervals, and rest periods. Time-domain backcalculation, on the other hand, directly compares measured and simulated deflection histories over any chosen time interval. This method allows for more flexible matching but requires extensive output data from forward models and can complicate the statistic convergence process. Table 1.1 summarizes the current backcalculation techniques or software developed.

The PAVEMENT ME uses the E^* master curve as key input data; however, obtaining it through laboratory testing is time consuming and costly. Therefore, backcalculation of E^* from FWD time history data facilitates the process and provides a more precise assessment of the pavement's remaining service life, leading to better-informed M&R decisions.

1.5 Problem Statement

Despite continuous efforts to improve dynamic backcalculation techniques, the results have often shown fair to poor success, indicating persistent challenges. This difficulty arises primarily from the inherent complexities of modeling transient, nonperiodic signals generated by FWD tests, often inadequately addressed by traditional discrete Fourier transform (DFT)

TABLE 1.1
Current FWD Backcalculation Software (Endiran, 1999; Hajj et al., 2024; Huang, 1993; Lee, 2014; Liu & Scullion, 2001; Sivaneswaran et al., 1991; Strickland, 2001; Von Quintus et al., 2015; Washington State Department of Transportation, 2005).

Software	Developer	Methodology and Feature
ViscoWave	Michigan State University and ARA	Generate dynamic modulus value by using dynamic finite layer method
EVERCAL	Washington State DOT	Estimate the elastic modulus by using iterative optimization and layered elastic analysis
MODULUS 7.0	Texas A&M (TTI)	Uses linear elastic theory to generate data for FWD deflection basins
ELMOD	Dynatest	Estimate the elastic modulus using FEM, Linear Elastic Theory and Method of Equivalent Thickness (MET)
BISAR	Shell	Estimate the layer stiffness by using multi-layer elastic theory
KENLAYER/KENPAVE	University of Kentucky	Analyze pavement based on elastic multilayer theory
WESLEA	US Army of Corps of Engineering	Developed based on static elastic layer analysis
BAKFAA	Federal Aviation Administration (FAA)	Estimate elastic modulus based on the layered elastic analysis program

methods. The short loading duration, high sensitivity, and failure to consider wave propagation effects in existing solutions highlight the need for a more accurate approach. Advanced methodologies, such as those using continuous integral transforms, offer potential improvements, yet the field seeks more accurate and reliable procedures to backcalculate the *E** master curve.

1.6 Objectives

This study aims to overcome the limitations of current dynamic backcalculation techniques by developing a mechanistic-based algorithm for predicting the *E** master curve using FWD time history data. This approach is designed to account for the time-dependent nature of pavement responses to FWD impulse loading, incorporating viscoelastic principles. The efficiency of the proposed model will be validated by comparing its results with those obtained from existing methods and laboratory tests of field-cored specimens. Ultimately, the developed model aims to provide greater accuracy in predicting the *E** master curve.

2. BACKGROUND

2.1 Introduction to Viscoelasticity

Three fundamental parameters that describe the mechanics of a continuous medium are strain, stress, and displacement (Malvern, 1969). These parameters are interrelated through three key types of equations, known as laws of nature: (a) constitutive equations, (b) kinematic relations, and (c) equilibrium conditions (Flügge, 1967).

Equilibrium conditions are concerned with stress quantities and typically involve their spatial derivatives. These conditions can be expressed for either an infinitesimal or a finite piece of material, sometimes with an additional loading term on the right-hand side. Since the displacement of every point in a material completely defines its deformation, the corresponding strains can be determined from these displacements. The equations that describe the relationship between strain and displacement are known as kinematic relations, which form the second set of elasticity equations (Lakes, 2009).

The first two sets of equations—equilibrium conditions and kinematic relations—are independent of the material itself. The equilibrium conditions ensure that forces are balanced, while the kinematic relations describe how displacement corresponds to strain. In contrast, constitutive equations are material-dependent, defining the relationship between stress and strain based on the material's properties. In the simplest case, six equations directly relate the six stress components to the corresponding strain components. When these equations are linear, they are known as Hooke's law (Hajikarimi & Hosseini, 2023).

Many materials exhibit various behaviors that lead engineers to propose several idealized models. These models account for different ways a material responds to stress or strain. For example, an elastic material shows a direct, one-to-one relationship between stress and strain: it deforms under load but returns to its original shape once the load is removed. On the other hand, plastic materials display more complex behavior than elastic materials, as outlined below:

- They behave like elastic materials until the yield limit is reached.
- Beyond the yield limit, additional deformation occurs without an increase in stress, a phenomenon known as *plastic flow*.
- This extra deformation is permanent and cannot be recovered, even after the load is removed.
- This material type is time-independent, as the fundamental equations do not account for the strain rate.

Some materials are significantly affected by the rate at which they are loaded (loading rate). In these materials, more gradual increases in stress often result in larger strains. These materials can also exhibit creep behavior, where deformation continues to increase over time under a constant load, and the rate of strain depends on the applied stress (Hajikarimi & Hosseini, 2023). Such materials are referred to as viscoelastic, like asphalt.

The constitutive equations for viscoelastic materials can be either linear or nonlinear, depending on the loading conditions, to describe the strain-stress relationship. Unlike elastic materials, which respond instantaneously to applied stress, viscoelastic materials show time-dependent behavior under load. This means that their deformation evolves over time, influenced by the magnitude of the applied stress or strain. Two key characteristics of the time-dependent behavior of viscoelastic materials are creep and stress relaxation.

2.2 Creep Behavior

Creep is the tendency of viscoelastic materials to deform continuously under constant applied stress (Hajikarimi & Hosseini, 2023). This behavior is important in flexible pavements, where continued loads from traffic and the environment can lead to long-term deformation. Viscoelastic materials experience three stages of creep:

- Transient stage (primary creep): The deformation rate is initially high but gradually decreases over time as internal resistance builds.
- Steady-state stage (secondary creep).
- Failure stage (tertiary creep).

For a viscoelastic material subjected to constant uniaxial stress (σ_0), the total strain $\varepsilon(t)$ at any given time t can be expressed using the creep function J(t), as shown in Equation 2.1:

$$\varepsilon(t) = J(t)\sigma_0 \qquad \text{(Eq. 2.1)}$$

where, J(t) is the creep compliance function in 1/Pa (m^2/N), σ_0 is the constant applied stress in Pa (N/m^2), and $\varepsilon(t)$ is the time-dependent strain response (dimensionless).

2.2.1 Characteristics of the Creep Function

In the linear viscoelastic medium, the creep compliance is independent of stress level. The initial strain observed in the creep curve is commonly ascribed to instantaneous elasticity. However, a load cannot be applied instantaneously; instead, the material exhibits a natural, time-dependent response.

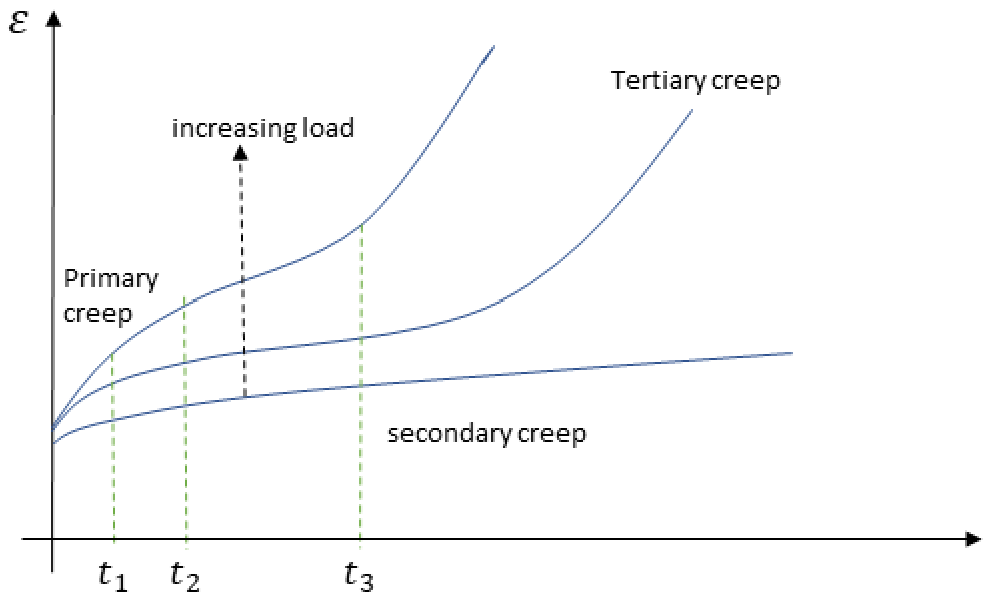

Figure 2.1 Creep Behavior at Different Regions.

Creep behavior is typically divided into three stages (Figure 2.1, Flügge, 1967; Hajikarimi & Nejad, 2021). In the initial creep phase or primary stage, the curve shows a smooth upward behavior that indicates a deceleration in the deformation rate. This is followed by the secondary creep phase, where strain increases linearly with time (considered a constant strain rate). However, the straight-line appearance in a strain-versus-time plot does not imply a linear viscoelastic response; both secondary and tertiary creep generally involve nonlinear viscoelasticity behavior. In tertiary creep, the deformation rate accelerates until the material eventually fails (Hajikarimi & Nejad, 2021).

A linear viscoelastic response is characterized by a direct proportionality between applied stress and the resulting strain at a given time. To evaluate this, one can compare stress and strain data at constant times, so-called isochronal plots (Lakes, 2009). For example, Figure 2.1 illustrates data points taken at times t_1, t_2, and t_3. If the plot of stress versus strain at any fixed time yields a straight line, the material may be considered to show linear behavior. Despite the linear appearance of secondary creep in time-dependent plots, its behavior is almost always nonlinear, even under a small strain level.

The creep function denoted as $J(t)$, contains several key behaviors that describe a material's response under continuous constant stress. At the initial moment ($t = 0$), many materials display an instantaneous elastic response, characterized by an immediate strain increase, as shown in Equation 2.2.

$$\sigma(0) = E_0\varepsilon_0 \qquad \text{(Eq. 2.2)}$$

where E_0 is the instantaneous modulus. This instantaneous displacement is just the beginning of the deformation process. Over time, as the material is subjected to a constant load, additional strain accumulates, a phenomenon referred to as time-dependent strain growth (Hajikarimi & Hosseini, 2023). Depending on the material, this deformation might eventually stabilize into a steady-state or asymptotic behavior, where the strain increases consistently. In some instances, however, the material may keep deforming indefinitely until it fails. Furthermore, if the applied stress is removed at a specific time ($t = t_r$), certain materials show a recovery phase where the accumulated strain slowly returns to its original state, indicating a partial reversal of the deformation. The precise functional form of $J(t)$ depends on the material's constitutive model, which defines the underlying stress-strain and time relationship and captures the complex interplay of elastic, viscous, and plastic responses during creep (Lakes, 2009).

2.3 Relaxation

In viscoelastic materials, stress relaxation is the phenomenon where stress gradually decreases over time when the material is subjected to a constant strain. For example, if a strain of magnitude ε_0 is applied as a step function at time zero, then:

$$\varepsilon(t) = \varepsilon_0 \mathrm{H}(t) \qquad \text{(Eq. 2.3)}$$

where $H(t)$ is the Heaviside step function and ε_0 is the applied strain magnitude. As such, the relaxation modulus $E(t)$ can be simply described as:

$$\mathrm{E}(t) = \frac{\sigma(t)}{\varepsilon_0} \qquad \text{(Eq. 2.4)}$$

In this equation, $\sigma(t)$ is the applied stress, and $E(t)$ is the relaxation modulus as a function of time. In linear viscoelastic materials, $\mathrm{E}(t)$ depends solely on time and is independent of the strain level. In uniaxial tension and compression mode, the symbol E represents Young's modulus which describes the material's stiffness in a one-dimensional direction (Lakes, 2009).

2.4 Constitutive Relationships

Constitutive equations are widely used to accurately predict the response of a viscoelastic material under a strain history or arbitrary load. These equations extend the analysis beyond simple creep and relaxation properties, providing a comprehensive framework for predicting the material's actual behavior. These equations can be used to determine the recovery characteristic of a viscoelastic material by using the Boltzmann Superposition principle.

2.4.1 Recovery Determination from Relaxation

The creep and relaxation characteristics discussed in Sections 2.2 and 2.3 enable the prediction of a viscoelastic material's response when subjected to a stress or strain step function. However, constitutive equations must be used to predict the behavior under any arbitrary time-dependent load or deformation. This analysis focuses on isothermal, one-dimensional deformations. While the symbol *E* is used here to denote the elastic modulus, the same principles apply to shear deformations, with the corresponding modulus *G*, and to volumetric deformations, where the bulk modulus *B* (referred to as *K*) is relevant. Before detailing this section, it is necessary to describe some of the mathematical principles used in this study.

2.4.2 Boltzmann Superposition Principle

The Boltzmann Superposition Principle is a key concept in linear viscoelasticity. It explains that the response of a viscoelastic material at any given time is the cumulative effect of all previous stress or strain increments (Shukla & Joshi, 2017). This principle is based on two main assumptions (Hajikarimi & Nejad, 2021):

- Linearity: The material's response to a load is directly proportional to the magnitude of that load.
- Time Invariance: The material properties remain constant over time as long as it stays within its linear region.

Because of these assumptions, the total response (stress or strain) of a linear viscoelastic material is the summation of its individual responses to each load step over time.

2.4.2.1 Stress Response to a Strain History. An arbitrary uniaxial stress history is shown in Figure 2.2 as an input excitation function. The total duration of stress application is divided into *n* small time intervals, as therefore, it is reasonable to assume that the applied stress remains constant at a value of $\Delta\sigma$ within each time interval. Given the creep compliance (D(t)) of the viscoelastic material, the corresponding strain increment $\Delta\varepsilon(t)$ at time ξ can be determined using Equation 2.5:

$$\Delta\epsilon(t) = D(t-\xi)\Delta\sigma \qquad \text{(Eq. 2.5)}$$

It is feasible to sum the corresponding strains over the full loading history (n-time steps) as:

$$\epsilon(t) = \sum_{i=0}^{n}\left[\Delta\sigma_i D(t-\xi_i)\right]\times\frac{\Delta\xi_i}{\Delta\xi_i} = \sum_{i=0}^{n}\frac{\Delta\sigma_i}{\Delta\xi_i}D(t-\xi_i)\times\Delta\xi_i \qquad \text{(Eq. 2.6)}$$

Considering an infinitesimal stress increment, $d\sigma$, applied at time ξ, the differential form of Equation 2.6 can be expressed as:

$$\epsilon(t) = \int_{-\infty}^{t} D(t-\xi)\frac{d\sigma(\xi)}{d\xi}d \qquad \text{(Eq. 2.7)}$$

Equation 2.7 is applicable when the stress history $\sigma = \sigma(\xi)$ is smooth; however, if the stress history exhibits a nonsmooth trend, then the differential in Equation 2.8 should be used.

$$\epsilon(t) = \int_{-\infty}^{t} D(t-\xi)d\sigma(\xi) \qquad \text{(Eq. 2.8)}$$

Traditionally, hereditary integral constitutive equations start with a lower integration limit of -∞. If it is assumed that an instantaneous loading is applied at time zero, then the stress history can be written as a function of time:

$$\sigma(t) = \begin{cases} 0 & when\, t < 0 \\ \sigma_0 + \sigma_1(t); \quad \sigma_1(0) = 0 & when\, t \geq 0 \end{cases} \qquad \text{(Eq. 2.9)}$$

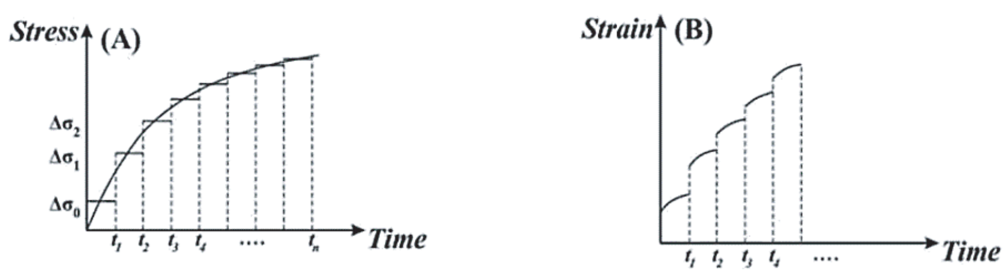

(a) (b)

Figure 2.2 (a) An Arbitrary Uniaxial Stress History, and (b) Corresponding Strain for Each Time Interval.

Next, the strain can be determined by discretizing integration limits as shown in Equation 2.10:

$$\epsilon(t) = \int_{-\infty}^{0^-} D(t-\xi)d\sigma(\xi) + \int_{0^-}^{0^+} D(t-\xi)d\sigma(\xi) + \int_{0^+}^{t} D(t-\xi)d\sigma(\xi)$$
$$= 0 + D(t)\sigma_0 + \int_{0^+}^{t} D(t-\xi)d\sigma(\xi) \qquad \text{(Eq. 2.10)}$$

For example:

$$\epsilon(t) = D(t)\sigma_0 + \int_{0^+}^{t} D(t-\xi)d\sigma(\xi) \qquad \text{(Eq. 2.11)}$$

Figure 2.3 illustrates a typical uniaxial strain excitation function along with its associated stress response. Following the same method used to determine strain from a stress excitation function, it is possible to divide the total duration of strain application into *n* small time intervals. It is reasonable to assume that the applied strain remains constant at a value of $\Delta\sigma$ during each interval. With the relaxation modulus of a viscoelastic material, *E(t)*, the corresponding stress, $\Delta\sigma$, can be calculated at time ξ using the following equation.

$$\Delta\sigma(t) = E(t-\xi)\Delta \qquad \text{(Eq. 2.12)}$$

The total stress over entire strain history (n time steps) can be expressed as:

$$\sigma(t) = \sum_{i=0}^{n}\left[\Delta\epsilon_i E(t-\xi_i)\right]\times\frac{\Delta\xi_i}{\Delta\xi_i} = \sum_{i=0}^{n}\frac{\Delta\epsilon_i}{\Delta\xi_i}E(t-\xi_i)\times\Delta\xi_i \qquad \text{(Eq. 2.13)}$$

Assuming an infinitesimal strain change ($d\varepsilon$) applied at time ξ, the differential form of Equation 2.13 is:

$$\sigma(t) = \int_{-\infty}^{t} E(t-\xi)\frac{d\epsilon(\xi)}{d\xi}d \qquad \text{(Eq. 2.14)}$$

This equation applies when the strain history $\varepsilon = \varepsilon(\xi)$ is smooth; however, in case of nonsmooth strain history, the integration in Equation 2.15 should be used:

$$\sigma(t) = \int_{-\infty}^{t} E(t-\xi)d\epsilon(\xi) \qquad \text{(Eq. 2.15)}$$

Considering an infinitesimal strain increment ($d\varepsilon$), the immediate strain can be taken out from the differential form of Equation 2.15, as shown in Equation 2.16:

$$\sigma(t) = E(t)\epsilon_0 + \int_{0^+}^{t} E(t-\xi)d\epsilon(\xi) \qquad \text{(Eq. 2.16)}$$

Boltzmann's principle can be used to determine the recovery expression from relaxation modulus. To do this, it is necessary to determine the strain in a relaxation and recovery test initially by considering the linearity in the material behavior for predicting the resulted stress history. By inspiring from Figure 2.4, it is possible to convert the strain function (Equation 2.3) into a superposition form as:

$$\epsilon(t) = \epsilon_0\left[H(t) - H(t-t_1)\right] \qquad \text{(Eq. 2.17)}$$

Therefore, by applying the Boltzmann superposition principle on Equation 2.17, the stress, shown in Figure 2.4, can be determined as:

$$\sigma(t) = \epsilon_0\left[E(t) - E(t-t_1)\right] \qquad \text{(Eq. 2.18)}$$

The stress produced by a delayed strain step, represented as $\varepsilon_0 H(t - t_1)$, has the same time-history form as $\varepsilon_0 E(t - t_1)$. This similarity occurs because the stress responses ε_0 *E(t)* from an earlier strain step ε_0 H(t), are simply shifted in the time domain. This relationship applies only to nonaging materials, which maintain consistent mechanical properties over time. Depending on the material type, the strain may or may not recover fully to zero as it becomes larger, a phenomenon commonly known as recovery or the elastic after-effect.

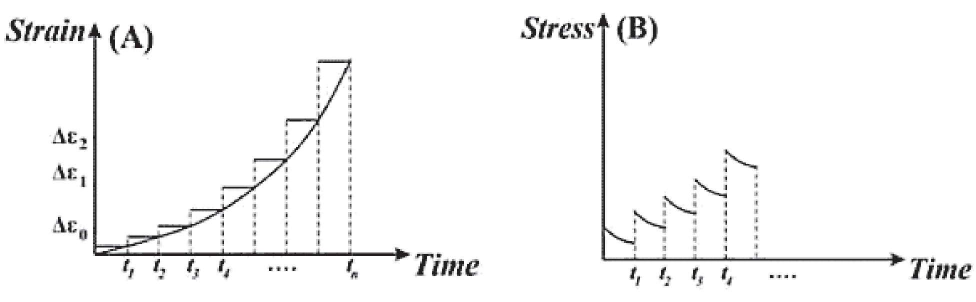

(a) (b)

Figure 2.3 Boltzmann's Superposition Principle for (a) an Arbitrary Uniaxial Strain History and (b) Responded Stress at Each Time Step *n*.

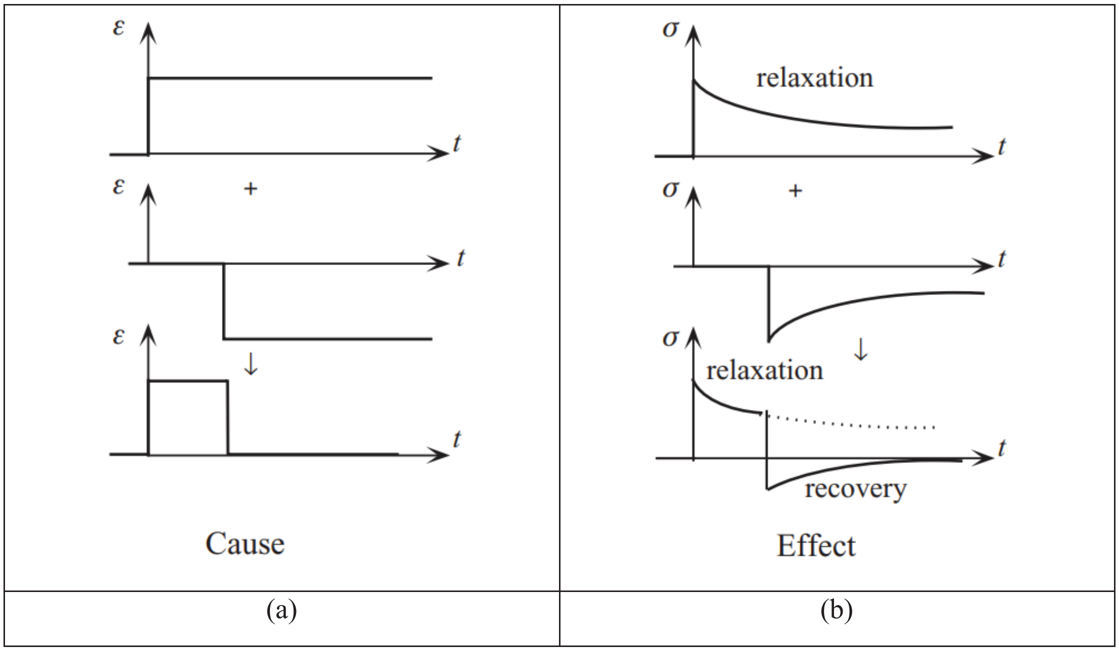

Figure 2.4 (a) The Summation of Strain Steps Over Time. (b) Recovery Curve of Stress (σ) Created by the Superposition of Individual Relaxation Curves.

2.5 Relation Between Creep and Relaxation

There are various ways to determine the relationship between creep and relaxation. The most well-known are Laplace transforms, which are constructed by direct inter-relation-driven equations.

2.5.1 Laplace Transform

The Laplace transform is an effective method for transforming linear ordinary differential equations into algebraic ones, which makes solving them easier. This transform substitutes differentiation in the time domain with multiplication in the frequency domain. In linear viscoelastic analysis, the creep function *J(t)* and the relaxation function *E(t)* are interconnected through integral equations derived from the Boltzmann superposition principle. Integral transforms, such as Laplace or Fourier transforms, can transform these integral equations from convolution-type expressions into algebraic forms. In the context of linear viscoelasticity, the relationships between *J(t)* and *E(t)* are often implicit. Explicit formulas can be derived by applying the Laplace transform to a specific analytical form *E(t)* or *J(t).* Considering *s* as the transform variable, it is possible to use derivation and convolution theorems to convert constitutive equations. As such, the relaxation modulus and creep compliance functions can be written by transforming these functions into the s-domain as:

$$\frac{\sigma(s)}{\epsilon(s)} = sE(s), \quad \frac{\sigma(s)}{\epsilon(s)} = \frac{1}{sJ(s)} \qquad \text{(Eq. 2.19)}$$

$$E(s)J(s) = \frac{1}{s^2} \qquad \text{(Eq. 2.20)}$$

Using the inverse transform in conjunction with the convolution theorem and the known relation $L[t]=1/s^2$, the following expression is derived:

$$\int_0^t J(t-\tau)E(\tau)d\tau = \int_0^t E(t-\tau)J(\tau)d\tau = t \qquad \text{(Eq. 2.21)}$$

An alternative formulation can be derived by rearranging the given relation in the Laplace domain and using the expression $sL[t]=1/s$, thus:

$$1 = J(0)E(t) + \int_0^t E(t-\tau)\frac{dJ(\tau)}{d\tau}d\tau \qquad \text{(Eq. 2.22)}$$

The relationships are implicit. However, explicit relationships can be established by using Laplace transformations if a specific analytical form for *J(t)* or *E(t)* is provided.

2.5.2 Direct Construction $J(t) \leftrightarrow E(t)$

Instead of using Laplace transform functions, it is possible to derive any solution by direct formulation. Specifically, the strain response (ε(t)), caused by a constant stress (σ_c) can be represented as the sum of an instantaneous component, *H*(*t*), and a series of time-dependent Heaviside step functions that account for the delayed response as shown in Equation 2.23.

$$\epsilon(t) = \epsilon(0)H(t) + \sum_{i=0}^{N} \Delta\epsilon_i H(t-t_i) \qquad \text{(Eq. 2.23)}$$

Each incremental strain step in the summation (Figure 2.5.a) generates a corresponding stress relaxation component (Figure 2.5.b). For a linear material, the modulus stays constant regardless of strain, which means that the effects of each individual strain step in the summation do not influence one another. Consequently, the total stress response to this strain history is obtained by superimposing the respective relaxation components.

2.6 Viscoelastic Mechanical Models

Viscoelastic materials exhibit a combination of elastic and viscous behavior under mechanical loading that require specialized models to accurately characterize their time-dependent stress-strain behavior. To this end, mechanical analogs composed of springs (representing pure elasticity) and dashpots (representing viscosity) are widely used. These models can be categorized into integer-order and fractional-order formulations. Integer-order models, such as the Maxwell, Kelvin-Voigt, and Standard Linear Solid (SLS) models, rely on classical differential equations with integer-order derivatives to describe the material's creep and relaxation behavior. While effective in specific cases, they often fail to accurately represent the broad frequency-dependent behavior observed in real viscoelastic materials (Hajikarimi & Nejad, 2021). In contrast, fractional-order models use fractional derivatives of noninteger order to provide a more accurate and generalized description of viscoelastic behavior. These models account for the continuous relaxation spectrum of materials, offering improved accuracy in predicting stress relaxation, creep compliance, and dynamic modulus over a wide range of loading conditions. As a result, fractional-order viscoelastic models have been increasingly used in advanced flexible pavement analysis, biomaterials, and polymer engineering due to their superior ability to describe material behavior across different time scales (Hajikarimi & Hosseini, 2023; Hajikarimi & Nejad, 2021).

2.6.1 Integer-Order Differential Models

In the context of integer-order differential equations, two fundamental mechanical elements, the linear spring and the dashpot, are typically used to represent viscoelastic behavior. A linear spring obeys Hooke's law, capturing ideal elastic properties where stress is directly proportional to strain. In contrast, a dashpot follows Newton's law, modeling purely viscous behavior with stress proportional to the rate of strain. All integer-order viscoelastic models can be formulated by various series or parallel combinations of these two components. Figure 2.6 depicts both the linear spring and the dashpot, along with their corresponding stress-strain relationships as described by Equations 2.24 and 2.25:

$$\sigma_e = E \times \varepsilon_e \qquad \text{(Eq. 2.24)}$$

$$\sigma_\upsilon = \eta \times \dot{\varepsilon}_\upsilon \qquad \text{(Eq. 2.25)}$$

where, σ is the applied stress (Pa), ε the corresponding strain (dimensionless), E is the linear spring stiffness (Pa), and η is the dashpot viscosity coefficient (Pa.s).

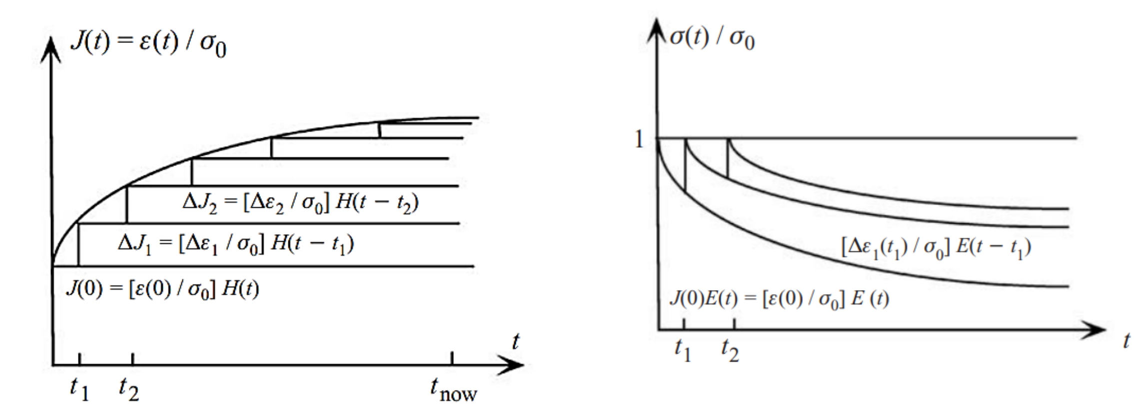

(a) (b)

Figure 2.5 Creep Function Decomposition: (a) Summation of Delayed and Immediate Heaviside Step Functions, and (b) Corresponding Summation of Relaxing Components.

(a) (b)

Figure 2.6 Primary Components of Integer-Order Viscoelastic Models: (a) Linear Spring, and (b) Dashpot.

2.6.1.1 Maxwell Model. The well-known Maxwell model consists of a linear spring and a dashpot connected in series, as illustrated in Figure 2.7. In this configuration, the stress remains uniform across both elements, while the total strain of the model is determined as:

$$\varepsilon = \varepsilon_{\varepsilon} + \varepsilon_{\upsilon} \rightarrow \dot{\varepsilon} = \dot{\varepsilon}_{\varepsilon} + \dot{\varepsilon}_{\upsilon} \qquad \text{(Eq. 2.26)}$$

As seen in Equation 2.26, the total strain of the Maxwell model can be written in the first derivative format, and can therefore be re-written as:

$$\dot{\varepsilon} = \frac{\dot{\sigma}}{E} + \frac{\sigma}{\eta} \qquad \text{(Eq. 2.27)}$$

A creep tests under applied stress is assumed to determine the constitutive functions of the Maxwell models, including E(t) and J(t). As therefore, Equation 2.27 can be written as:

$$\frac{d\varepsilon}{dt} = \frac{1}{E}\frac{d\sigma}{dt} + \frac{\sigma}{\eta} \Rightarrow d\varepsilon = \frac{1}{E}d\sigma + \frac{\sigma}{\eta}dt$$

$$\int_0^t d\varepsilon = \int_0^t \frac{1}{E}d\sigma + \int_0^t \frac{\sigma}{\eta}dt \Rightarrow \varepsilon(t) = \left(\frac{1}{E} + \frac{t}{\eta}\right)\sigma_0 \qquad \text{(Eq. 2.28)}$$

Considering the definition of creep compliance, the creep function of the Maxwell model is represented as:

$$D(t) = \frac{\varepsilon(t)}{\sigma_0} = \frac{1}{E} + \frac{t}{\eta} \qquad \text{(Eq. 2.29)}$$

A thorough analysis of the Maxwell model reveals that displacement in the viscous (dashpot) component is irrecoverable upon unloading. As a result, the model alone fails to represent the full viscoelastic behavior of asphalt materials, which typically exhibit both recoverable and nonrecoverable deformation characteristics. Similarly, for a relaxation test under an applied strain, the final E(t) of the Maxwell model can be represented as:

$$E(t) = \frac{\sigma(t)}{\varepsilon_0} = E\exp\left(-\frac{E}{\eta}t\right) \qquad \text{(Eq. 2.30)}$$

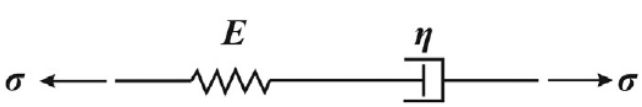

Figure 2.7 Maxwell Model.

2.6.1.2 The Kelvin Model. The Kelvin model consists of a linear spring and a viscos dashpot in parallel, as shown in Figure 2.8. Unlike the Maxwell model, the applied stress is distributed across both elements, while the strain remains equal for each component.

The simple stress-strain relationship in this model can be written as:

$$\varepsilon = \varepsilon_e = \varepsilon_v \qquad \text{(Eq. 2.31)}$$

$$\sigma = \sigma_e + \sigma_v \qquad \text{(Eq. 2.32)}$$

$$\sigma = E\varepsilon_e + \eta\dot{\varepsilon}_v \Rightarrow \sigma = E\varepsilon + \eta\dot{\varepsilon} \qquad \text{(Eq. 2.33)}$$

The constitutive functions of the Kelvin model are:

$$t = 0 \Rightarrow \varepsilon = 0 \Rightarrow \varepsilon(t) = \frac{\sigma_0}{E}\left[1 - \exp\left(\frac{-E}{\eta}t\right)\right] \qquad \text{(Eq. 2.34)}$$

$$D(t) = \frac{\varepsilon(t)}{\sigma_0} = \frac{1}{E}\left(1 - \exp\left[\frac{-E}{\eta}t\right]\right) \qquad \text{(Eq. 2.35)}$$

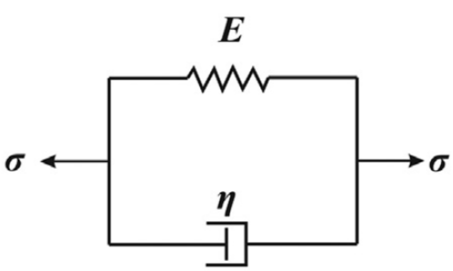

Figure 2.8 The Kelvin Model.

Unlike the Maxwell model, the Kelvin model (sometimes called the Kelvin–Voigt model) demonstrates a complete recovery of strain because the strain in the dashpot eventually returns to zero. However, a significant limitation of this model is that it does not account for instantaneous recovery upon unloading, thus restricting its use as a sole representation of viscoelastic behavior. Furthermore, because the dashpot and spring are arranged in parallel, the dashpot behaves like a rigid element at t = 0 which requires an infinitely large stress for any immediate deformation at the initial loading moment.

2.6.1.3 Burger Model. To overcome the limitation of both the Maxwell and Kelvin models, the Burger Model was introduced to more accurately characterize viscoelastic behavior by connecting a Kelvin to a Maxwell model as shown in Figure 2.9.

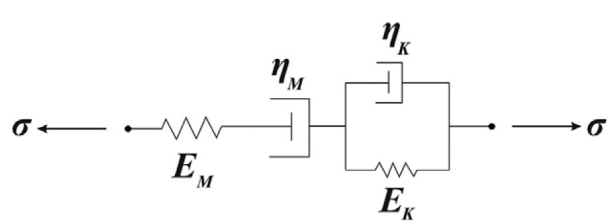

Figure 2.9 The Burger Model.

According to the configuration of the Burger model, the stress and strain can be written as:

$$\sigma_B = \sigma_M = \sigma_K \quad \text{(Eq. 2.36)}$$

$$\varepsilon_B = \varepsilon_M + \varepsilon_K \quad \text{(Eq. 2.37)}$$

Given the strain in each element, the total strain and creep compliance of the Burger model can be expressed as:

$$\varepsilon(t) = \sigma_0 \left[\underbrace{\left(\frac{1}{E_M} + \frac{t}{\eta_M} \right)}_{\text{Maxwell model}} + \underbrace{\frac{1}{E_K}\left(1 - \exp\left(\frac{-E_K}{\eta_K} t \right) \right)}_{\text{Kelvin model}} \right] \quad \text{(Eq. 2.38)}$$

$$D(t) = \frac{1}{E_M} + \frac{t}{\eta_M} + \frac{1}{E_K}\left(1 - e^{\frac{-E_K}{\eta_K} t} \right) \quad \text{(Eq. 2.39)}$$

All these integer-order differential models are limited to specific frequency ranges or loading times, restricting their ability to accurately describe viscoelastic behavior across varying conditions. To overcome this limitation, researchers have established that connecting multiple Kelvin models in series or Maxwell models in parallel allows for a more comprehensive representation of viscoelastic material properties over a broader frequency spectrum. This configuration, known as the Generalized Maxwell Model (for parallel Maxwell elements) or the Generalized Kelvin Model (for series Kelvin elements), effectively describes the time-dependent mechanical response of viscoelastic materials. The Generalized Maxwell Model is particularly useful in stress relaxation analysis, as the combination of multiple Maxwell elements allows for an extended range of relaxation times. Conversely, the Generalized Kelvin Model is often used in creep analysis, where a series of Kelvin elements enables a more accurate representation of material deformation under applied loading.

2.6.2 Fractional-Order Differential Model

In the viscoelastic modeling of asphalt materials, many integer-order viscoelastic elements are required to accurately describe the time-dependent mechanical behavior of asphalt mixtures. For example, 8 to 25 Maxwell elements must be connected in parallel to sufficiently describe viscoelastic response under varying loading conditions (Hajikarimi & Nejad, 2021). In this case, accurate representation of viscoelastic responses requires a large number of model parameters, which significantly increases computational complexity and processing time. To address this limitation, it is reasonable to develop models that require fewer parameters while maintaining high accuracy.

A promising solution is the use of fractional-order differential models, which provide a more compact yet highly effective representation of viscoelastic behavior. One of the most successful models in this category is the Huet-Sayegh (HS) model, which has been widely used to characterize the rheological properties of asphalt mixtures. For instance, Graziani et al. (2020) successfully applied the HS model to describe the viscoelastic behavior of cold-recycled mix asphalt (CMA), demonstrating its ability to accurately capture the frequency-dependent modulus of asphaltic materials with significantly fewer parameters than traditional integer-order models. Later, Olard and Di Benedetto introduced a 2S2P1D fractional-order model that includes two elastic spring (2S), two parabolic dashpot (2P), and one linear dashpot (1D). This model has been widely used in multi-scale modeling of the linear viscoelasticity of asphalt materials (Mangiafico et al., 2019). Figure 2.10 illustrates the 2S2P1D model, which includes seven constants that need to be specified for determining the entire linear viscoelastic behavior of the asphalt mixtures at a given temperature.

The complex modulus in this model can be determined by the equation:

$$E^*(i\omega\tau) = E_0 + \frac{E_\infty - E_0}{1 + \delta(i\omega\tau)^{-k} + (i\omega\tau)^{-h} + (i\omega\beta\tau)^{-1}} \quad \text{(Eq. 2.40)}$$

where the δ, β, K, τ_0, E_0, E_∞ are the model constants, E^* is dynamic modulus, and ω is the loading frequency.

2.7 Time-Temperature Superposition

Up to this point, isothermal conditions have been assumed. However, the material viscoelastic behavior is influenced not only by time t but also by temperature, *T*. For instance, the relaxation function can be expressed as a function of time and temperature as:

$$E = E(t, T) \quad \text{(Eq. 2.41)}$$

Consider a material where viscoelasticity originates from processes such as molecular rearrangements or stress-induced

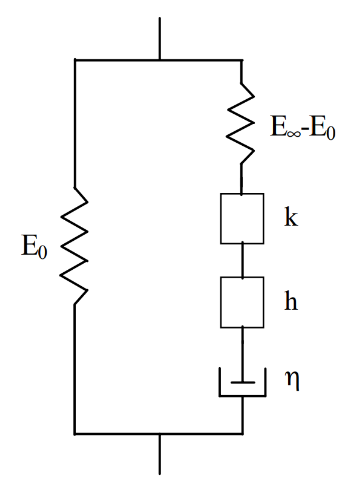

Figure 2.10 Element Configuration of 2S2P1D.

diffusion. The rates of these processes depend on molecular motion, which is inherently temperature dependent. If every process that contributes to the material's viscoelastic response accelerates uniformly with an increase in temperature, then the relaxation function can be reformulated as:

$$E(t,T) = E(\zeta,T_0) \quad \text{(Eq. 2.42)}$$

where the reduced time ζ is defined by

$$\zeta = \frac{\mathrm{t}}{\mathrm{a_T}(\mathrm{T})}. \quad \text{(Eq. 2.43)}$$

In this expression, T_0 is a chosen reference temperature, and $a_T(T)$ is the shift factor that accounts for the temperature dependence of the viscoelastic response. Essentially, a change in temperature effectively stretches or compresses the time scale over which viscoelastic phenomena occur. Since viscoelastic properties are frequently visualized as a function of time, log(t) or frequency, log(ω), a temperature change leads to a horizontal shift of these curves along the time or frequency axis. Materials that exhibit this behavior, as described by the relationship are said to obey the time–temperature superposition principle and are known as thermo-rheologically simple materials (Schwarzl & Staverman, 1952).

The shift factor $\alpha_T(T)$ is influenced by both temperature and material properties. For many materials, temperature-dependent creep behavior follows the Arrhenius equation:

$$\tau^{-1} = \nu_0 \exp\left\{-\frac{U}{kT}\right\}, \quad \text{(Eq. 2.44)}$$

where τ represents the time constant, ν denotes the frequency-dependent characteristic, T is the absolute temperature, K is the Boltzmann constant, and U is the activation energy. This formulation leads to thermo-rheologically simple behavior, characterized by the shift factor:

$$\ln a_T = \frac{U}{k}\left\{\frac{1}{T_2} - \frac{1}{T_1}\right\}. \quad \text{(Eq. 2.45)}$$

2.8 Master Curve

Estimating the horizontal shift of a master curve at different temperatures without experimental data presents a significant challenge. To address this, two widely recognized shift functions are utilized: the Williams-Landel-Ferry (WLF) equation and the Arrhenius activation energy model (Hajikarimi & Nejad, 2021). For asphalt materials, the time-temperature shift behavior is predominantly described by the empirical WLF equation as shown in Equation 2.46.

$$\log a_T = -\frac{C_1(T - T_{\mathrm{ref}})}{C_2 + (T - T_{\mathrm{ref}})}, \quad \text{(Eq. 2.46)}$$

In this equation, T_{ref} represents the reference temperature, and the logarithm is base 10. For polymers near the glass transition temperature (T_g), the shift factor $a_T(T)$ exhibits significant sensitivity to temperature variations, making an isothermal approximation unreliable under even minor fluctuations. The constants C_1 and C_2 are material-specific parameters. Considering time or frequency as the primary variable, the shift factor can be defined as follows:

$$\alpha_t = \frac{t}{t_R} \quad \text{(Eq. 2.47)}$$

where t represents the actual experimental time and t_R denotes the reduced time in the master curve. Additionally, the shift factor can be expressed in the frequency domain as:

$$\alpha_t = \frac{\omega_R}{\omega} \quad \text{(Eq. 2.48)}$$

where ω_R denotes the reduced frequency and ω corresponds to the experimentally observed frequency. By applying a shift function like WLF, the desired viscoelastic properties can be determined at any temperature or loading frequency.

The Arrhenius activation energy equation (Menzinger & Wolfgang, 1969) can be used to derive a shift function for temperatures below the T_g:

$$\tau(T) = A\exp\left(-\frac{E_a}{RT}\right) \quad \text{(Eq. 2.49)}$$

In this equation, τ denotes the relaxation time, T is temperature, E_a represents the activation energy, and R is the gas constant. Applying the natural algorithm (ln) of both sides results in the equation:

$$\ln\left[\tau(T)\right] = \ln(A) - \frac{E_a}{RT}. \quad \text{(Eq. 2.50)}$$

Next, by forming a ratio between an arbitrary temperature and T_g and then converting the result to base-ten logarithms, the following expression is obtained:

$$\log(a_T) = \log\left(\frac{\tau(T)}{\tau(T_g)}\right) = -\frac{E_a}{2.303R}\left(\frac{1}{T} - \frac{1}{T_g}\right). \quad \text{(Eq. 2.51)}$$

2.9 Layered Elastic Anisotropic Model

This section presents the derivation of stresses and deformations in a multilayered, transversely isotropic elastic half-space subject to uniformly distributed vertical loads on a circular surface area. In the Cartesian coordinate system (x,y,z) where x-y denotes the plane of material isotropy, the relevant constitutive relationship is:

$$\varepsilon_x = a_{11}\sigma_x + a_{12}\sigma_y + a_{13}\sigma_z \quad \text{(Eq. 2.52)}$$

$$\varepsilon_y = a_{12}\sigma_x + a_{11}\sigma_y + a_{13}\sigma_z \quad \text{(Eq. 2.53)}$$

$$\varepsilon_z = a_{13}\sigma_x + a_{13}\sigma_y + a_{33}\sigma_z \quad \text{(Eq. 2.54)}$$

$$\varepsilon_{xz} = \frac{a_{44}}{2}\tau_{xy} \quad \text{(Eq. 2.55)}$$

$$\varepsilon_{xz} = \frac{a_{44}}{2}\tau_{xz} \quad \text{(Eq. 2.56)}$$

$$\varepsilon_{yz} = a_{66}\tau_{yz} \quad \text{(Eq. 2.57)}$$

Here, the six ε terms represent the strain tensor components, whereas the σ and τ terms denote the stress tensor components, and the α terms correspond to the material constants (i.e., elastic properties). Using a cylindrical coordinate system (r,θ,z), as shown in Figure 2.11, with z taken as the axis of material symmetry, and assuming an axisymmetric deformation state (i.e., εθz=εrθ=0), the constitutive relationship can be expressed as:

$$\varepsilon_r = a_{11}\cdot\sigma_r + a_{12}\cdot\sigma_\theta + a_{13}\cdot\sigma_z \quad \text{(Eq. 2.58)}$$

$$\varepsilon_\theta = a_{12}\cdot\sigma_r + a_{11}\cdot\sigma_\theta + a_{13}\cdot\sigma_z \quad \text{(Eq. 2.59)}$$

$$\varepsilon_z = a_{13}\cdot\sigma_r + a_{13}\cdot\sigma_\theta + a_{33}\cdot\sigma_z \quad \text{(Eq. 2.60)}$$

$$\varepsilon_{rz} = \left(\frac{a_{44}}{2}\right)\cdot\tau_{rz} \quad \text{(Eq. 2.61)}$$

in which,

$$a_{11} = \frac{1}{E_x}, \quad a_{33} = \frac{1}{E_z}, \quad a_{12} = -\frac{\nu_{xy}}{E_x}, \quad a_{13} = -\frac{\nu_{xz}}{E_z}, \quad a_{44} = \frac{1}{G_{xz}}.$$

Here, the included elastic constants are two Young's moduli: $E_X(=E_y)$ and E_Z, two Poisson's ratios: $\nu_{xy}\left(=\nu_{yx}\right)$ $and\,\nu_{xz}\left(=\nu_{zx}.E_z / E_x\right)$, and one shear modulus G_{xz} (=G_{yz}).

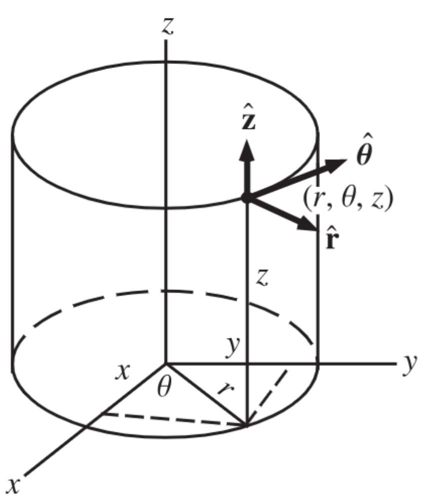

Figure 2.11 A Cylindrical Coordinate System.

To ensure that the strain energy remains positive, it is necessary to impose the following property restrictions (PR) on the elastic constants:

$$\mathrm{E_x, E_z, G_{xz}} > 0 \;(\mathrm{PR1});$$

$$1 - \nu_{xy}\cdot 2\cdot\nu_{xz}\cdot\nu_{zx} > 0 \quad (\mathrm{PR2});$$

$$1 - \left|\nu_{xy}\right| > 0 \quad (\mathrm{PR3})$$

The stresses ($\sigma_r, \sigma_\theta, \sigma_z, \tau_{rz}$) and the displacements (u, w) in the radial (r) and axial (z) directions, respectively, can be obtained from a stress function $\phi(r,z)$, as detailed in Lekhnit͡skiĭ (1963) and Singh (1986):

$$\sigma_r = -\frac{\partial}{\partial z}\left(\frac{\partial^2\phi}{\partial r^2} + \frac{b}{r}\frac{\partial\phi}{\partial r} + a\cdot\frac{\partial^2\phi}{\partial z^2}\right) \quad \text{(Eq. 2.62)}$$

$$\sigma_\theta = -\frac{\partial}{\partial z}\left(b\cdot\frac{\partial^2\phi}{\partial r^2} + \frac{1}{r}\frac{\partial\phi}{\partial r} + a\cdot\frac{\partial^2\phi}{\partial z^2}\right) \quad \text{(Eq. 2.63)}$$

$$\sigma_z = -\frac{\partial}{\partial z}\left(c\cdot\frac{\partial^2\phi}{\partial r^2} + \frac{c}{r}\frac{\partial\phi}{\partial r} + d\cdot\frac{\partial^2\phi}{\partial z^2}\right) \quad \text{(Eq. 2.64)}$$

$$\tau_{rz} = \frac{\partial}{\partial r}\left(\frac{\partial^2\phi}{\partial r^2} + \frac{1}{r}\frac{\partial\phi}{\partial r} + a\cdot\frac{\partial^2\phi}{\partial z^2}\right) \quad \text{(Eq. 2.65)}$$

$$u = \left(a_{12} - a_{11}\right)\cdot\left(1 - b\right)\cdot\frac{\partial^2\phi}{\partial r\partial z} \quad \text{(Eq. 2.66)}$$

$$w = \left(2\cdot a_{13}\cdot a - a_{33}\cdot d\right)\cdot\frac{\partial^2\phi}{\partial z^2} - a_{44}\left(\frac{\partial^2\phi}{\partial r^2} + \frac{1}{r}\frac{\partial\phi}{\partial r}\right) \quad \text{(Eq. 2.67)}$$

In all above equations, the a , b , c, and d parameters represent elastic constant functions, which are determined as follows:

$$a = \frac{a_{13}\cdot\left(a_{11} - a_{12}\right)}{a_{11}\cdot a_{33} - a_{13}^2} \quad \text{(Eq. 2.68)}$$

$$b = \frac{a_{13}\cdot\left(a_{13} + a_{44}\right) - a_{12}\cdot a_{33}}{a_{11}\cdot a_{33} - a_{13}^2} \quad \text{(Eq. 2.69)}$$

$$c = \frac{a_{13}\cdot\left(a_{11} - a_{12}\right) + a_{11}\cdot a_{44}}{a_{11}\cdot a_{33} - a_{13}^2} \quad \text{(Eq. 2.70)}$$

$$d = \frac{a_{11}^2 - a_{12}^2}{a_{11}\cdot a_{33} - a_{13}^2} \quad \text{(Eq. 2.71)}$$

The stress function at any point with radial r, and axial z depth should satisfy the following “compatibility” condition:

$$\nabla_{\alpha}^{2}\nabla_{\beta}^{2}\phi = 0,$$

in which,

$$\nabla_{\alpha}^{2} = \frac{\partial^{2}}{\partial r^{2}} + r^{-1}\frac{\partial}{\partial r} + \alpha^{-2}\cdot\frac{\partial^{2}}{\partial z^{2}},$$

&

$$\left(\nabla_{\beta}^{2} = \nabla_{\alpha}^{2}\right)$$

The terms α and β are also determined based on the material properties using Equation 2.72.

$$\frac{\alpha^{2}}{\beta^{2}} = \frac{a + c \pm \sqrt{\left(a+c\right)^{2} - 4\cdot d}}{2\cdot d} \qquad \text{(Eq. 2.72)}$$

If a semi-infinite domain consists of n-1 parallel layers placed on top of a half-space, each layer can be labeled by a subscript, *i*, with its material characteristics given as $(E_z)_i$, $(E_x)_i$, $(\nu_{zx})_i$, $(\nu_{xy})_i$, and $(G_{xz})_i$. Layers are labeled consecutively, beginning with Layer 1 at the top and Layer n as the half-space. Consistent with the isotropic case (Section 4.2.1), the origin of the cylindrical coordinate system lies at the surface of the first layer, with the z-axis directed downward and r-axis aligned parallel to the layer interfaces. The individual interface depths (measured from the surface) are represented by z_i (where i=1, 2, …., n-1). Therefore, z_1 is the thickness of Layer 1, z_2 is the combined thickness of layer 1 and 2, and so on. Denoting the total thickness of the *n*-1 layers by *H*, ($H=z_{n-1}$), a stress function satisfying these conditions can be formulated as follows:

$$\varnothing_i\left(\rho,\lambda\right) = \left(\frac{H^{3}.J_{0}\left(m.\rho\right)}{m^{2}}\right)\cdot\left(\begin{array}{l} A_i.e^{-m.(\lambda_i-\lambda)} - B_i.e^{-m.\left(\lambda-\lambda_{i-1}\right)} \\ +C_i.m.\lambda.e^{-m.(\lambda_i-\lambda)} - D_i.m.\lambda.e^{-m.(\lambda-\lambda_{i-1})} \end{array}\right) \qquad \text{(Eq. 2.73)}$$

in which, $\rho = r/H$, $\lambda = z/H$, $\lambda_i = z_i/H$, where m is a dimensionless parameter. The terms A_i, B_i, C_i, and D_i are dimensionless functions of m, J_k denotes the Bessel function of the first kind of order k, and the subscript *i* indicates the layer index. Substituting this function into Equations 2.62–2.67 yields the layer *i* response under the nondimensional surface load.

To determine the value of each dimensionless functions, it is necessary to solve a system of linear equations representing boundary and continuity conditions. For the bottom most layer (i=n), as $\lambda \to \infty$, both the stresses and displacements must vanish. The stress function must be determined in a way to ensure that it complies with the elastic properties of each layer and satisfies the overall equilibrium and compatibility conditions throughout the multilayered system.

2.10 Mechanistic Model Development

The development of a mechanistic-based methodology produces a dynamic modulus master curve by integrating a pavement’s structural configuration with time-dependent data from FWD testing. The approach begins by defining a cylindrical element at multiple depths within the pavement, as shown in Figure 2.12. This cylindrical element enables the localized evaluation of stress-strain states under FWD loading. Substituting Equation 2.73 into Equations 2.62–2.67 yields layer-specific stress and strain profiles under a nondimensional surface load. Four dimensionless functions, each dependent on the parameter *m*, are determined by satisfying boundary conditions (i.e., layer interfaces) and continuity constraints (i.e., stress and displacement compatibility) between layers. This ensures that the stress function not only aligns with each layer’s anisotropic or isotropic elastic properties but also maintains overall system equilibrium.

The complete derivation was coded in MATLAB, providing a systematic means to compute the stress–strain tensors at any point of interest (POI), including interfacial boundaries, within the pavement. By accommodating the pavement’s thickness, subgrade modulus, and Poisson’s ratios, the program can independently solve for elastic modulus. In other words, for each POI, the resulting model parameters (i.e., dynamic modulus, strain response) are derived directly from the FWD measurements and the known pavement layer properties. Figure 2.12 shows the designated POIs in the pavement’s multilayer system, each located at the layer interfaces beneath the geophone sensors. These positions are selected to consider well-defined boundary conditions and to accurately obtain the structural response.

To determine the elastic modulus of each layer, the model relies on peak deflection points, reflecting the elastic theory principle of utilizing maximum deflections for each geophone. To consider the viscoelastic nature of flexible pavement, the corresponding principles (CP) in viscoelasticity is applied to make the model account for the time- and frequency-dependent nature of asphalt materials (Section 2.4). This allows the model to extend classical elastic solutions into the viscoelastic domain, incorporating the effects of material relaxation and delayed response under loading. To this end, a discrete time-series analysis was performed, consisting of the following key steps:

- Decomposing the load signal into multiple everlasting sinusoids, representing the harmonic components of the applied load;
- Determining the corresponding deflection as a sinusoid at the same loading time; and
- Summing all sinusoidal deflections to reconstruct the total deflection, providing a viscoelastic response to the load signal.

Unlike conventional methods, this approach analyzes the time-domain response through Differential-Time Fourier Transform (DTFT) analysis. This enables the determination of an equivalent loading duration at any given instant within the deflection time history. The applied load and its corresponding deflections at each geophone are decomposed into differential time segments, facilitating a high-resolution mechanistic evaluation of pavement response, as illustrated in Figure 2.13. As this

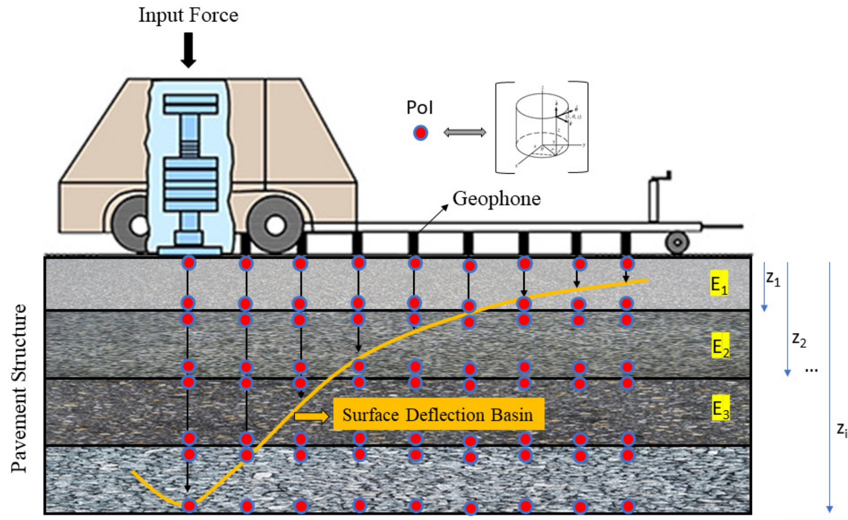

Figure 2.12 FWD Configuration and Point of Interests for a Pavement Structure.

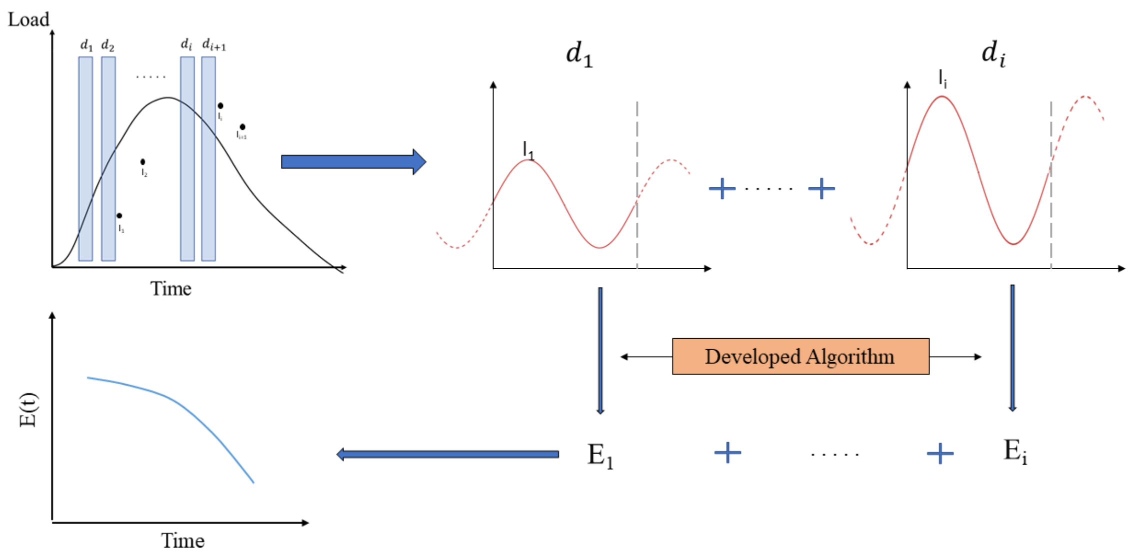

Figure 2.13 Differential-Time Fourier Transform Analysis for Determining Relaxation Modulus.

figure shows, the results of the mechanistic algorithm for each loading time yields a corresponded relaxation modulus ($E(t)$).

The outcome of this approach is a relaxation modulus curve, $E(t)$, which characterizes the time-dependent stiffness of the asphalt material. To transition from the time-domain to the frequency-domain, the relaxation modulus is transformed using the Laplace transform function (Section 2.5). This transformation facilitates the analysis of viscoelastic behavior in the loading frequency domain, enabling a frequency-dependent representation of asphalt materials. It should be noted that the E(t) is obtained within a very narrow time domain. However, due to the inherent limitations of FWD testing, including its restricted loading frequency range and the test temperatures, direct determination of E^* over an extended frequency spectrum is not feasible. To address this limitation, a fractional-order differential model (Section 2.6.2) is used to construct the E^* master curve.

3. DATA COLLECTION

In this study, the E^* master curve was determined through both backcalculation techniques from FWD time history data and laboratory dynamic modulus tests conducted on field-cored specimens. A set of flexible pavement sections was selected for FWD testing, with field-core sampling from the exact location where the FWD loading was applied. These core specimens were then transported to the laboratory, where dynamic modulus tests were conducted to obtain the actual master curve under controlled conditions.

3.1 FWD Testing

Several full-depth asphalt pavements were selected for FWD testing as summarized in Table 3.1.

Figure 3.1 shows the deflection time history data for all geophones from FWD testing conducted on the State Road (SR) 67 section, as well as the related appearance of the pavement surface. The data indicates that the maximum deflection is recorded at the center geophone (D1), followed by progressively lower deflections at the subsequent geophones. As the distance from the load center increases, the deflection magnitude decreases, demonstrating the typical distribution of pavement response under FWD loading.

TABLE 3.1
Selected Pavement Section Information for FWD and Lab Testing.

Section	Mean Pavement Surface Temperature (°F)	Pavement Layer Thickness (in.)		Estimated Subgrade Modulus (ksi)
US 27	90 and 105	Surface	1.5	15.0
		Intermediate	2.5	
		Base	11.0	
SR 67	95	Surface	1.5	15.0
		Intermediate	3.0	
		Base	11.5	
SR 545	118 and 95	Surface	1.5	13.0
		Intermediate	2.5	
		Base	11.5	
SR 32	95 and 137	Surface	1.5	13.0
		Intermediate	2.5	
		Base	12	
US 20	95 and 85	Surface	2.0	18.0
		Intermediate	2.5	
		Base	11	
US 31	78	Surface	1.8	14.0
		Intermediate	2.5	
		Base	10.5	
I-69	62	Surface	2.0	12.0
		Intermediate	3.0	
		Base	10.0	

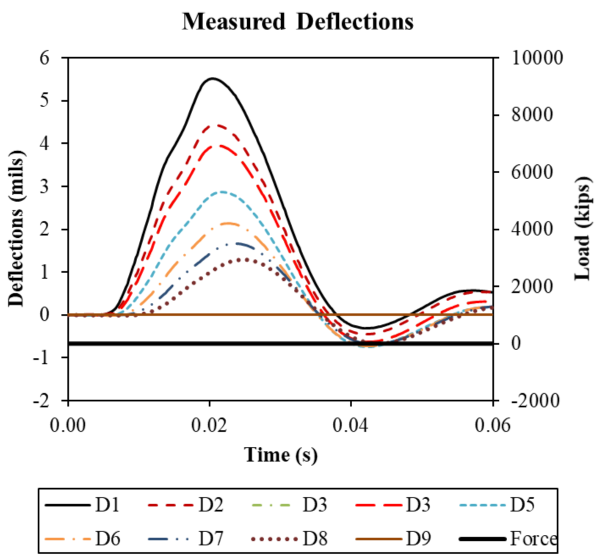

(a)

(b)

Figure 3.1 (a) FWD Time History Data for SR 67 and (b) SR 67 Appearance Before FWD Testing.

After FWD testing, field-core specimens were extracted through a drilling process at the exact locations where the FWD tests were conducted, as shown in Figure 3.2.

3.2 Dynamic Modulus Testing

Dynamic modulus testing was performed on field-cored specimens following the American Association of State Highway and Transportation Officials (AASHTO) test method, TP-132, "Standard Method of Test for Determining the Dynamic Modulus for Asphalt Mixtures Using Small Specimens in the Asphalt Mixture Performance Tester (AMPT)." The test was conducted at three test temperatures of 39, 68, and 104°F (equivalent to 4, 20, and 40°C, respectively) and six frequencies (25, 10, 5, 1, 0.5, and 0.1 Hz). The displacements were measured after applying a series of cyclic sinusoidal loads using three magnetic extensometers. It should be noted that all specimens were conditioned at the test temperature for 4 hr before performing the test. These results were subsequently used to construct the E^* master curve at a 68°F (20°C) reference temperature using the FlexMAT software. Figure 3.3 provides an

(a) (b)

Figure 3.2 (a) FWD Testing and (b) Field-Core Sampling (I-69 Test Section).

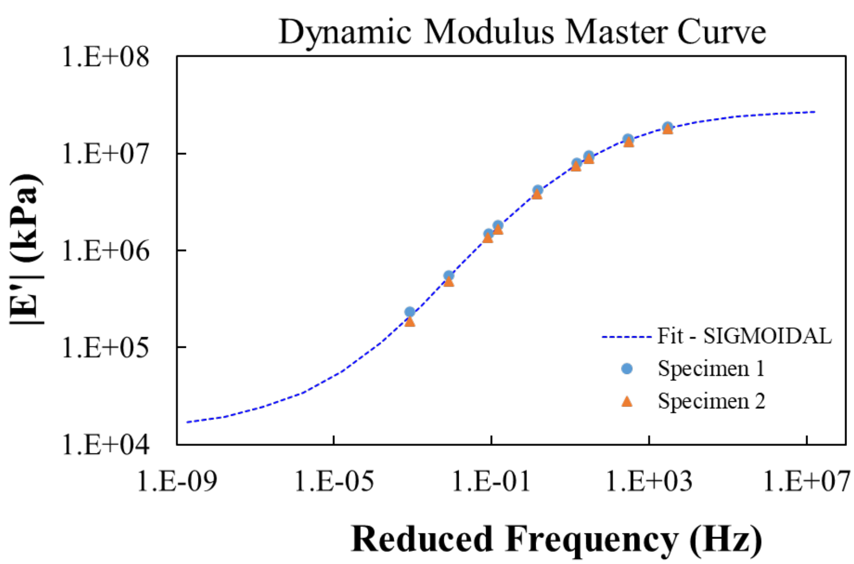

Figure 3.3 E^* Master Curve Constructed by FlexMAT From Dynamic Modulus Test Results Performed at Three Test Temperatures.

example of an E^* master curve constructed by FlexMAT for the US 31 surface layer, derived from dynamic modulus testing on field-cored specimens.

3.3 Methodology

The E^* master curve was backcalculated using both the mechanistic approach developed in the research and ViscoWave, a commercially available software package. The results from these methods were then compared and further validated against the laboratory-measured E^* master curve determined by FlexMAT.

3.3.1 Mechanistic Analysis

The mechanistic method, detailed in Section 2.10, was used to generate the E^* master curve based on the collected FWD data. A parametric study was performed to optimize the method's computational time by focusing on the selection of time interval steps. Time intervals of 3, 5, 10, 15, and 20 were evaluated to find a balance between computational effort and the precision of the results that reliably represent a pavement's material characteristics.

A sensitivity analysis was also performed to assess the sensitivity of the backcalculation process to pavement configuration parameters, such as layer thickness and Poisson's ratio (ν). In this assessment, a slight variation was introduced to the pavement layers' thicknesses to evaluate its impact on the resulting master curve. For instance, increasing the surface layer thickness by 0.5 in. was used to observe how the dynamic modulus would shift for all layers (surface, intermediate, and base). This analysis is performed to determine the relative importance of each input parameter. Finally, the mechanistic model was used to produce the E^* master curve for all the flexible pavement sections tested.

3.3.2 ViscoWave Analysis

ViscoWave was developed to determine the E^* master curve of pavement materials using FWD time history data (Lee, 2014). By incorporating pavement structural details, such as layer thickness, Poisson's ratio, and density, this software can estimate both the relaxation and dynamic moduli using the FWD time-history data. The results of this tool were compared with those obtained by the mechanistic model and the laboratory dynamic modulus tests.

4. VISCOWAVE

ViscoWave is a dynamic finite element method software package designed to estimate the dynamic modulus of flexible pavement layers by integrating wave propagation theory with a forward analysis approach (Lee, 2014). Lee (2013) stated that the main framework of this tool is the use of continuous integral transforms, such as Laplace and Hankel transforms. These transform functions are more compatible with the transient, nonperiodic nature of FWD data than the Discrete Fourier Transform (DFT) that is used in conventional approaches. This approach eliminates many challenges associated with discrete transforms, including signal truncation, periodicity assumptions, and noise sensitivity. Moreover, this software uses optimization algorithms, such as Gauss-Newton and Levenberg-Marquardt methods, to determine the dynamic modulus within the seed values defined initially as input in the software. Like the Pavement ME, ViscoWave uses the sigmoidal function, Equation 4.1, to represent the E^* master curve.

$$\log\left(\left|E^*\right|\right) = \delta + \frac{\alpha}{1 + e^{\beta - \gamma \log(\xi)}} \qquad \text{(Eq. 4.1)}$$

where α, β, γ, and δ are the sigmoidal fitting coefficients determined through an optimization process. Figure 4.1 shows an example of the ViscoWave results. The fitted curve can be derived either from the sigmoidal function or the Prony series. ViscoWave determines the four aforementioned coefficients, which control the shape of the curve, through optimization algorithms based on a forward analysis method. Inputs to this software include pavement structural parameters (i.e., the modulus of elasticity for nonasphalt layers, Poisson's ratios, density, thickness, and damping ratio), along with FWD time-history data and seed values to establish the maximum and minimum dynamic modulus over the operational frequency range of the FWD.

To assess the ViscoWave accuracy, multiple flexible pavement sections, including SR 67 and SR 27, were selected for analysis by performing FWD tests, then extracting field cores from the exact were the FWD testing was performed. These cores were then tested in the laboratory to determine the master curves for the various asphalt materials. Table 4.1 provides information on the selected pavement sections.

The outcome of the ViscoWave tool is the value of sigmoidal function coefficients that can be used to generate E^* master curves for the various pavement layers. Figure 4.2 presents the D0 and D18 deflection data, demonstrating a strong match between the modeled and observed deflection responses.

Table 4.2 shows the four sigmoidal function coefficients determined by ViscoWave for the three asphalt mixture layers of US 27. By substituting these coefficients into the sigmoidal function (Equation 4.1), the E^* curve can be drawn for each of the pavement layers, as shown in Figure 4.3. As shown in the figure, the ViscoWave analysis results are compared to laboratory-based dynamic modulus measurements performed on the field cores. The plots show a noticeable discrepancy between the ViscoWave results and the dynamic modulus test results. For each asphalt mixture layer, the master curve derived through ViscoWave differs in shape from that obtained via dynamic modulus testing, especially for the intermediate and base layers. This inconsistency may be attributed, at least in part, to the curve-fitting procedure.

Data from SR 67 was also used to compare the ViscoWave analysis results to laboratory dynamic modulus. Table 4.3 presents the final ViscoWave results for the SR 67 section, while Figure 4.4 show the E^* master curves for the three layers. Similar to the US 27 comparison, the ViscoWave-derived master curve diverges from the dynamic modulus testing results.

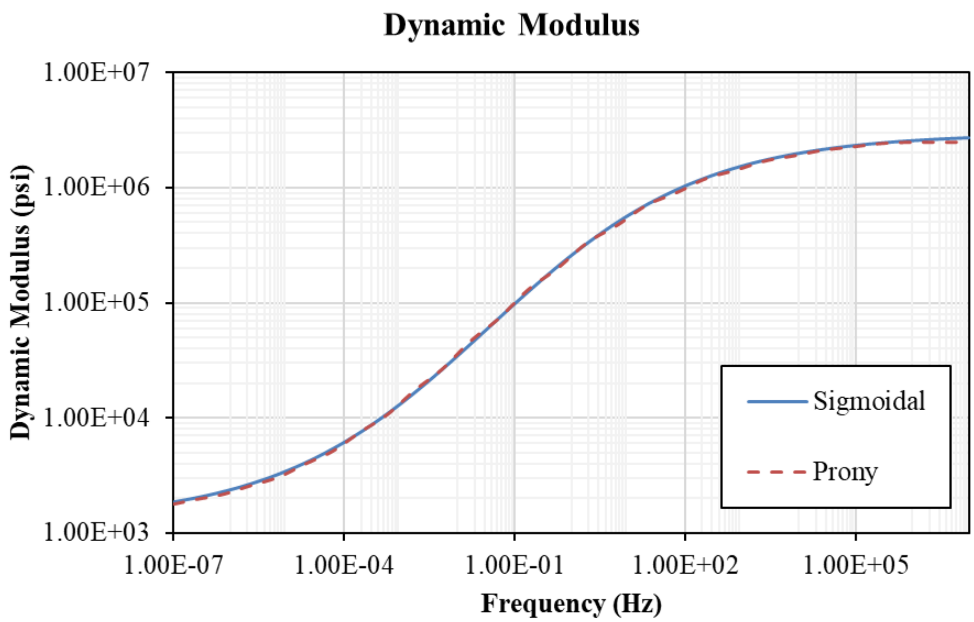

Figure 4.1 ViscoWave Results Based on FWD Time History Data.

TABLE 4.1
Selected Road Section for ViscoWave Analysis.

Item		SR 67	US 27
Thickness (in.)	Layer 1	1.5	1.5
	Layer 2	3.0	2.5
	Layer 3	11.5	11.0
Subgrade Modulus (ksi)		15.0	15.0
Mean Surface Temperature (°F)		95.0	114.0

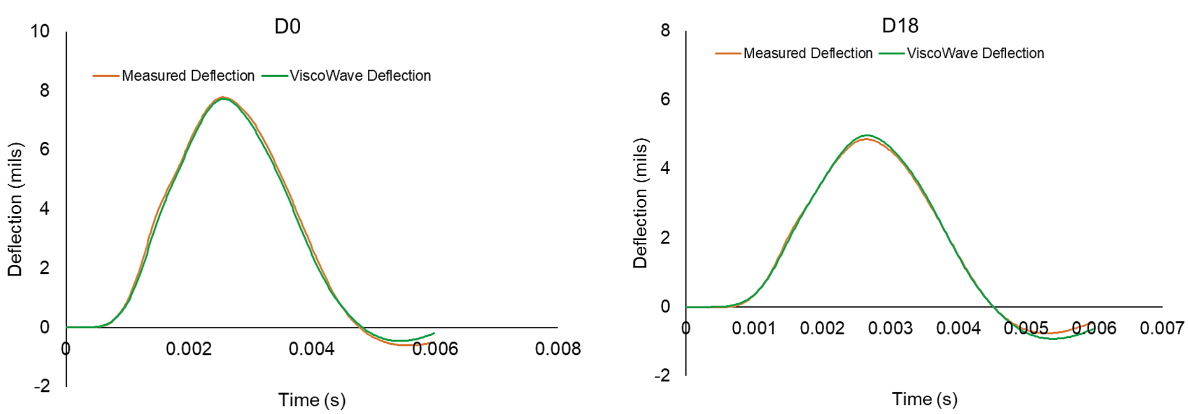

(a) (b)

Figure 4.2 ViscoWave Time History Data for Two FWD Geophones (a) Geophone D0 and (b) Geophone D18.

TABLE 4.2
ViscoWave Analysis Results for US 27.

Layer Number	C1	C2	C3	C4
1	3.123	3.446	–0.128	0.554
2	3.000	3.200	–0.130	0.754
3	3.200	2.800	–0.150	0.658

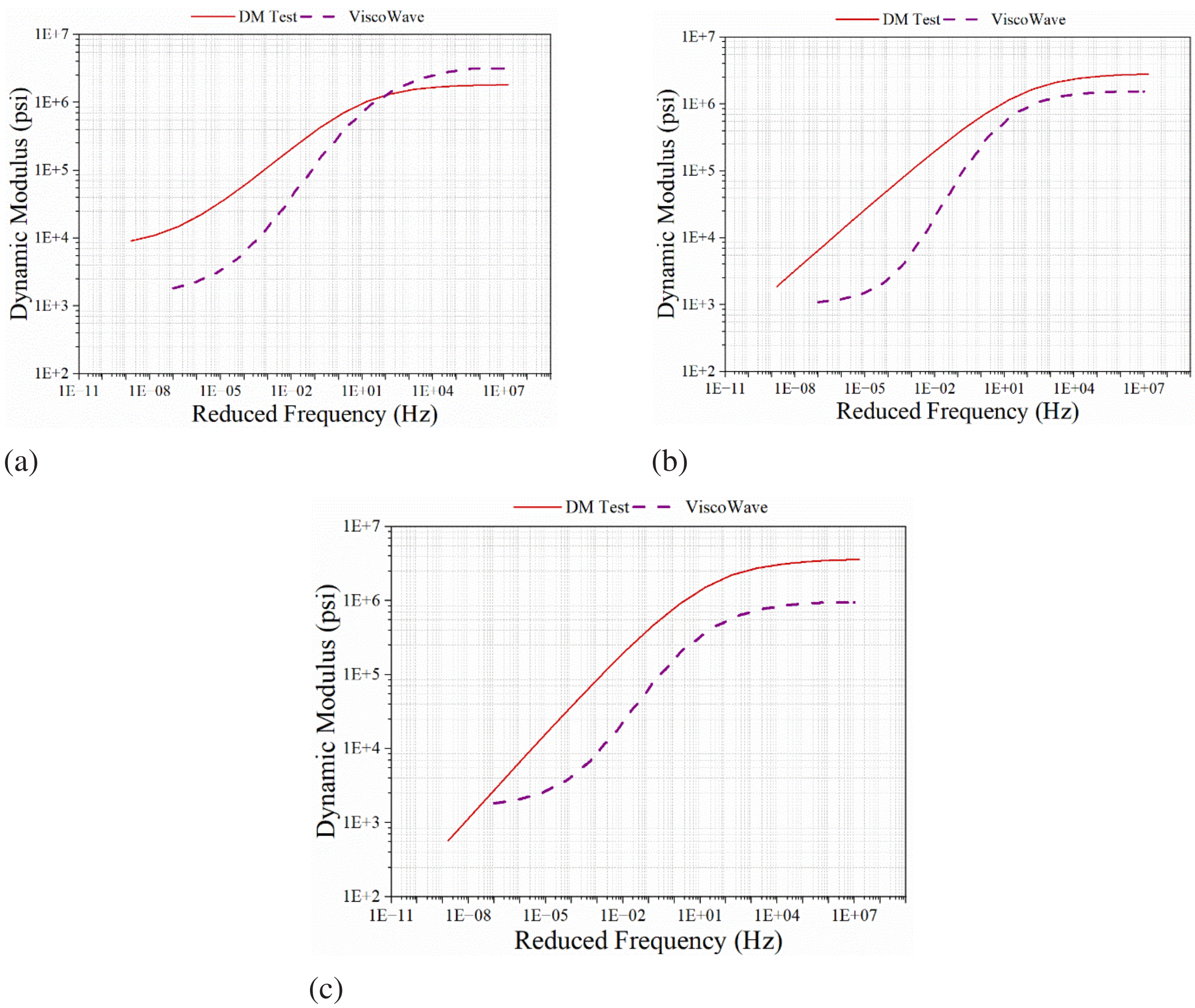

Figure 4.3 ViscoWave and Field Core Dynamic Modulus Tests Results for US 27 (a) Surface Layer; (b) Intermediate Layer; (c) Base Layer.

TABLE 4.3
ViscoWave Analysis Results for SR 67.

Layer Number	C1	C2	C3	C4
1	3.572	3.410	–0.118	0.509
2	2.771	3.194	–0.137	0.803
3	2.799	3.182	–0.141	0.800

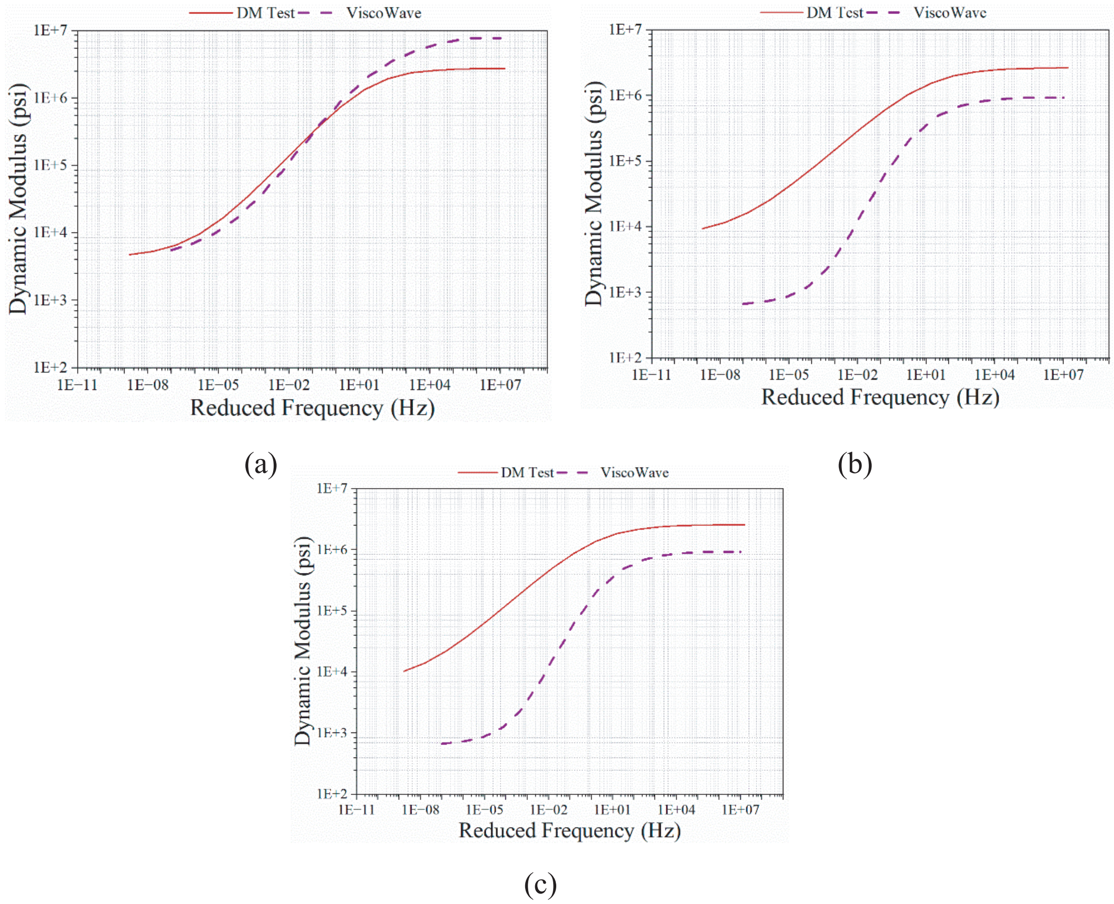

Figure 4.4 ViscoWave and Lab Testing Results for SR 67 Road Section (a) Surface Layer; (b) Intermediate Layer; (c) Base Layer.

For the surface layer, ViscoWave overestimates *E** compared to the experimental curve at higher frequency, whereas for the intermediate and base layers, it underestimates E* over the entire loading-frequency range.

To better understand the ViscoWave analyses, a parametric study on the sigmoidal function was conducted to evaluate how each coefficient influences the generated *E** master curve.

4.1 C_1 Analysis

With a 0.5 increase in the C_1 parameter while keeping the other three coefficients constant, the *E** value increases by 215% at all loading frequencies, as shown in Figure 4.5. This result is expected, as C_1 is responsible for the vertical shift in the sigmoidal function that influences the overall magnitude of *E** over all loading frequencies. Since C_1 is an offset term in the sigmoidal equation, it causes a uniform vertical shift in the modulus curve without affecting the shape or rate of modulus transition between low and high frequencies. This suggests that C_1 should be associated with factors that contribute to a general stiffness increase but do not interfere with the material's viscoelastic behavior. Such factors can be related to aggregate properties, including aggregate source, mineral composition, or gradation, rather than temperature- or frequency-dependent viscoelastic characteristics of asphalt binder.

4.2 C_2 Analysis

With a 0.5 increase in the C_2 parameter and the other three parameters unchanged, the effect on the *E** values vary over all frequency ranges. As indicated in Figure 4.6, the effect of C_2 is negligible at low frequencies but rises steadily to 200% at higher frequencies. At shorter frequencies (long loading times or higher temperatures), the distortion of the *E** master curve caused by C_2 is relatively small. However, as frequency increases (short loading times or low temperatures), the effect of C_2 is more pronounced. This reaction shows that C_2 is primarily associated with the viscoelastic properties of the asphalt binder, mainly at low temperatures, where the rheological response of the asphalt binder controls the overall pavement response.

Unlike C_1, which causes a uniform vertical shift in the modulus curve, C_2 primarily influences the model's behavior at higher

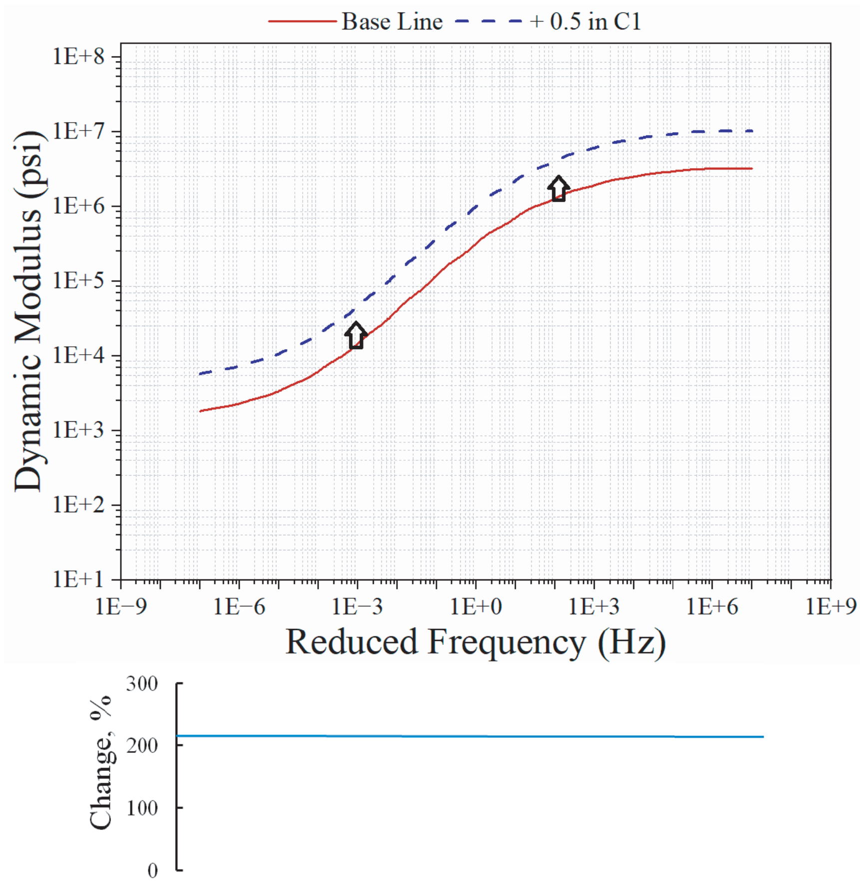

Figure 4.5 C_1 Effect on Sigmoidal Function.

loading frequencies. This indicates that C_2 controls the material's rate of stiffening at increasing frequencies, which aligns with the temperature-dependent behavior of asphalt binders. Asphalt binder exhibits more elastic characteristics in colder conditions, leading to a significant increase in modulus, which the C_2 parameter can describe.

4.3 C_3 Analysis

As C_3 parameter decreases by 0.1 the other three parameters kept constant, there is an increase in the *E** value in the intermediate frequency range, as shown in Figure 4.7. The effect is most noticeable around 0.1 Hz, increasing the modulus by as much as 150%. This behavior suggests that C_3 is responsible for the transition area of the sigmoidal function, where the material undergoes a transition from a response dominated by viscous behavior at low frequencies to one dominated by elastic behavior at high frequencies. Since C_3 primarily affects the intermediate frequency range, it should likely be considered in the control of the transition rate between the viscous and elastic state, i.e., filler-binder interactions.

4.4 C_4 Analysis

A 0.5 increase in the C_4 parameter, keeping the other three parameters constant, significantly affects the shape of the *E** master curve. As shown in Figure 4.8, this change reduces the *E** value in the low-frequency range, reducing stiffness at long loading times (or high temperatures). In contrast, the modulus values are shifted upwards at higher frequencies, which reflects an increase in stiffness at short loading times (or low temperatures). This observation suggests that C_4 plays a significant role in determining the transition region between the viscous-dominated and elastic-dominated response of the asphalt materials. C_4 is, therefore, one of the controlling parameters in the master curve shape in the sigmoidal function.

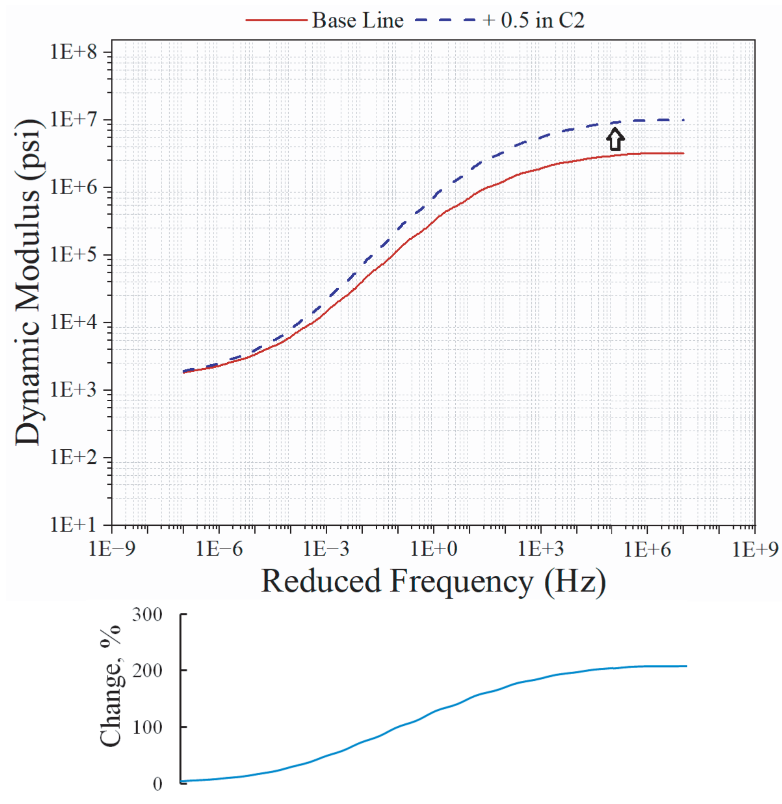

Figure 4.6 C_2 Variation Effect on the Sigmoidal Function Shape.

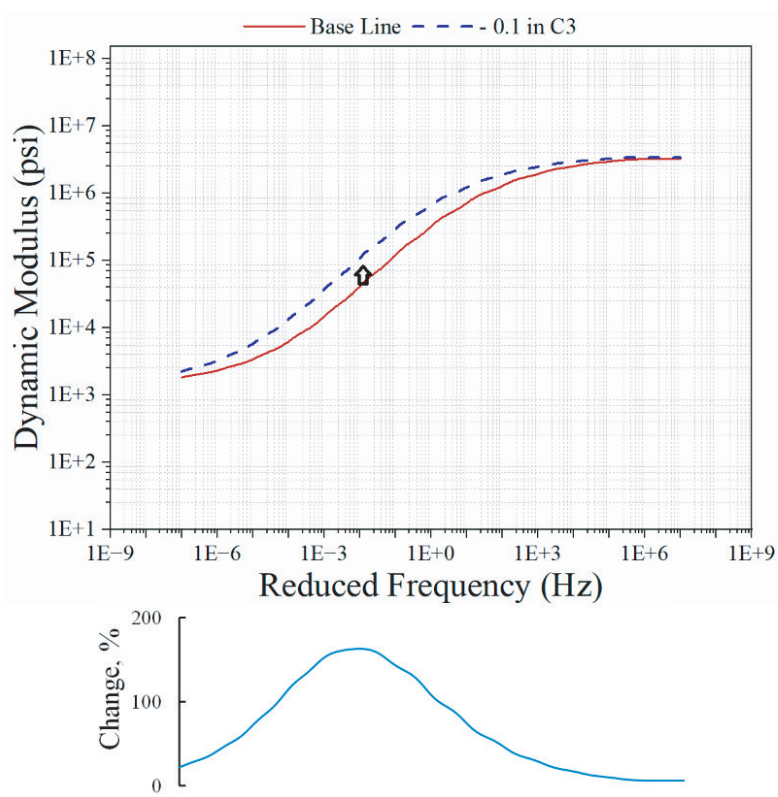

Figure 4.7 C_3 Variation Effect on the Sigmoidal Function Shape.

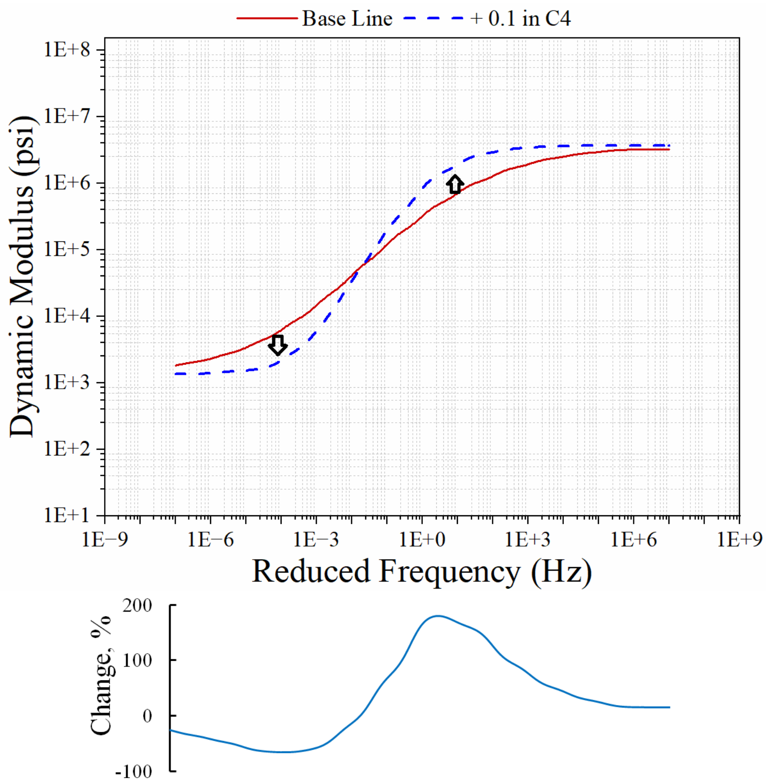

Figure 4.8 C_4 Analysis Under +0.5 Increment.

5. PAVEMENT ME SOFTWARE

The Pavement ME software uses the MEPDG hierarchical input levels analysis to describe the importance of the E^* master curve backcalculation. A key feature of the MEPDG is its hierarchical input system, which allows users to select design parameters based on project needs and budgetary limitations. The hierarchical input refers to traffic and material properties data in the analyses of new flexible pavements and the assessment of existing ones. The MEPDG presents three different input levels that allow designers to include different levels of detail to fit a project's specific demands.

5.1 MEPDG Hierarchical Input Levels

The MEPDG categorizes inputs into three hierarchical levels based on the level of detail and accuracy required, as follows:

- **Level 1** offers the highest precision and the lowest risk of error by using data directly measured in laboratories or on-site. Although this approach provides the most accurate reflection of specific traffic, material, and climatic conditions, it also carries the highest costs in terms of testing and data collection and can be time consuming.
- **Level 2** represents an intermediate level of accuracy. Here, parameters are derived from established correlations, typically using results from routine laboratory tests or information drawn from an agency's existing databases.
- **Level 3** mainly depends on default values, making it the least accurate approach. In this tier, best estimates are used to represent the input parameters, thus minimizing costs and data-gathering efforts but reducing overall precision in the design process.

For HMA characterization at Level 1, the MEPDG requires conducting dynamic modulus tests at multiple loading frequencies and temperatures. The software uses these results to develop an E^* master curve that provides insights into the pavement mechanical performance at different temperatures or loading conditions. In Levels 2 and 3, E^* testing is not required, as the software includes built-in predictive models to determine E^* values under different conditions. Examples of required MEPDG input at all three levels is shown in Figure 5.1.

As shown in Figure 5.1, Level 1 requires dynamic modulus test results at a minimum of three loading frequencies to thoroughly characterize the HMA stiffness. In addition, it requires rheological data for the asphalt binder, including complex modulus (G^*) and phase angle (δ) measurements at 10 rad/s (1.59 Hz), tested at no fewer than three different temperatures. Three temperature data points are necessary to determine the appropriate fitting coefficients of the Arrhenius model, such as A and *VTS*. The test data from the asphalt mixture and the asphalt binder can accurately describe how the asphalt mixture, and thus the flexible pavement will perform. In Level 2, the dynamic modulus test is excluded. Instead, the asphalt mixture gradation is used, along with the same asphalt binder rheological

Asphalt Dynamic Modulus (Input Level: 1)

T (ºF)	0.1 Hz	1 Hz	10 Hz
14	3116621	3564464	3968845
39.2	1812726	2347123	2852122
68	594760	1043644	1574997
104	95741	225429	480451
131	31722	79184	189232

Asphalt Binder

Temperature (ºF)	Binder Gstar (Pa)	Phase angle (deg)
168.8	4880	81.1
179.6	2390	83.4
190.4	1180	85.2

(a)

Asphalt Dynamic Modulus (Input Level: 2)

Gradation	Percent Passing
3/4-inch sieve	100
3/8-inch sieve	95.3
No.4 sieve	69.7
No.200 sieve	5.5

Asphalt Binder

Temperature (ºF)	Binder Gstar (Pa)	Phase angle (deg)
168.8	4880	81.1
179.6	2390	83.4
190.4	1180	85.2

(b)

Asphalt Dynamic Modulus (Input Level: 3)

Gradation	Percent Passing
3/4-inch sieve	100
3/8-inch sieve	95.3
No.4 sieve	69.7
No.200 sieve	5.5

Asphalt Binder

Parameter	Value
Grade	Superpave Performance Grade
Binder Type	70-22
A	10.299
VTS	-3.426

(c)

Figure 5.1 MEPDG Required Data Input: (a) Level 1, (b) Level 2, and (c) Level 3.

characteristics used in Level 1, in predictive models to estimate *E** under a range of loading frequencies. Finally, Level 3 relies on aggregate gradation and asphalt binder performance grade (PG) to determine the Witczak's empirical model coefficients necessary for generating the *E** master curve. This approach significantly reduces the need for laboratory testing while sacrificing some degree of accuracy compared to Levels 1 and 2. Figure 5.2 shows the relaxation modulus curves determined for an asphalt mixture using each of the three data input levels. The figure clearly shows there is considerable difference in E(t) over the range of loading times between the three levels.

There are two E* empirical predictive models to generate the *E** master curves, including the NCHRP 1-37, viscosity-based model, and the NCHRP 1-40D, asphalt binder shear modulus (*G**) based model. Both models were developed by Witczak and his colleagues (ARA, 2004; Witczak & Bari, 2004).

5.1.1 Witczak Viscosity-Based E Model*

This model was first implemented in the initial version of the MEPDG and was developed using 2,750 measured *E** data points from 205 different HMA mixtures. It predicts the *E** at various temperatures based on information, including aggregate gradation, volumetric properties, loading frequency, and asphalt binder viscosity. Equation 5.1 represents the viscosity-based model, which includes asphalt mixture volumetric properties, asphalt binder viscosity, and aggregate gradation.

where ρ_{200}, ρ_4, ρ_{38}, ρ_{34} are gradation parameters representing the percentage of aggregate retained or passing certain sieves, V_a

$$\log_{10}\left(E^*\right) = -1.249937 + 0.02923\,\rho_{200} - 0.001767\left(\rho_{200}\right)^2 - 0.002841\,\rho_4 - 0.058097\,V_a - 0.82208\left(\frac{V_{beff}}{V_{beff}+V_a}\right) + \frac{3.871977 - 0.0021\,\rho_4 + 0.003958\,\rho_{38} - 0.000017\left(\rho_{38}\right)^2 + 0.00547\,\rho_{34}}{1 + e\left(-0.603313 + 0.31335\log(f) - 0.39353\log(\eta)\right)} \quad \text{(Eq. 5.1)}$$

is the air voids content by volume, V_{beff} is the effective binder content by volume, η is the binder viscosity (in poise) at the specified age and temperature, f is the loading frequency (Hz), and *E** is the dynamic (complex) modulus of the HMA (in units of 10^5 psi).

A careful examination of this model indicates that two main terms are used. The first term includes information related to the aggregate gradation and asphalt mixture volumetric properties. In contrast, the second term (fraction) involves information regarding aggregate gradation, asphalt binder viscosity, and

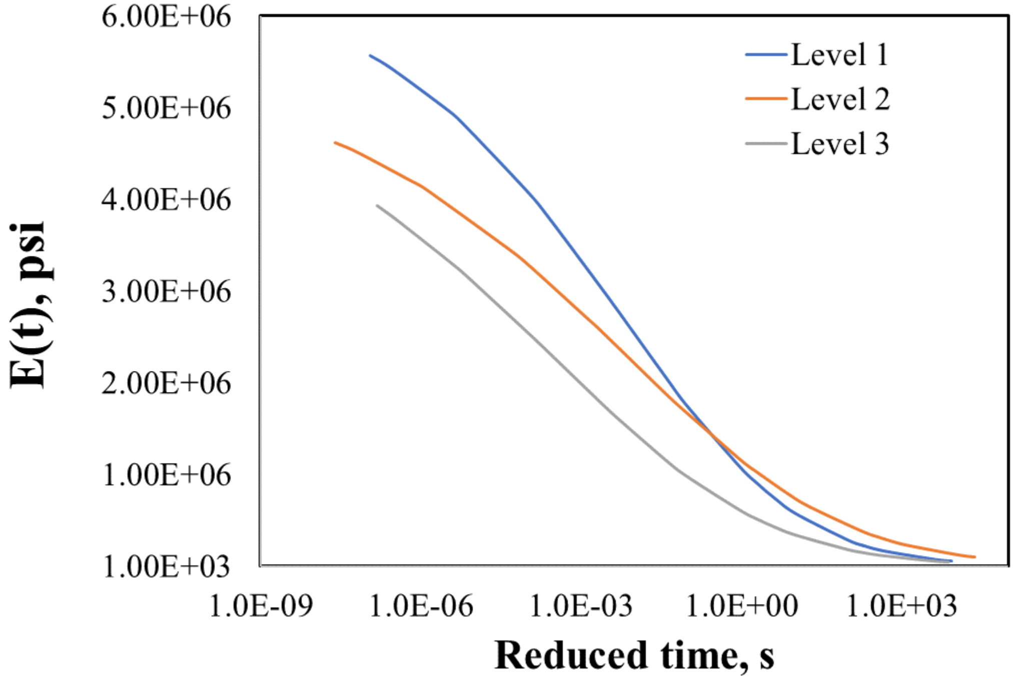

Figure 5.2 Relaxation Modulus for an Asphalt Mixture Determined at the Three MEPDG Levels.

loading frequency. The shape of these two terms is like a sigmoidal function shown below.

$$\log\left(\left|E^*\right|\right) = \delta + \frac{\alpha}{1 + e^{\beta + \gamma \log(f_r)}}$$

By comparing the Witczak model with the sigmoidal mathematical function, it becomes possible to match each coefficient in the sigmoidal function with the corresponding term used in the Witczak model, as shown below:

$$\delta = -1.249937 + 0.02923\rho_{200} - 0.001767\left(\rho_{200}\right)^2 - 0.002841\rho_4 - 0.058097V_a - 0.82208!\left(\frac{V_{\text{beff}}}{V_{\text{beff}} + V_a}\right);$$

$$\alpha = 3.871977 - 0.0021\rho_4 + 0.003958\rho_{38} - 0.000017\left(\rho_{38}\right)^2 + 0.00547\rho_{34};$$

$$\beta = -0.603313 - 0.39353\log\left(\eta\right);$$

$$\gamma = -0.39353\log\left(\eta\right).$$

As discussed in the sigmoidal coefficient analysis (Section 4.1), an increase in C_1 (equal to δ) results in a fixed vertical shift in the E^* master curve over all loading frequencies, indicating that δ is independent of loading frequency. Therefore, δ fails to represent the viscoelastic characteristics in any significant sense but only influences the magnitude of E^* values. However, the volume of air voids (V_a) and effective binder (V_{beff}) affect the E^* considerably at different loading frequencies. For example, Hofko et al. (2012) showed that a change in V_a affects the E^* value with a nonlinear behavior over all loading frequencies (Figure 5.3). However, the Witczak model ignores such complexities by excluding the viscoelastic characteristics between loading frequency and air voids content in asphalt mixtures.

In the Pavement ME Design software (calibrated under NCHRP 1-40D), the G^*-based E^* model is used to overcome the asphalt binder viscosity data concern of the previous model. In this revision, the Superpave asphalt binder data (G^* and δ) are used in the model to improve the accuracy of the estimated E^* master curve, instead of viscosity data. This model is a modified version of Bari and Witczak's predive model originally developed in 2005 (Bari, 2005; Witczak et al., 2007).

$$\log_{10}\left(\mathrm{E}^*\right) = 0.02 + 0.758\left(|G_b^*|^{-0.0009}\right) \left(\begin{array}{l} 6.8232 - 0.03274\rho_{200} + 0.00431\left(\rho_{200}\right)^2 + 0.0104\rho_4 - 0.00012\left(\rho_4\right)^2 \\ +0.00678\rho_{38} - 0.00016\left(\rho_{38}\right)^2 - 0.0796V_a - 1.1689\left(\dfrac{V_{\text{beff}}}{V_a + V_{\text{beff}}}\right) \end{array}\right) + \frac{1.437 + 0.03313V_a + 0.6926\left(\dfrac{V_{\text{beff}}}{V_a + V_{\text{beff}}}\right) + 0.00891\rho_{38} - 0.00007\left(\rho_{38}\right)^2 - 0.0081\rho_{38}}{1 + \mathrm{e}(-4.5868 - 0.81716\log(|G_{\mathrm{b}}^*|) + 3.2733\log_{38}(\delta))}$$

where $|G_b^*|$ is the asphalt binder dynamic shear complex modulus (psi) and δ is the asphalt binder phase angle (degree). Like the previous version, this revised model's first term only affects the magnitude of the E^* value. However, it is well known that the asphalt binder properties and V_a not only affect E^* magnitude, but also, they affect E^* in nonlinear behavior at different loading frequencies. Therefore, the Witczak empirical model appears to oversimplify this aspect by overlooking the viscoelastic interactions of loading frequency and V_a within an asphalt mixture.

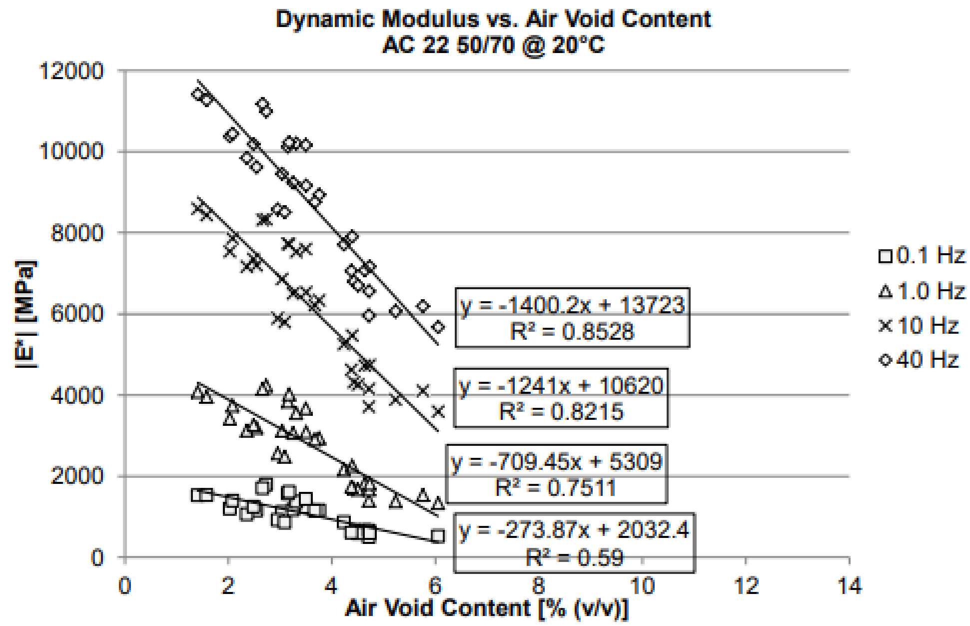

Figure 5.3 Air Voids Content Effects On E* At Different Loading Frequencies.

6. RESULTS AND DISCUSSIONS

The accuracy and effectiveness of the mechanistic method for backcalculating the *E** master curve is determined by analyzing the FWD and laboratory test data on several flexible pavement sections. The experimental plan included FWD tests and concurrent field-core sampling for laboratory *E** measurement. *E** curves were also obtained through the ViscoWave method using the same FWD time-history data used in the mechanistic model. The laboratory-measured *E** master curve serves as the benchmark for comparing the mechanistic and ViscoWave results. These comparisons allow the evaluation of the reliability and accuracy of the developed model.

6.1 US 27

Figure 6.1 shows the US 27 pavement surface appearance on the day of the FWD testing. As summarized in Table 6.1, this full-depth flexible pavement structure consists of three asphalt layers placed on a subgrade. Field-cored specimens were taken immediately after the FWD testing from the testing locations for laboratory dynamic modulus testing. Figure 6.2 presents the backcalculated *E** master curves determined by both the ViscoWave and the mechanistic method, as well as the laboratory-determined *E** master curve.

Figure 6.2a indicates that for the surface layer, the mechanistically determined *E** master curve compares favorably to the laboratory dynamic modulus test results over the entire load frequency range. In contrast, the ViscoWave curve consistently underestimates the modulus values, specifically at frequencies below 100 Hz, while it overestimates them at frequencies beyond 100 Hz. The intermediate layer data in Figure 6.2b again indicates the mechanistic method produces an *E** master curve more closely resembling the laboratory dynamic modulus test curve than does ViscoWave at the mid-range loading frequencies. The base layer results, Figure 6.2c, further confirm the better accuracy of the mechanistic approach compared to the ViscoWave method in generating the *E** master curve.

6.2 SR 67

Figure 6.3 illustrates the appearance of the SR 67 pavement on the day of FWD testing. As indicated in Table 6.2, this pavement consists of three asphalt layers placed on an approximately 15,000 psi modulus subgrade with an. As shown in Figure 6.3, this pavement contains a single traffic lane in each direction.

Figure 6.4. shows the backcalculated and laboratory-measured *E** master curves for all pavement layers. As shown, the mechanistic result again shows a notable consistency with the DM test data across the surface, intermediate, and base layers. In contrast, the ViscoWave *E** predictions tend to deviate more significantly. For the surface layer (Figure 6.4a) the mechanistic curve remains close to the laboratory data over the entire loading frequency range. In contrast, ViscoWave overestimates the modulus, particularly in the mid-to-high loading frequencies, although it converges with DM test results at mid to lower frequencies. Figure 6.4b presents the *E** master curves generated for the intermediate layer. As shown, the curve generated by the mechanistic approach shows closer *E** values to the DM test result, while the ViscoWave-generated curve shows lower accuracy over the entire loading frequency range. Additionally, an identical divergence is observed in the *E** master curve generated by the ViscoWave tool (refer to Figure 6.4c). In contrast, the mechanistic approach exhibits a more accurate *E** master

Figure 6.1 US 27 Test Section.

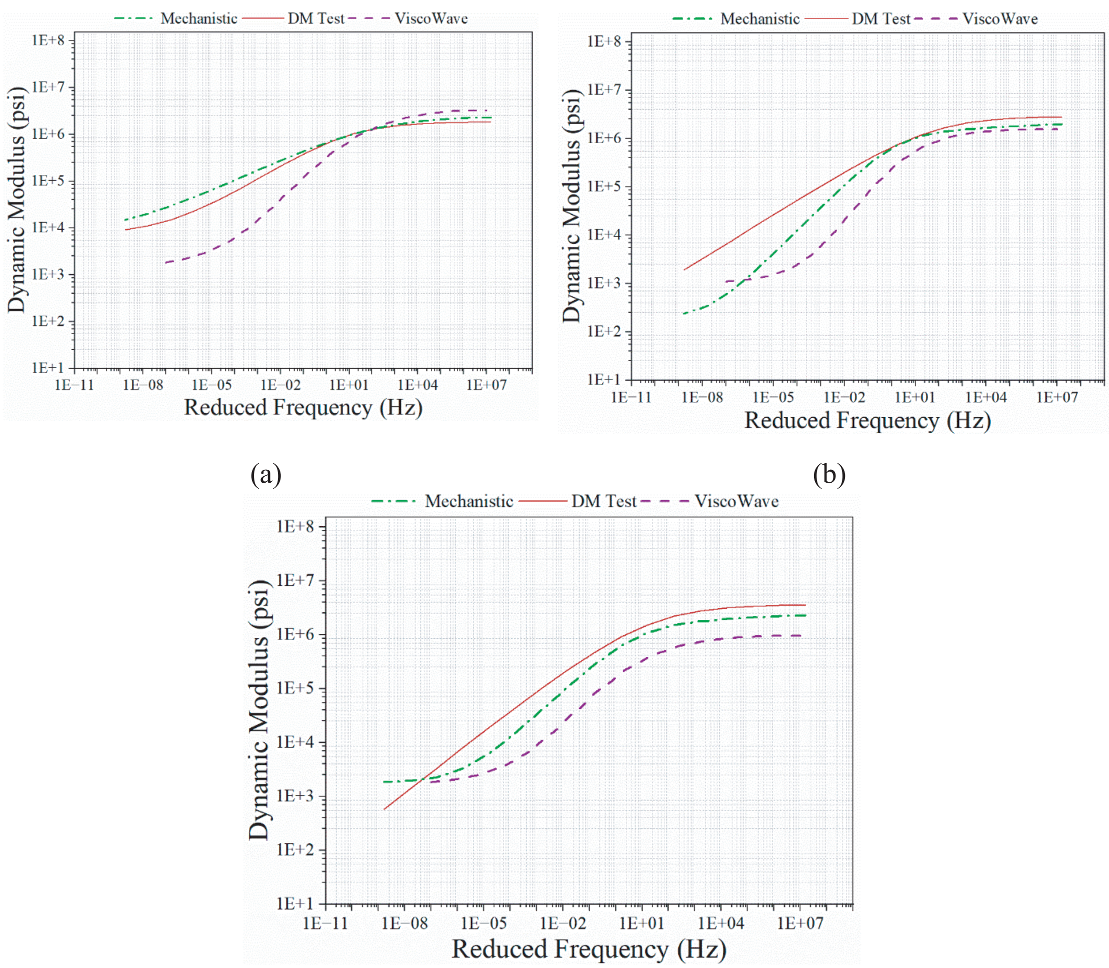

(a) (b)

(c)

Figure 6.2 *E** Master Curves for the US 27 Pavement Layers: (a) Surface, (b) Intermediate, and (c) Base.

TABLE 6.1
US 27 Pavement Structure Information.

Pavement Layer	Thickness (in.)	Modulus (psi)
Surface	1.5	–
Intermediate	2.5	–
Base	11.0	–
Subgrade	–	15,000

Figure 6.3 SR 67 Test Section.

TABLE 6.2
SR 67 Pavement Structure Configuration Information.

Pavement Layer	Thickness (in.)	Modulus (psi)
Surface	1.5	–
Intermediate	3.0	–
Base	11.5	–
Subgrade	–	15,000

curve than the one generated by the ViscoWave procedure. One possible explanation for the low accuracy in the ViscoWave method is the seed values, which need to be defined within a close range of the expected data; otherwise, such inaccuracies may occur.

6.3 SR 545

Figure 6.5 illustrates the appearance of the SR 545 pavement on the day of FWD testing. The pavement structure information, summarized in Table 6.3, indicates that this pavement is a full-depth asphalt pavement placed on a subgrade, with the subgrade modulus being approximately 13,000 psi. As shown in Figure 6.5, this pavement contains a single traffic lane in each direction. This pavement includes a thicker base layer than SR 67 and US 20 and a lower subgrade modulus.

Figure 6.6 shows the *E** master curves obtained through two backcalculation approaches and the laboratory DM test for the all-pavement layers. As shown in Figure 6.6a, the *E** master curve generated by the mechanistic method closely follows the laboratory DM test curve at higher loading frequencies; however, a small divergence occurs when frequency decreases to the lower end of the DM test curve. The ViscoWave-generated *E** master curve, however, appears to lag the mechanistic and DM test results at mid to low loading frequencies, indicating an underestimation of stiffness under low loading frequencies or high pavement temperatures. This difference reduces to some extent at higher frequencies; however, the difference is still very

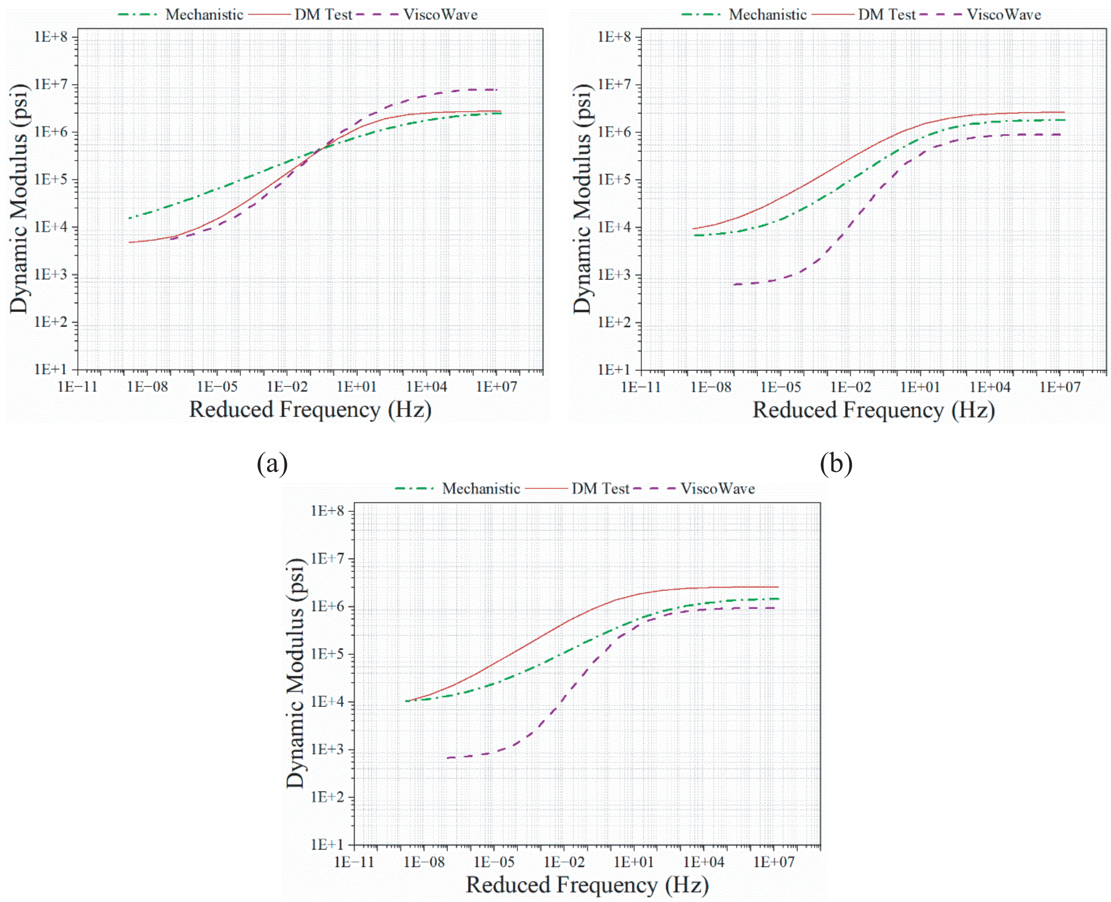

Figure 6.4 *E** Master Curves for the SR 67 Flexible Pavement: (a) Surface Layer, (b) Intermediate Layer, and (c) Base Layer.

Figure 6.5 SR 545 Test Section.

TABLE 6.3
SR 545 Pavement Structure Configuration Information.

Pavement Layer	Thickness (in.)	Modulus (psi)
Surface	1.5	–
Intermediate	2.5	–
Base	11.5	–
Subgrade	–	13,000

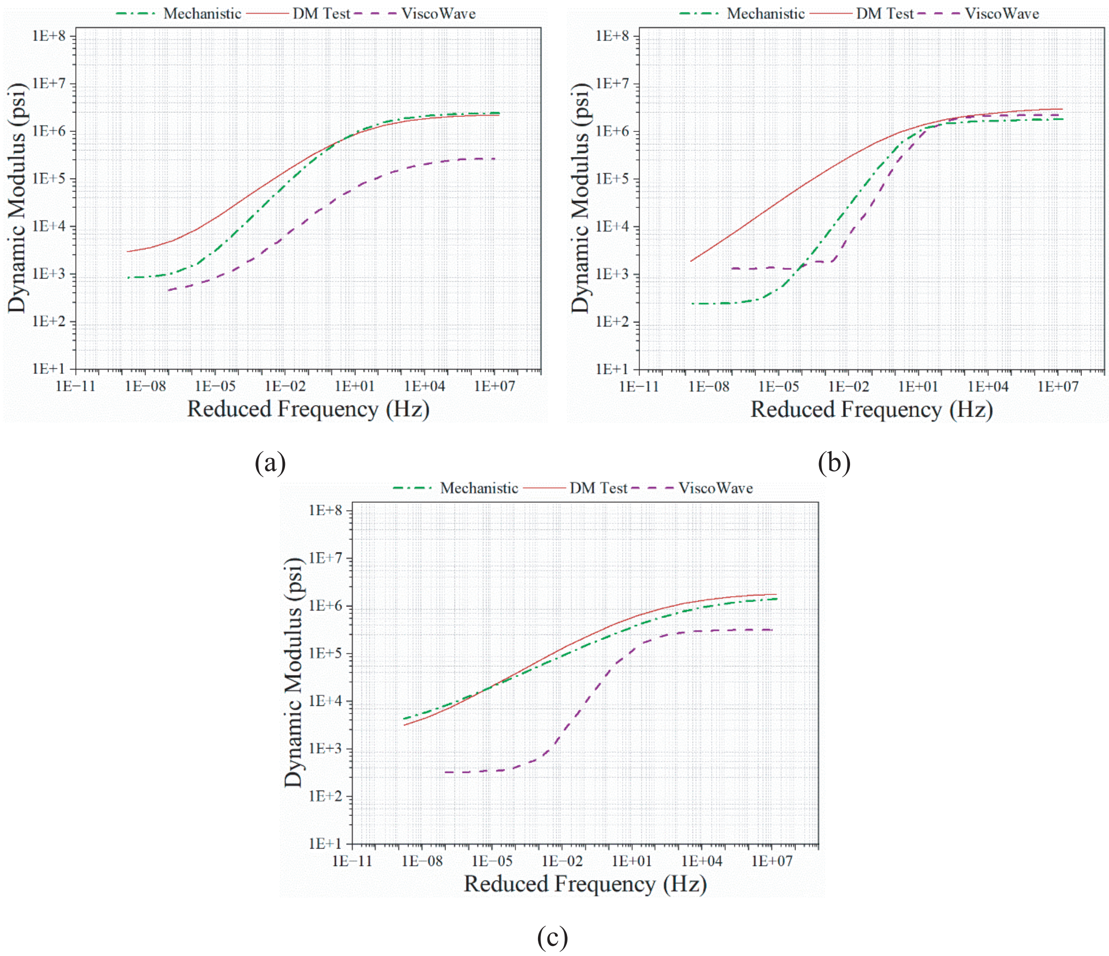

Figure 6.6 *E** Master Curves for the SR 545 Pavement: (a) Surface Layer, (b) Intermediate Layer, and (c) Base Layer.

noticeable compared to the mechanistic method's results. Note that the surface layer tends to undergo the largest temperature deviations, so even minimal errors in temperature may cause visible differences in the modulus curves.

Figure 6.6b shows the analysis related to the intermediate layer. In this case, both backcalculation procedures generate similar curves, neither of which is clearly dominant over the other. This result suggests that there may be noise in the FWD time history data. Next, Figure 6.6c presents the E^* master curves for the base layer. The E^* master curve obtained from the mechanistic approach better approximates the laboratory-measured E^* master curve than ViscoWave, notably over the entire loading frequency range. Although ViscoWave can estimate the general shape of the master curve, it consistently underestimates the E^* values compared to laboratory measurements. As the base layer is thicker and directly in contact with the subgrade, subgrade support and transition assumptions can significantly affect backcalculation accuracy.

6.4 SR 32

Figure 6.7 illustrates the appearance of the SR 32 flexible pavement surface on the day of FWD testing. The pavement structure information, summarized in Table 6.4, indicates that this pavement is a full-depth asphalt pavement placed on an approximately 13,000 psi modulus subgrade. As shown, this pavement contains a single traffic lane in each direction with visible sealed surface cracks.

Figure 6.8 presents the *E** master curves obtained from both backcalculation techniques and the laboratory-measured DM test result for the SR 32 pavement section. As evident from Figure 6.8a, the mechanistic approach generates a very close *E** master curve compared to that obtained through the ViscoWave tool. The ViscoWave overestimates the E* values at higher frequencies and underestimates the *E** values at lower frequencies. According to the sigmoidal function analysis, the C4 coefficient is the cause of such behavior in this curve.

Figure 6.8b indicates that the mechanistic-determined curve again remains near the DM test result, especially in the mid-to-high frequency range. ViscoWave, however, underpredicts the *E** master curve over nearly all loading frequencies. One potential explanation for this deficiency is that the intermediate layer tends to have complex shear and temperature gradients and thus would be more sensitive to assumptions about wave propagation, damping, or interface conditions between layers. Small variations in these parameters may result in significant variations in the backcalculated master curve.

Figure 6.8c presents the *E** master curves obtained through all three methods. The mechanistic approach underestimates the E* value at mid to high loading frequencies while overestimating at frequencies lower than 10^{-5} Hz. Meanwhile, the ViscoWave-generated master curve remains below both curves throughout the frequency range, converging somewhat as frequency increases but never fully matching the laboratory-measured values. The increased base layer thickness and related uncertainties regarding subgrade support to add complexity to backcalculation algorithms. However, the mechanistic approach seems more capable of coping with such difficulties than does the wave-based approach.

TABLE 6.4
SR 32 Pavement Structure Information.

Pavement Layer	Thickness (in.)	Modulus (psi)
Surface	1.5	–
Intermediate	2.5	–
Base	12	–
Subgrade	–	13,000

6.5 US 20

Figure 6.9 illustrates the appearance of the US 20 flexible pavement surface on the day of FWD testing. The pavement structural information, summarized in Table 6.5, indicates that the consists of three asphalt layers placed on subgrade, the subgrade modulus being approximately 18,000 psi. As shown in Figure 6.9, this pavement contains a single traffic lane in each direction and is in good surface condition. Additionally, the surface layer of this pavement is thicker compared to the previous analyzed sections.

Figure 6.10 presents the final *E** master curves for all pavement layers for the US 20 pavement section. In Figure 6.10a, the mechanistic approach underestimates the *E** values of the surface layer over most loading frequencies, except for frequencies below 10^{-5} Hz. Conversely, ViscoWave overestimates the

Figure 6.7 SR 32 Test Section.

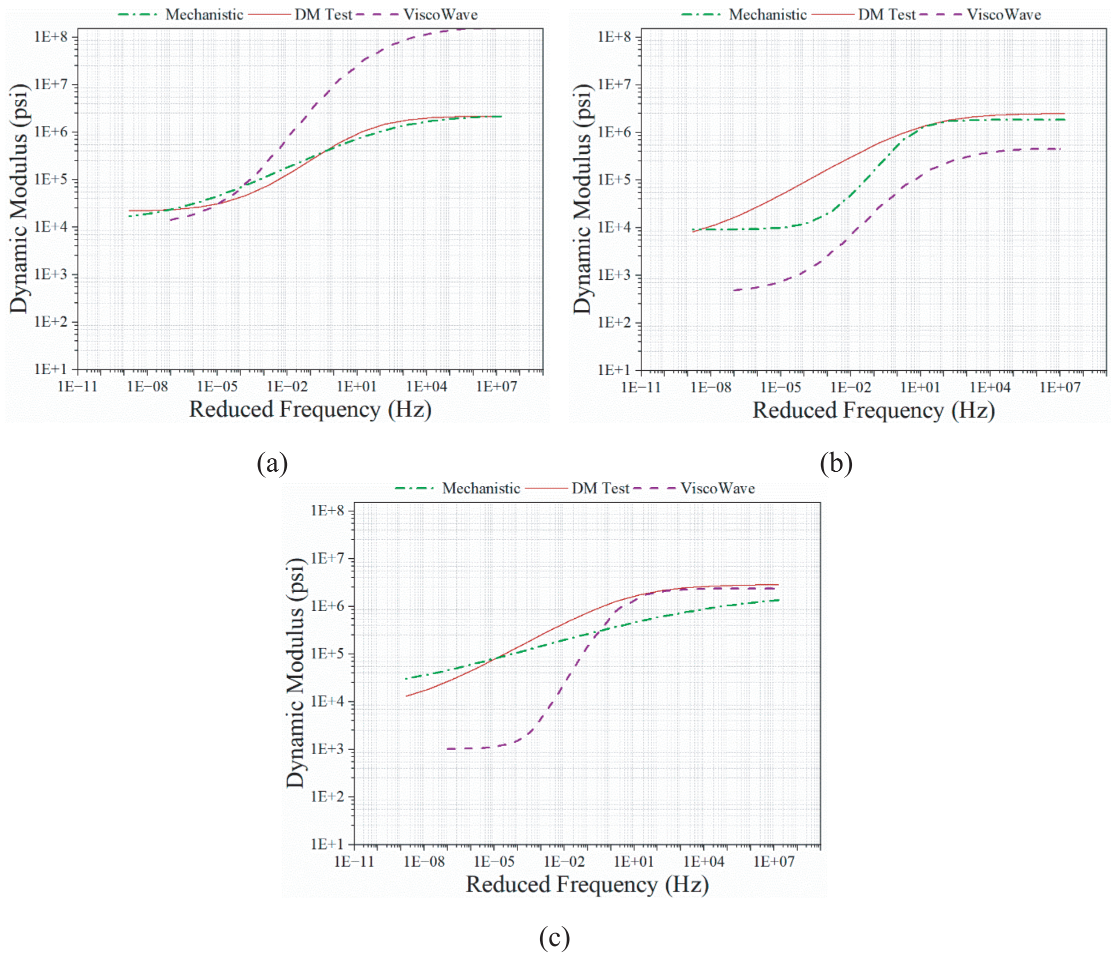

Figure 6.8 *E** Master Curves for the SR 32 Pavement: (a) Surface Layer, (b) Intermediate Layer, and (c) Base Layer.

Figure 6.9 US 20 Pavement Section.

TABLE 6.5
US 20 Pavement Structure Information.

Pavement Layer	Thickness (in.)	Modulus (psi)
Surface	2.0	–
Intermediate	2.5	–
Base	11.0	–
Subgrade	–	18,000

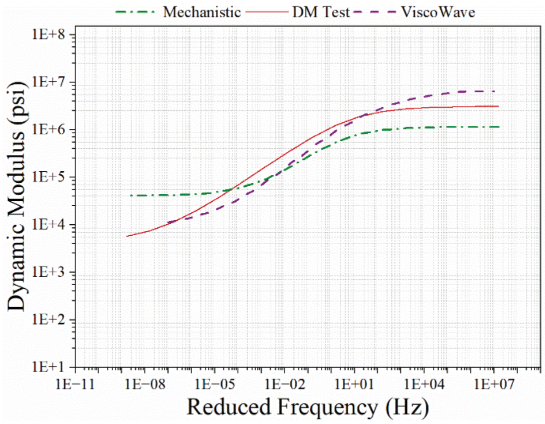

(a)

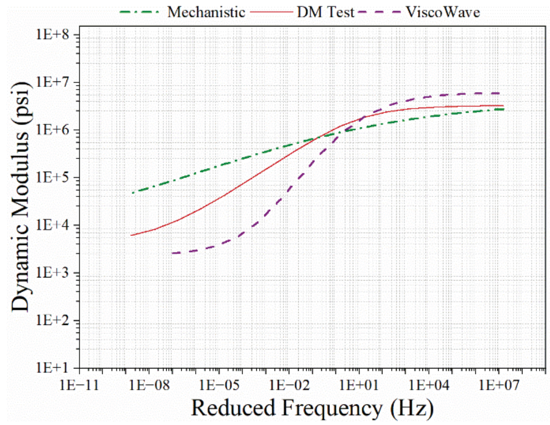

(b)

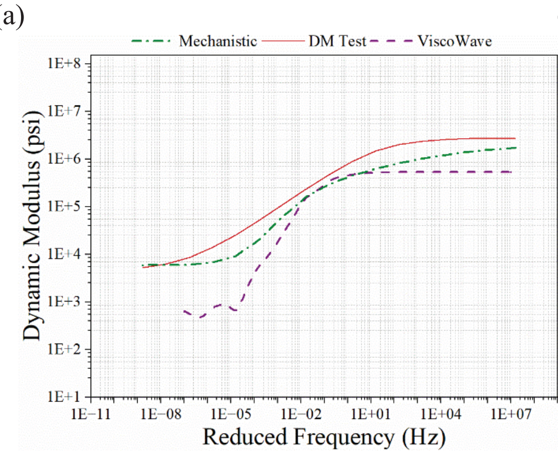

(c)

Figure 6.10 *E** Master Curves for the US 20 Pavement Section: (a) Surface Layer, (b) Intermediate Layer, and (c) Base Layer.

*E** values at loading frequencies above 100 Hz while underestimating it at lower frequencies. Although minor variations exist between the two backcalculated curves, both demonstrate high accuracy in this specific case.

6.6 US 31

Figure 6.11 illustrates the condition of the US 31 flexible pavement on the day of FWD testing. The pavement structural information, summarized in Table 6.6, indicates that this pavement is a full-depth asphalt pavement placed on a subgrade with an approximate modulus of 14,000 psi. As shown in Figure 6.11, this pavement contains three traffic lanes in each direction and is in good surface condition.

Figure 6.12 shows the *E** master curves obtained from both backcalculated methods along with the actual curve obtained from the laboratory DM test. In Figure 6.12a, the mechanistic approach closely estimates the *E** values at frequencies above 10 Hz but tends to overestimate the values at frequencies below 10 Hz. In contrast, the ViscoWave method significantly overestimates the *E** master curve at the entire frequency range. Comparing two backcalculated *E** master curves, the result from the mechanistic method shows greater accuracy than the one generated by the ViscoWave method.

Figure 6.12b indicates that the backcalculated *E** master curves obtained from both backcalculation methods fall below the actual *E** master curve at all loading frequencies. However, the mechanistic method estimates *E** values that align fairly

Figure 6.11 US 31 Test Section.

TABLE 6.6
US 31 Pavement Structure Configuration Information.

Pavement Layer	Thickness (in.)	Modulus (psi)
Surface	1.8	–
Intermediate	2.5	–
Base	10.5	–
Subgrade	–	14,000

closely with the laboratory data over most of the frequency range, maintaining a fairly consistent gap that narrows slightly at higher frequencies. In contrast, the ViscoWave method significantly underestimates the *E** curve relative to the DM test results.

Figure 6.12c presents the results for the base layer. Here, the mechanistic method produces more precise *E** values than those generated by the ViscoWave method at all loading frequencies. Overall, the mechanistic method generally demonstrates better agreement with the laboratory results.

6.7 I-69

Figure 6.13 illustrates the surface condition of the Interstate 69 (I-69) flexible pavement section on the day of FWD testing. As pavement structural information summarized in Table 6.7, this pavement consists of three asphalt layers placed on a subgrade with an approximate modulus of 12,000 psi. This pavement contains three traffic lanes in each direction and is in good functional performance condition. Moreover, the core specimens were obtained from the speed lane (lane 3), as the core location was marked in the image.

Figure 6.14 shows the backcalculated and laboratory-measured *E** master curves for all pavement layers. In Figure 6.14a, both backcalculated curves obtained from the ViscoWave and mechanistic methods overestimate the modulus values. However, the mechanistic-determined curve is closer to the actual modulus than the ViscoWave-generated modulus. Moreover, the mechanistic approach produces almost the same modulus values as laboratory-measured values at frequencies greater than 1 Hz. In contrast, the modulus value generated by the ViscoWave tool has a considerable distance from the actual values at almost all loading frequencies.

Figure 6.14b and Figure 6.14c present the results for intermediate and base layers, respectively. A similar trend can be seen for both layers, whereas the mechanistic-determined *E** master curves more closely match laboratory-measured modulus compared to ViscoWave-generated master curves. The ViscoWave method underestimates the *E** master curve for both intermediate and base layers by a notable difference.

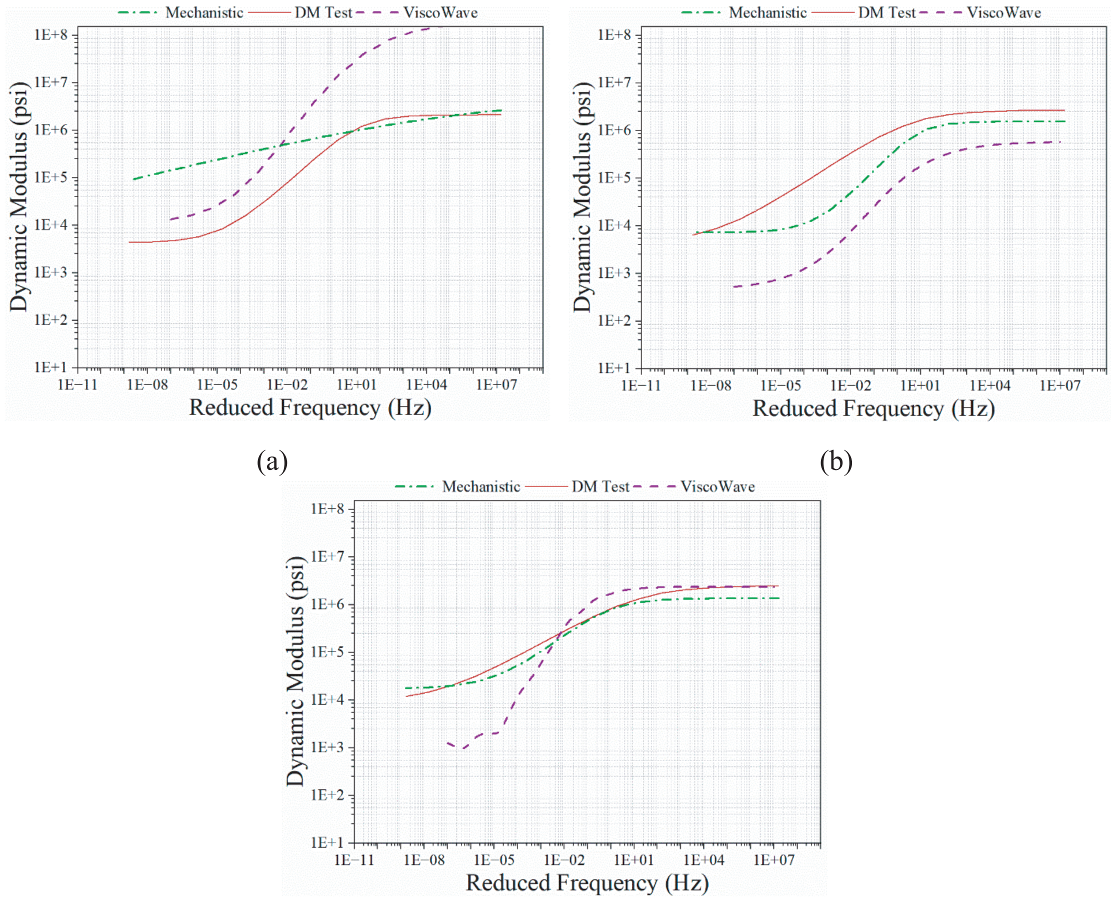

(a) (b)

(c)

Figure 6.12 *E** Master Curves for the US 31 Pavement: (a) Surface Layer, (b) Intermediate Layer, and (c) Base Layer.

Figure 6.13 I-69 Test Section.

TABLE 6.7
I-69 Pavement Structure Configuration Information.

Pavement Layer	Thickness (in.)	Modulus (psi)
Surface	2.0	–
Intermediate	3.0	–
Base	10.0	–
Subgrade	–	12,000

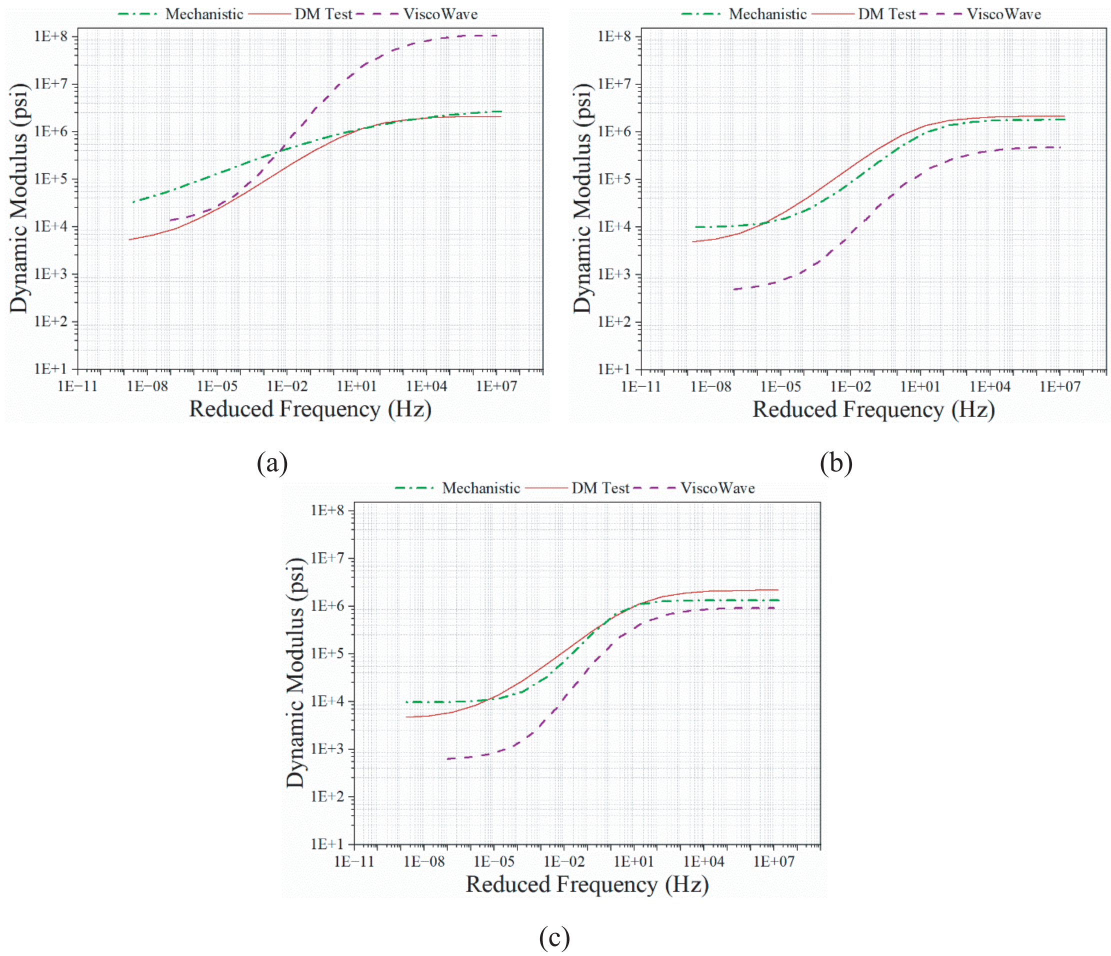

Figure 6.14 *E** Master Curves for the I-69 Pavement: (a) Surface Layer, (b) Intermediate Layer, and (c) Base Layer.

6.8 Evaluate FWD Time History Intervals Effects in Mechanistic Approach

The mechanistic method described in Section 2.10 decomposes the FWD load pulse into numerous small-time segments, each approximated by a sinusoidal wave. This procedure, referred to as Time Interval Steps (TIS), is responsible for both the accuracy of the backcalculated *E** values and the related computational processing time. A parametric study was conducted using TIS values of 3, 5, 10, 15, and 25 to determine an optimum balance between these factors. The obtained *E** master curves were compared to the laboratory DM test data.

Figure 6.15 presents the results for all TISs; as shown, smaller TIS (i.e., 5 and 10) produce E* values close to the DM test results. The differences between *E** master curves are pronounced at lower loading frequencies, where the viscous portion of the asphalt mixture is predominant in the asphalt mixture's mechanical performance. However, higher TISs require more processional time as the model needs to process a larger number of sinusoidal segments to construct the *E** master curve. Thus, 10-time interval step is well enough for producing *E** master curves of asphalt pavement using the mechanistic method.

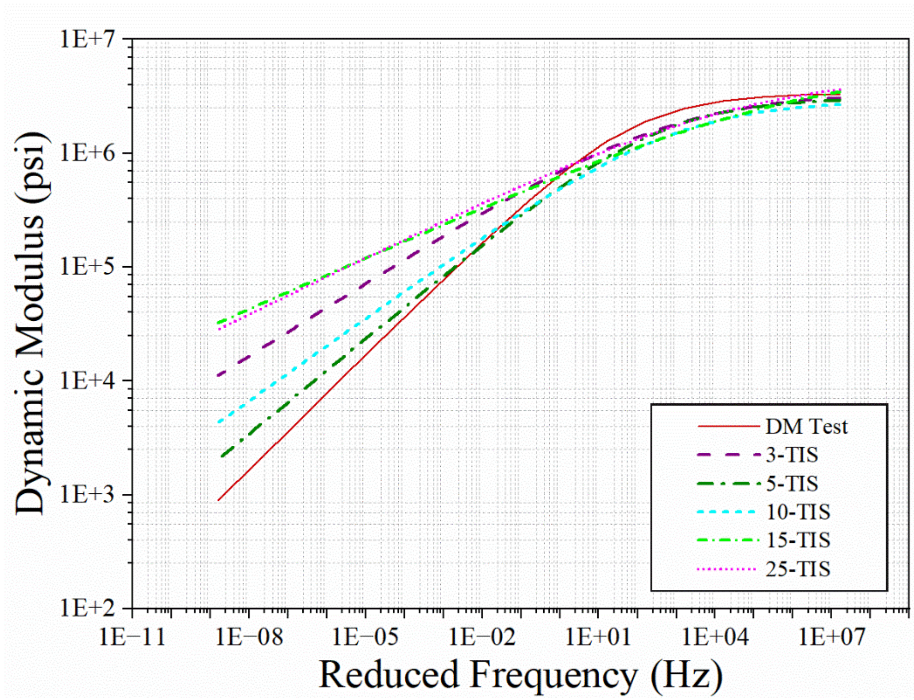

Figure 6.15 *E** Master Curves Obtained at Several Time-Interval Steps.

6.9 Parametric Study of Mechanistic Approach

This section presents the sensitivity analysis of the backcalculated *E** master curve to the pavement layer information, such as layer thickness and Poisson ratio (ν). To this end, a small thickness tolerance is used to evaluate how slight thickness variability in the pavement layer would affect the resulting *E** master curve. Table 6.8 presents the amount of thickness tolerance applied to each layer, along with the actual values used to generate the baseline *E** master curve. As shown in this table, a half-inch thickness tolerance was applied to the surface layer because the typical measurement error for the surface layer is approximately ± 0.5 in. Following the same philosophy, the intermediate and base layers are each subject to a 1- and 2-in. thickness tolerance. The 2-in. tolerance for the base was chosen based on practical observation during the field coring process: sometimes, the full length of the core is not recovered due to moisture damage or breaking during coring, resulting in the loss of aggregate and, subsequently, a shorter core specimen.

Additionally, a 10% error is considered for the Poisson ratio (ν) to examine how it would affect the *E** master curve. To this end, every parameter other than the parameter under analysis is left at the reference level, and the resulting *E** master curve would later be compared with laboratory-measured *E** master curve. It should be noted that the SR 67 data was used for the analysis presented in this section.

6.3.1 Surface Layer Thickness Sensitivity

In this scenario, only the surface layer thickness is increased by 0.5 in. to evaluate how this change affects the mechanistic backcalculated *E** master curve for all three layers. Figure 6.16 indicates that the surface layer's ν significantly impacts the backcalculation results for the surface layer, following a small effect on the intermediate layer's *E** master curve and a negligible impact on the base layer's *E** master curve. Figure 6.16a shows that increasing the surface layer thickness from 1.5 to 2 in. shifts the backcalculated *E** master curve closer to the DM test results because it causes a downward shift at mid-to-low loading frequency compared to the baseline curve (based on actual input data). In contrast, the backcalculated *E** master curves for the intermediate and base layers indicate a small change. The base layer's *E** master curve (Figure 6.16b), in particular, remains constant and marginally close to the baseline, which implies that in a deeper layer, the change in the surface layer's thickness is not as impactful as it is for the surface layer. This may be related to the vertical stress distribution that does not change considerably at depth, with a slight change in the top few inches.

This analysis implies that even a tiny variation in surface layer thickness, either in measurement or estimation, can significantly impact the backcalculation results for the surface layer. These findings highlight the importance of the top layer's thickness: misestimation of even half an inch can shift the entire

TABLE 6.8
Baseline Values Used in the Parametric Study and Corresponding Variation Amounts.

Pavement Layer	Thickness (in.)	Poisson's Ratio	Thickness Change (in.)
Surface	1.5	0.35	+0.5
Intermediate	2.5	0.35	+1
Base	9	0.35	+2

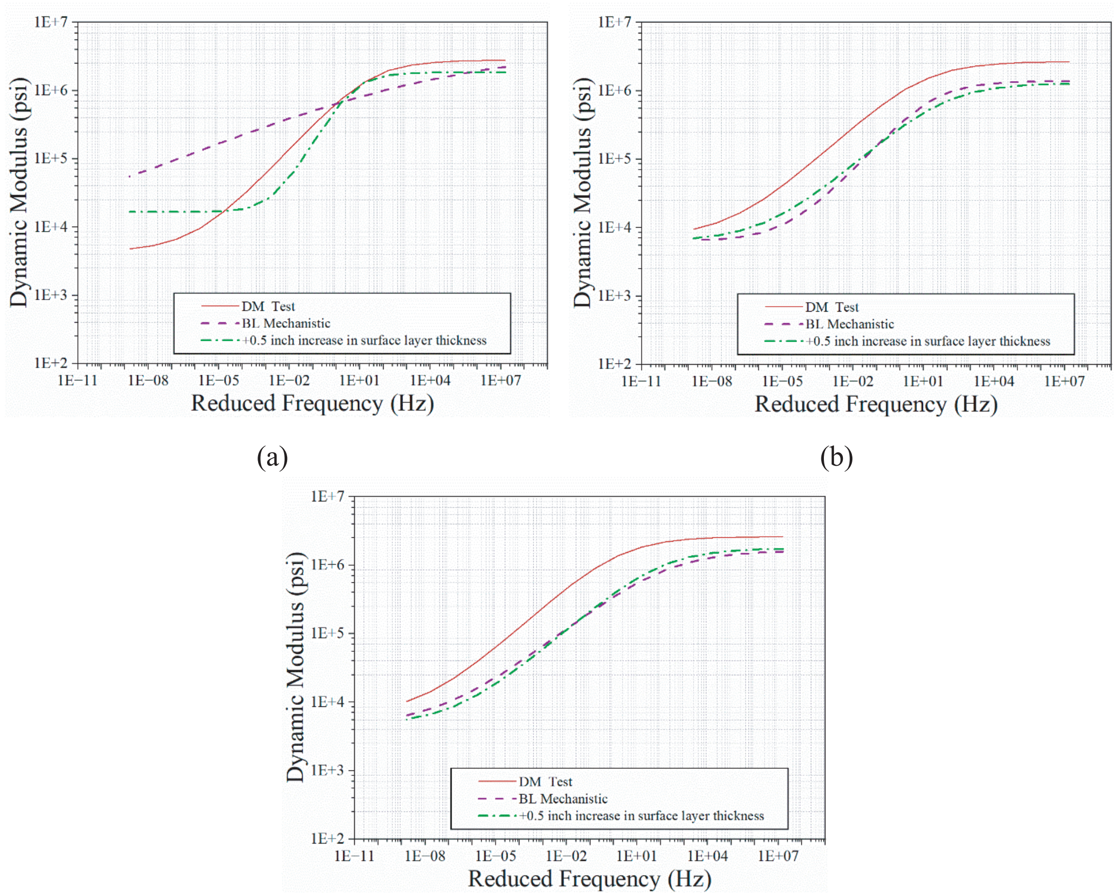

Figure 6.16 Backcalculated E^* Master Curves Under a 0.5-in. Increase in the Surface Layer Thickness: (a) Surface Layer, (b) Intermediate Layer, and (c) Base Layer.

surface layer's E^* master curve, leading to inaccurate determination of in-situ performance.

6.3.2 Base Layer Thickness Sensitivity

This section evaluates the effect of a small change, i.e., 2 in., in the base layer thickness on the backcalculated E^* master curves for all pavement layers. As shown in Figure 6.18, the highest change occurs in the surface layer's E^* master curve, followed by the base layer, while the least change attributes to the intermediate layer. Figure 6.18a indicates that the surface layer's backcalculated curve shows a notable downward shift at mid-to-low loading frequencies that aligns more closely with the DM test curve. Figure 6.18b demonstrates that increasing the base layer's thickness up to 2 in. affects the intermediate layer's E^* master curve at mid-range loading frequency with almost no change observed at frequencies higher than 1 Hz or lower than 10^{-6} Hz. On the other hand, Figure 6.18c shows an upward shift occurring over the entire frequency range in the base layer's E^* master curve that takes it closer to the DM test curve.

The sensitivity analysis demonstrated that the surface layer is most affected by thickness variations in any of the asphalt layer thicknesses. This variation is caused by minor inaccuracies in thickness measurement from field-core inspection or unreliable construction records that lead to a mismatch between the actual and model-assumed configuration. Although the dynamic modulus is a fundamental material property and is not a function of dimension, the deflection response under FWD tests is highly dependent on all pavement layer thickness. The backcalculation method based on such deflection information is highly sensitive to layer thickness and produces a backcalculated master curve in terms of E^* with a high degree of dependence on layer thickness.

In conclusion, a reliable backcalculated E^* master curve requires precise thickness measurements, which can be obtained through careful coring, NDT techniques like Ground Penetration Radar (GPR), or reliable construction records. Even minor variations in pavement layer thickness may misrepresent the pavement's structural capacity, which could result in suboptimal M&R strategies.

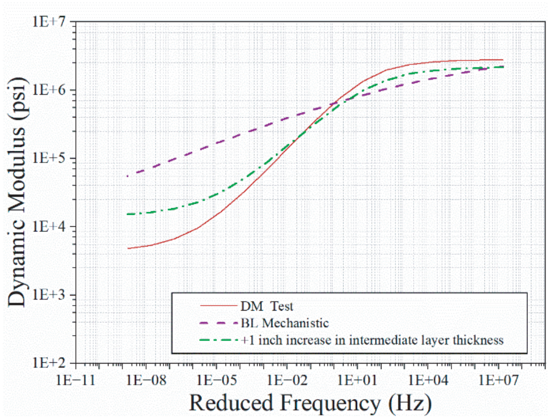

(a)

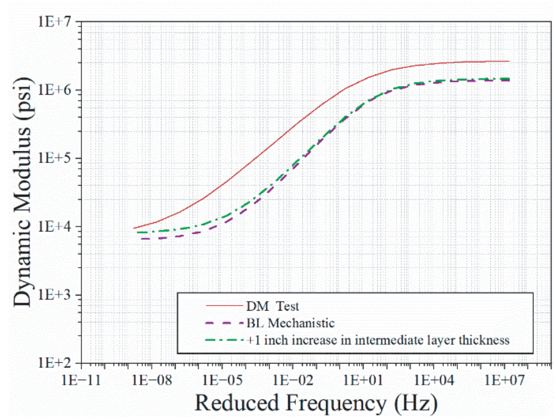

(b)

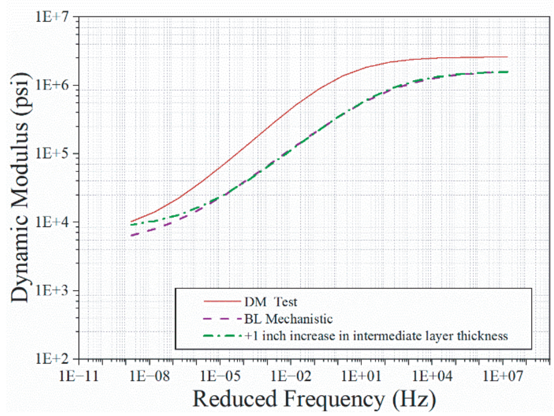

(c)

Figure 6.17 Backcalculated E^* Master Curves Under a 1-in. Increase in the Intermediate Layer Thickness: (a) Surface Layer, (b) Intermediate Layer, and (c) Base layer.

6.3.3 Surface Layer's Poisson Ratio Sensitivity

This section evaluates the effect of the asphalt mixture's Poisson's ratio (ν) on the accuracy of the backcalculated E^* master curves for all pavement layers. To this end, a 10% change in the surface layer's ν is applied, causing a 0.035 increase in ν from the default value of 0.35. Figure 6.19 shows the results for all layers, with a noticeable change occurring in the backcalculated E^* master curves of the surface and base layers. As shown in Figure 6.19a, the small change in ν causes a considerable shift in the surface layer curve at all frequencies. The most noticeable change occurs at frequencies below 10 Hz, where the loading time or temperature causes the asphalt materials to show a predominant viscoelastic behavior. This change implies that the variation of the surface layer's ν significantly impacts the lateral deformation in the surface layer and subsequently affects the overall strain-strain responses in the horizontal direction. This is especially important when a proper evaluation of the asphalt layer's fatigue properties depends on precisely determining the critical tensile strain at the bottom of the surface layer.

Figure 6.19b indicates no meaningful change in the backcalculated E^* master curve for the intermediate layer under a slight change of surface material's ν. However, a meaningful change is observable in the master curve related to the base layer (see Figure 6.19c).

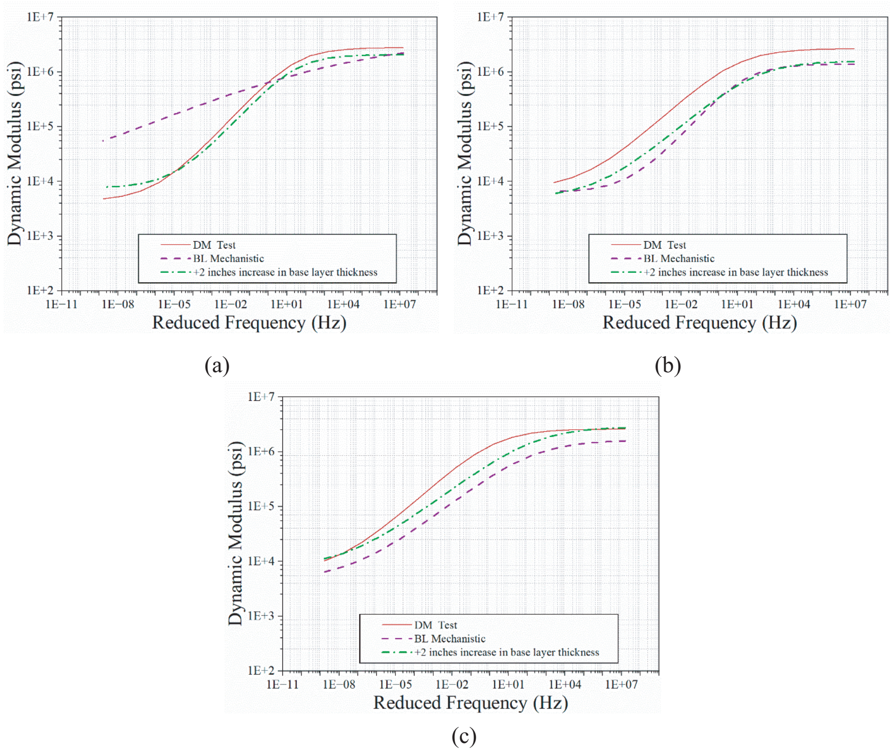

Figure 6.18 Backcalculated *E** Master Curves Under a 2-in. Increase in the Base Layer Thickness: (a) Surface Layer, (b) Intermediate Layer, and (c) Base Layer.

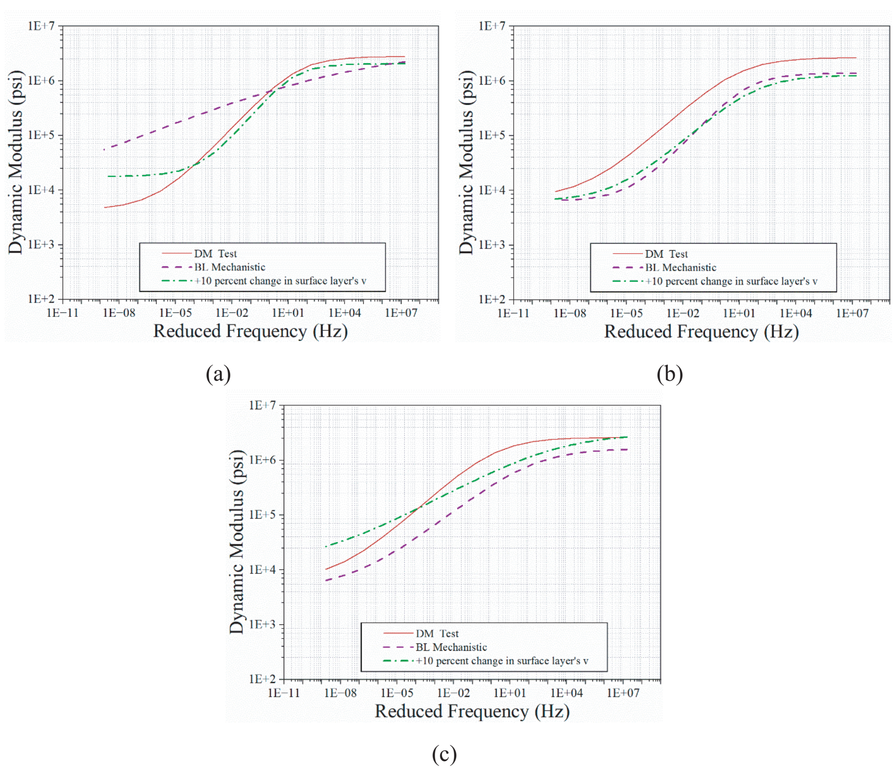

Figure 6.19 Backcalculated ***E**** Master Curves Under a 10% Change in the Surface Layer's ν: (a) Surface Layer, (b) Intermediate Layer, and (c) Base Layer.

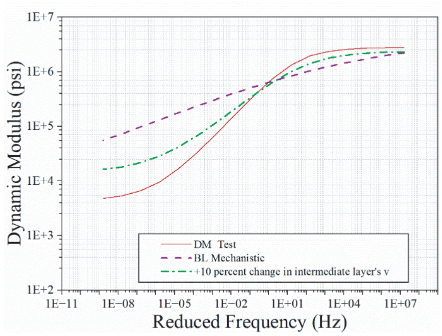

(a)

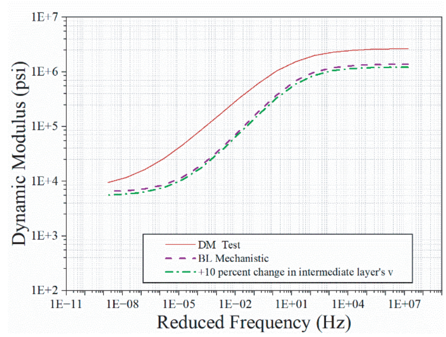

(b)

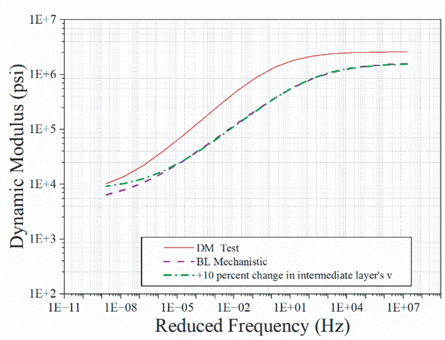

(c)

Figure 6.20 Backcalculated ***E**** Master Curves Under a 10% Change in the Intermediate Layer's ν: (a) Surface Layer, (b) Intermediate Layer, and (c) Base Layer.

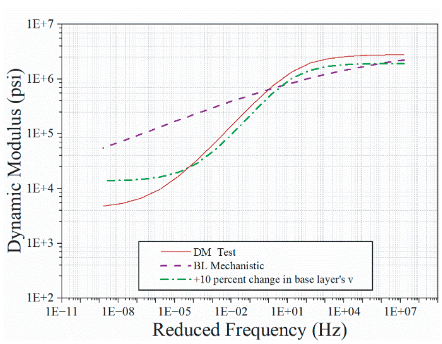

(a)

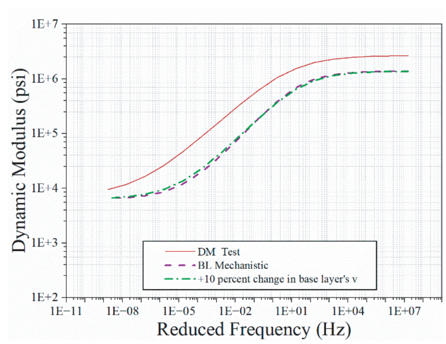

(b)

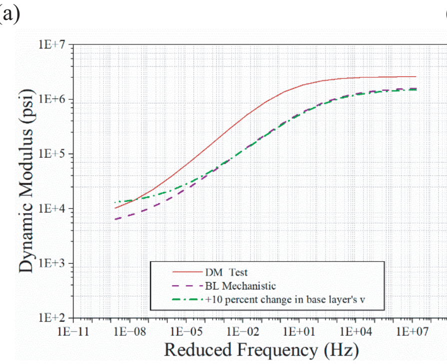

(c)

Figure 6.21 Backcalculated ***E**** Master Curves Under a 10% Change in the Base Layer's ν: (a) Surface Layer, (b) Intermediate Layer, and (c) Base Layer.

7. SUMMARY AND RECOMMENDATIONS

The Dynamic Modulus (E^*) master curve is a fundamental asphalt material property that describes an asphalt mixture's behavior over a broad range of loading frequencies and temperatures. This property is commonly determined either through direct measurement from dynamic modulus testing on asphalt specimens or through backcalculating processes using pavement deflection data obtained from NDT such as the FWD. Given the time and budget limitations of most highway agencies, estimating the E^* master curve from FWD testing will help improve pavement evaluation accuracy and subsequently, allow for better-informed decisions about M&R strategies.

Many elastic modulus backcalculation techniques have been developed to assess the load-bearing capacity of existing flexible pavements. However, due to the viscoelastic nature of asphalt materials, these elastic techniques often fail to accurately characterize the actual in-situ performance of flexible pavements. Therefore, developing a backcalculation method to estimate the E^* master curve of flexible pavement using FWD test results has become an important focus of recent advancements in pavement evaluation techniques.

This study developed a mechanistic-based technique to determine the E^* master curve using the FWD time-history deflection data and has achieved several key outcomes that advance the understanding of in-situ flexible pavement performance through detailed theoretical derivation, laboratory measurement validation, and sensitivity analysis. The research successfully developed a mechanistic-based backcalculation technique that integrates LET with viscoelastic principles. The model defines a link between the pavement deflection data and the relaxation modulus by decomposing the load pulse into several time intervals and applying DTFT analysis. Finally, Laplace transform functions, corresponding principles, and a fractional-order differential model were used to construct the E^* master curve. In contrast, the currently used ViscoWave method, which relies on continuous integral transforms and sigmoidal functions, can generate the overall E^* master curve trend, but it consistently shows discrepancies when compared to laboratory-measured E^* master curve.

Overall, the conclusion drawn from this study are:

- The developed mechanistic-based technique can successfully generate asphalt mixture E^* master curves with a higher degree of accuracy than can existing methods. This conclusion was validated with laboratory-measured E^* values from dynamic modulus testing of field-cored specimens from several flexible pavements.
- Among the varied pavement layers, the backcalculated E^* master curve for the surface layer demonstrates the highest accuracy in most cases. Although the backcalculated E^* master curves for the base and intermediate layers closely match the results of dynamic modulus testing, the surface layer is the most sensitive and reliable measure of pavement condition because of its interaction with the applied load and its surroundings.
- In contrast to the mechanistic-based technique, the ViscoWave method produced the E^* master curve with lower accuracy.
- The pavement structural properties, such as layer thickness and Poisson ratio, significantly influence the accuracy of the backcalculated E^* master curve obtained from the mechanistic-based approach. Also, the surface layer shows the highest sensitivity to even small parameter variations.

The mechanistic-based approach eliminates the requirement for time-consuming laboratory tests while increasing reliance on in-situ pavement condition assessments. By accurately calculating the E^* master curve using the time-history data from the FWD measurement, agencies can effectively optimize their M&R strategies. Although this work estimates the E^* master curve with a higher degree of accuracy than the existing methods, there is still some space for improvement by incorporating thermodynamic principles to consider a realistic temperature gradient throughout the pavement depth. Moreover, this study highlights the need to accurately determine Poisson's ratio and develop a better nondestructive approach for measuring pavement layer thicknesses.

REFERENCES

Al-Khoury, R., Scarpas, A., Kasbergen, C., & Blaauwendraad, J. (2001). Spectral element technique for efficient parameter identification of layered media. I. Forward calculation. *International Journal of Solids and Structures*, *38*(9), 1605–1623. https://doi.org/10.1016/S0020-7683(00)00112-8

ARA, Inc. (2004). *Guide for mechanistic-empirical design of new and rehabilitated pavement structures*. https://content.aashtowarepavementme.org/Documents/1-37A/2appendices_AA.pdf

Bari, J. (2005). *Development of a new revised version of the Witczak E* predictive models for hot mix asphalt mixtures* (Publication No. 2005.3194882) [Doctoral dissertation, Arizona State University]. ProQuest Dissertations Publishing. https://www.proquest.com/openview/c7db4f51a98541feefe2dedf499414c2/1?cbl=18750&diss=y&pq-origsite=gscholar

Cai, X., Wang, D., & Yu, J. (2020). Evaluation of the functional performance of paving materials based on the driving wheel pavement analyzer. *Applied Sciences*, *10*(7), 2410. https://doi.org/10.3390/app10072410

Chen, D.-H., Fernando, E., & Murphy, M. (1996). Application of falling weight deflectometer data for analysis of superheavy loads. *Transportation Research Record*, *1540*(1), 83–90. https://doi.org/10.1177/0361198196154000112

Chen, J., Hossain, M., & Latorella, T. M. (1999). Use of falling weight deflectometer and dynamic cone penetrometer in pavement evaluation. *Transportation Research Record*, *1655*(1), 145–151. https://doi.org/10.3141/1655-19

Cheng, H., Wang, Y., Liu, L., & Sun, L. (2021). Relationships between asphalt-layer moduli under vehicular loading and FWD loading. *Journal of Materials in Civil Engineering*, *33*(1), 4020437. https://doi.org/10.1061/(ASCE)MT.1943-5533.0003429

Endiran, S. V. (1999). *Nonlinear dynamic computer modeling of flexible pavements* (Publication No. 1999.9967751) [Doctoral dissertation, University of Arkansas]. ProQuest Dissertations Publishing. https://www.proquest.com/docview/304524534?pq-origsite=gscholar&fromopenview=true&sourcetype=Dissertations%20&%20Theses

Flügge, W. (1967). *Viscoelasticity*. Blaisdell Publishing Company.

Fu, G., Wang, J., Zhao, Y., Cao, D., Wu, F., & Sha, D. (2024). Development of a prediction model of dynamic deflections for asphalt pavements under FWD impulse loading. *Construction and Building Materials*, *425*, 135944. https://doi.org/10.1016/j.conbuildmat.2024.135944

Gopalakrishnan, K., Kim, S., Ceylan, H., & Kaya, O. (2014). *Development of asphalt dynamic modulus master curve using falling weight deflectometer measurements* (Institute for Transportation Report No. HRB Project TR-659). Iowa State University. https://rosap.ntl.bts.gov/view/dot/28113

Graziani, A., Mignini, C., Bocci, E., & Bocci, M. (2020). Complex modulus testing and rheological modeling of cold-recycled mixtures. *Journal of Testing and Evaluation*, *48*(1), 120–133. https://doi.org/10.1520/JTE20180905

Washington State Department of Transportation. (2005). *Pavement analysis computer software and case studies*. Washington State Department of Transportation.

Gupta, A., & Kumar, A. (2014). Comparative structural analysis of flexible pavements using finite element method. *International Journal on Pavement Engineering & Asphalt Technology*, *15*(1), 11–19. https://doi.org/10.2478/ijpeat-2013-0005

Haas, R., & Hudson, W. R. (1978). *Pavement management systems*. McGraw-Hill.

Hajikarimi, P., & Hosseini, A. S. (2023). *Constructional viscoelastic composite materials: Theory and application*. Springer Singapore. https://doi.org/10.1007/978-981-99-1786-0

Hajikarimi, P., & Nejad, F. M. (2021). *Applications of viscoelasticity: Bituminous materials characterization and modeling*. Elsevier.

Hajj, E. Y., Skaff, R., Sebaaly, P. E., Ma, X., Qin, H., & Yan, F. (2024). *Enhancing pavement assessment with dynamic backcalculation: A dynamic finite element approach* (Federal Aviation Administration Report No. DOT/FAA/TC-24/13). United States Department of Transportation. https://www.airporttech.tc.faa.gov/Products/Airport-Pavement-Papers-Publications/Airport-Pavement-Detail/enhancing-pavement-assessment-with-dynamic-backcalculation-a-dynamic-finite-element-approach

Hofko, B., Blab, R., & Mader, M. (2012). Impact of air void content on the viscoelastic behavior of hot mix asphalt. In J. T. Harvey & J. Pais (Eds.), *Four point bending* (pp. 139–149). CRC Press.

Huang, Y. H. (1993). *Pavement analysis and design*. Prentice Hall.

Kausel, E., & Peek, R. (1982). Dynamic loads in the interior of a layered stratum: An explicit solution. *Bulletin of the Seismological Society of America*, *72*(5), 1459–1481. https://doi.org/10.1785/BSSA0720051459

Kutay, M. E., Chatti, K., & Lei, L. (2011). Backcalculation of dynamic modulus mastercurve from falling weight deflectometer surface deflections. *Transportation Research Record*, *2227*(1), 87–96. https://doi.org/10.3141/2227-10

Lakes, R. S. (2009). *Viscoelastic materials*. Cambridge University Press. https://doi.org/10.1017/CBO9780511626722

Lee, H. S. (2013). *Development of a new solution for viscoelastic wave propagation of pavement structures and its use in dynamic backcalculation* [Doctoral dissertation, Michigan State University]. MSU Libraries Digital Repository. https://doi.org/doi:10.25335/enj2-nb52

Lee, H. S. (2014). ViscoWave–A new solution for viscoelastic wave propagation of layered structures subjected to an impact load. *International Journal of Pavement Engineering*, *15*(6), 542–557. https://doi.org/10.1080/10298436.2013.782401

Lei, L. (2011). *Backcalculation of asphalt concrete complex modulus curve by layered viscoelastic solution* [Doctoral dissertation, Michigan State University]. MSU Libraries Digital Repository. https://doi.org/doi:10.25335/rbfr-0g22

Lekhnitskiĭ, S. G. (1963). *Theory of elasticity of an anisotropic elastic body*. Holden-Day.

Liu, W., & Scullion, T. (2001). *MODULUS 6.0 for Windows: User's manual* (Texas Transportation Institute Report No. FHWA/TX-02/1869-3). Texas A & M University System College. https://pavementdesign.tamu.edu/manuals/Modulus6.pdf

Lytton, R. L. (1989). Backcalculation of pavement layer properties [Conference session]. In *Nondestructive testing of pavements and backcalculation of moduli* (pp. 7–38). First International Symposium on Nondestructive Testing of Pavements and Backcalculation of Moduli, Baltimore, Maryland. ASTM International. https://trid.trb.org/View/657727

Malvern, L. E. (1969). *Introduction to the mechanics of a continuous medium*. Prentice-Hall International Incorporated. https://trid.trb.org/View/199874

Mangiafico, S., Sauzéat, C., & Di Benedetto, H. (2019). 2S2P1D model calibration error from user panel for one bitumen and one bituminous mixture. *Advances in Materials Science and Engineering*, *2019*(1). https://doi.org/10.1155/2019/6547025

Manjusha, M., & Sunitha, V. (2023). A review of advanced pavement distress evaluation techniques using unmanned aerial vehicles. *International Journal of Pavement Engineering*, *24*(2). https://doi.org/10.1080/10298436.2023.2268796

Menzinger, M., & Wolfgang, R. (1969). The meaning and use of the Arrhenius activation energy. *Angewandte Chemie International Edition in English*, *8*(6), 438–444. https://doi.org/10.1002/anie.196904381

Nair, S. K., Hudson, W. R., & Lee, C. E. (1985). *Realistic pavement serviceability equations using the 690D surface dynamics profilometer* (Center for Transportation Research Report No. FHWA/TX-86/09+354-1F). University of Texas at Austin. https://library.ctr.utexas.edu/digitized/texasarchive/phase2/354-1f-ctr.pdf

Öcal, A. (2014). *Backcalculation of pavement layer properties using artificial neural network based gravitational search algorithm* [Master's thesis, Middle East Technical University]. OpenMETU. https://hdl.handle.net/11511/24098

Omer, J. R., & Eghan, B. A. (2018). Numerical analysis of road pavement response. *Advancements in Civil Engineering & Technology*, *2*(2). https://doi.org/10.31031/ACET.2018.02.000531

Park, B., Cho, S., Rahbar-Rastegar, R., Nantung, T. E., & Haddock, J. E. (2022). Prediction of critical responses in full-depth asphalt pavements using the falling weight deflectometer deflection basin parameters. *Construction and Building Materials*, *318*, 126019. https://doi.org/10.1016/j.conbuildmat.2021.126019

Park, B., Cho, S., Rahbar-Rastegar, R., Nantung, T. E., & Haddock, J. E. (2024). Use of falling weight deflectometer data to determine the effective structural number of full-depth asphalt pavements for structural condition assessment. *Road Materials and Pavement Design*, *25*(2), 276–290. https://doi.org/10.1080/14680629.2023.2200843

Rao, C., & Von Quintus, H. (2016). *Determination of in-place elastic layer modulus: Backcalculation methodology and procedures* [Webinar]. Transportation Research Board. https://www.trb.org/Main/Blurbs/174867.aspx

Roberts, F. L., & Hudson, W. R. (1971). Pavement serviceability equations using the surface dynamics profilometer. *Special Rep*, *116*, 68–79.

Sabahfar, N., Murrell, S., & Larrazabal, E. (2021). Comparison of light weight profilometer and mobile LiDAR for runway profile measurements. In H. Ozer, J. F. Rushing, & Z. Leng (Eds.), *Airfield and highway pavements 2021*: *Airfield pavement technology* (pp. 43–53). https://doi.org/10.1061/9780784483527.004

Sangghaleh, A., Pan, E., Green, R., Wang, R., Liu, X., & Cai, Y. (2014). Backcalculation of pavement layer elastic modulus and thickness with measurement errors. *International Journal of Pavement Engineering*, *15*(6), 521–531. https://doi.org/10.1080/10298436.2013.786078

Satyanandam, G., Guzzarlapudi, S. D., & Yadu, L. (2023). Assessment of robustness of backcalculation tool in capturing pavement moduli using FWD device [Conference paper]. In P. K. Sahu, N. Saboo, B. B. Majumdar, & A. Pani (Eds.), *Proceedings of the 7th International Conference of Transportation Research Group of India (CTRG 2023), Volume 1* (pp. 321–336). https://doi.org/10.1007/978-981-97-9654-0_19

Schnebele, E., Tanyu, B. F., Cervone, G., & Waters, N. (2015). Review of remote sensing methodologies for pavement management and assessment. *European Transport Research Review*, *7*, 7. https://doi.org/10.1007/s12544-015-0156-6

Schwarzl, F., & Staverman, A. J. (1952). Time-temperature dependence of linear viscoelastic behavior. *Journal of Applied Physics*, *23*(8), 838–843. https://doi.org/10.1063/1.1702316

Sebaaly, B., Davis, T. G., & Mamlouk, M. S. (1985). Dynamics of falling weight deflectometer. *Journal of Transportation Engineering*, *111*(6), 618–632.https://doi.org/10.1061/(ASCE)0733-947X(1985)111:6(618)

Shahin, M. Y. (1994). *Pavement management for airports, roads, and parking lots.* Chapman & Hall. https://trid.trb.org/View/461067

Sharma, S., & Das, A. (2008). Backcalculation of pavement layer moduli from falling weight deflectometer data using an artificial neural network. *Canadian Journal of Civil Engineering*, *35*(1), 57–66. https://doi.org/10.1139/L07-083

Shukla, A., & Joshi, Y. M. (2017). Boltzmann superposition principle for a time-dependent soft material: Assessment under creep flow field. *Rheologica Acta*, *56*, 927–940. https://doi.org/10.1007/s00397-017-1044-x

Singh, S. J. (1986). Static deformation of a transversely isotropic multilayered half-space by surface loads. *Physics of the Earth and Planetary Interiors*, *42*(4), 263–273. https://doi.org/10.1016/0031-9201(86)90029-4

Sivaneswaran, N., Kramer, S. L., & Mahoney, J. P. (1991). Advanced backcalculation using a nonlinear least squares optimization technique. *Transportation Research Record*, *1293*, 93–102. http://onlinepubs.trb.org/Onlinepubs/trr/1991/1293/1293-010.pdf

Solatifar, N., Kavussi, A., Abbasghorbani, M., & Sivilevičius, H. (2017). Application of FWD data in developing dynamic modulus master curves of in-service asphalt layers. *Journal of Civil Engineering and Management*, *23*(5), 661–671. https://doi.org/10.3846/13923730.2017.1292948

Strickland, D. (2001). Shell pavement design software for Windows. *The asphalt yearbook 2001*. Institute of Asphalt Technology. https://trid.trb.org/View/683379

Tarefder, R. A., & Ahmed, M. U. (2013). Consistency and accuracy of selected FWD backcalculation software for computing layer modulus of airport pavements. *International Journal of Geotechnical Engineering*, *7*(1), 21–35. https://doi.org/10.1179/1938636212Z.0000000009

Varma, S., Kutay, M. E., & Chatti, K. (2013). Data requirements from falling weight deflectometer tests for accurate backcalculation of dynamic modulus master curve of asphalt pavements [Conference proceedings]. In I. L. Al-Qadi, & S. Murrell (Eds.), *Airfield and highway pavement 2013: Sustainable and efficient pavements* (pp. 445–455). https://doi.org/10.1061/9780784413005.035

Von Quintus, H. L., Rao, C., & Irwin, L. H. (2015). *Long-term pavement performance program determination of in-place elastic layer modulus: Backcalculation methodology and procedures* (Federal Highway Administration Report No. FHWA-HRT-15-036). Federal Highway Administration. https://www.fhwa.dot.gov/publications/research/infrastructure/pavements/ltpp/15036/index.cfm

Vyas, V., Singh, A. P., & Srivastava, A. (2021). Prediction of asphalt pavement condition using FWD deflection basin parameters and artificial neural networks. *Road Materials and Pavement Design*, *22*(12), 2748–2766. https://doi.org/10.1080/14680629.2020.1797855

White, G. (2019). Use of falling weight deflectometer for airport pavements [Conference paper]. In M. Barman, M. Zaman, & J. R. Chang (Eds.), *Transportation and geotechniques: Materials, Sustainability and Climate* (pp.119–133). Springer. https://doi.org/10.1007/978-3-319-95768-5_11

Witczak, M., El-Basyouny, M., & El-Badawy, S. (2007). *Incorporation of the new (2005) E* predictive model in the MEPDG* [NCHRP 1-40D final report]. Arizona State University.

Witczak, M. W., & Bari, J. (2004). *Development of a master curve (E*) database for lime modified asphaltic mixtures*. Arizona State University.

Zhao, W., Wu, W., Yang, Q., & Liu, J. (2022). Accuracy analysis of modulus results considering the whole process of modulus back-calculation—based on GPR and FWD. *Construction and Building Materials*, *348*, 128671. https://doi.org/10.1016/j.conbuildmat.2022.128671

About the Joint Transportation Research Program (JTRP)

On March 11, 1937, the Indiana Legislature passed an act which authorized the Indiana State Highway Commission to cooperate with and assist Purdue University in developing the best methods of improving and maintaining the highways of the state and the respective counties thereof. That collaborative effort was called the Joint Highway Research Project (JHRP). In 1997 the collaborative venture was renamed as the Joint Transportation Research Program (JTRP) to reflect the state and national efforts to integrate the management and operation of various transportation modes.

The first studies of JHRP were concerned with Test Road No. 1—evaluation of the weathering characteristics of stabilized materials. After World War II, the JHRP program grew substantially and was regularly producing technical reports. Over 1,600 technical reports are now available, published as part of the JHRP and subsequently JTRP collaborative venture between Purdue University and what is now the Indiana Department of Transportation.

Free online access to all reports is provided through a unique collaboration between JTRP and Purdue Libraries. These are available at https://docs.lib.purdue.edu/jtrp/.

Further information about JTRP and its current research program is available at https://engineering.purdue.edu/JTRP.

About This Report

An open access version of this publication is available online. See the URL in the citation below.

Notani, M. A., Cho, S., & Haddock, J. E. (2025). *Backcalculated dynamic modulus master curve from the time histories of falling weight deflectometer surface deflections* (Joint Transportation Research Program Publication No. FHWA/IN/JTRP-2025/18). West Lafayette, IN: Purdue University. https://doi.org/10.5703/1288284317898